DTU Library

Quantum Communication with non-Gaussian states

Breum, Casper Rubæk

Publication date:
2020

Document Version
Publisher's PDF, also known as Version of record

[Link back to DTU Orbit](#)

Citation (APA):
Breum, C. R. (2020). *Quantum Communication with non-Gaussian states*. Department of Physics, Technical University of Denmark.

DTU Physics
Department of Physics

Quantum Communication with non-Gaussian states

A dissertation submitted to the Department of Physics at the Technical University of Denmark in partial fulfilment of the requirements for the degree of philosopiae doctor

Casper Rubæk Breum
November 2020

Supervisor: Professor Ulrik Lund Andersen
Co-supervisor: Senior Researcher Jonas Schou Neergaard-Nielsen

Abstract

In this thesis we investigate two aspects of quantum information processing with continuous variables in networks. Quantum physics is currently undergoing its second revolution, in which the unique properties of quantum superpositions and non-classical entanglement are harnessed and engineered to improve technologies across a wide range of fields. One particular area of interest is the connection of different quantum devices across a shared network, where the scale can range from a single room to the size of a university or company campus. An obvious choice of channels for networks of this size is optical fibers and so the faithful transfer of quantum states of light across the channels of the network becomes an integral challenge.

Firstly, we generate a continuous variable non-Gaussian state, namely the single photon subtracted squeezed vacuum state (1-PSSqV), and use it as a probe of the transmission efficiency across three different network channels. For the first channel, a 1m single mode fiber (SMF) on the same optical table of the state generation setup, we measure a Wigner negativities of $-0.206 \pm 0.001\pi$ of the received state. For the second channel, a 60 m SMF connection between the state generation lab and an adjacent lab, we measure $-0.104 \pm 0.001\pi$. For the third channel, a 400 m connection across 3 nodes of the DTU campus fiber-optic network to a separate building, we unfortunately could not measure any Wigner negativity. Here the main problem was optical loss of the channel. The presence of Wigner negativity confirms the survival of the highly non-classical correlations of the transmitted state.

Secondly, we implement a sensing protocol on a small on-table free-space network consisting of four nodes. In the protocol a continuous variable multi-partite entangled state is used to measure the average of individual phase shifts at each node. Here we show an increased sensitivity to the phase shift, as a $\sim 20\%$ reduction in the root-mean-square estimation error, compared to the sensitivity possible for any measurement protocol not using an entangled probe state.

Resumé

I denne afhandling undersøger vi to aspekter af kvanteinformations behandling med kontinuerlige variable i netværk. Kvantefysik gennemgår i øjeblikket sin anden revolution, hvor de unikke egenskaber ved kvantemekanisk superposition og ikke-klassisk sammenfiltring udnyttes og controlleres til at forbedre teknologier på tværs af en lang række felter. Et særligt interessant område er forbindelsen mellem forskellige kvanteenheder på tværs af et fælles netværk, hvor størrelsen kan være fra et enkelt rum til et universitet eller en virksomhedscampus. Et åbenlyst valg af kanaler til et netværk af denne størrelse er optiske fibre, hvorved pålidelig overførsel af kvantetilstande i laserlys over netværkets kanaler bliver en central udfordring.

Først, genererer vi en kontinuerlig variabel ikke-Gaussisk tilstand, navnlig den enkelt fotonfratrukket klemte vakuumtilstand og bruger den som en sonde for transmissionseffektiviteten på tværs af tre forskellige netværkskanaler. For den første kanal, en 1m single-mode optisk fiber (SMF) placeret på det samme optiske bord som tilstandsgenerationsopsætningen, måler vi en Wigner-negativitet på $-0.206 \pm 0.001\pi$ af den modtagne tilstand. For den anden kanal, en 60 m SMF-forbindelse mellem tilstandsgenerationslaboratoriet og et tilstødende laboratorie, måler vi $-0.104 \pm 0.001\pi$. For den tredje kanal, en 400 m forbindelse på tværs af 3 krydsnoder i DTU campus fiberoptiske netværk til en separat bygning, kunne vi desværre ikke måle nogen Wigner-negativitet. Problemet var her hovedesageligt optisk tab undervejs. Tilstedeværelsen af Wigner-negativitet bekræfter overlevelsen af de stærke ikke-klassiske korrelationer i den transmitterede tilstand.

Efter, implementerer vi en måleprotokol på et lille bordbegrænset fritlufts netværk bestående af fire knudepunkter. I protokollen anvendes en kontinuerligt variabel flerdelt sammenfiltret sondetilstand til at måle gennemsnittet af individuelle faseforskydninger ved hvert knudepunkt. Her viser vi en øget følsomhed over for faseforskydningen, som en $\sim 20\%$ reduktion i rod-middel-kvadrat måleafvigelsen, sammenlignet med den følsomhed der er mulig for enhver måleprotokol der ikke bruger en sammenfiltret sondetilstand.

Acknowledgements

I will start from the beginning and so should start by thanking ass. prof. Alexander Huck for giving my lab partner, Kristoffer Joanesarson, and I the opportunity to do our bachelors project at the QPIT section of DTU Physics. This marked my first encounter with experimental quantum physics. Later during my masters, with the help of prof. Ulrik L. Andersen, I arranged to take a semester abroad in Japan at the University of Tokyo. Here i joined the group of prof. Akira Furusawa and worked together with his student Okada Masanori. This was my baptism by fire in the arts of experimental quantum optics and i owe a great deal to Okada for holding my hand, his patience and for teaching me all the tricks of the trade. I would also like to thank Akira for hosting me, the secretary Yumiko Yoshikawa for all the paperwork and the rest of group for welcoming me and making my stay i Japan an unforgeable experience.

After returning to Denmark I joined the QPIT group to do my masters project and eventually my PhD project, both with Jonas S. Neergaard-Niesen and Ulrik has supervisors. I would like to thank them both greatly for giving me those opportunities. During my PhD I once again went to Japan to stay at the Furusawa group for a 6 week external stay. I would like to thank Akira for giving my the opportunity to come back, Mamoru Endo for letting me join his project and and the rest of the group for welcoming me back and taking care of me during my stay. At QPIT I would like to thank all my fellow PhD student through my time for great camaraderie and for always being there to provide reassurance when things in were not working. I have also great appreciated the help with paperwork and annoying DTU systems of our secretary Tine Klitmøller.

I would especially like to thank my office and lab partners Xueshi Guo, Shuro Izumi and Mikkel V. Larsen for making my time at QPIT truly special. I consider you my friends and I don't think I could have managed these years without you. Besides the tremendous help you have given me in the lab and in the office, I thank you for all the ramen / burger nights, dice games, Friday bar beers and fun times we have had. Our team leader, Jonas, also deserved high praise for providing a fun and engaging atmosphere and for always being ready to help and provide assistance, be it physics or life en general. I would also like to thank Jens Arnbak for being an all round outstanding guy and excellent PhD colleague. I hope all of us will continue to stay in touch. At DTU I would also like to thank my classmates Kristoffer, Emil Denning, Mads G. Senstius and Søren K. Hansen for our time in Klub 47. For our lengthy, heated and, perhaps drunken, discussions of everything physics and more.

But most of all I need to thank my beautiful fiancée, Annemette Isager Ahl, for keeping up with me during my studies the past 6 years and for providing eternal support and comfort during the hard times. And to our son, August Ahl Breum, for providing me some much needed reflection in what is important in life. It broke my heart having to spend so many late nights in lab and so much time away from you both during the final months of my PhD and I am forever grateful for the incredible strength you showed during that time. Celebrating Augusts 6 months on the day I handed in my thesis was both properly the biggest relief i have ever felt and one of the happiest days of my life.

Kgs. Lyngby, November 2020
Casper R. Breum

Declaration

I, Casper R. Breum, declare that this thesis and the work presented here is my own and has not previously been submitted for award at this or any other institution. The work of others shown here is appropriately referenced. Parts of this thesis are based upon published articles or manuscripts in preparation for publication in peer-reviewed physics journals. Below is a list of the work I contributed to during my Ph.D. project.

Journal publication contributions

Mikkel V. Larsen, Xueshi Guo, Casper R. Breum, Jonas S. Neergaard-Nielsen, Ulrik L. Andersen, *Fiber-coupled EPR-state generation using a single temporally multiplexed squeezed light source*, npj Quantum Information **5** (1), 46 (2019)

Mikkel V. Larsen, Xueshi Guo, Casper R. Breum, Jonas S. Neergaard-Nielsen, Ulrik L. Andersen, *Deterministic generation of a two-dimensional cluster state for universal quantum computing*, Science **366**, 6463 369-372 (2019)

Xueshi Guo, Casper R. Breum, Johannes Borregaard, Shuro Izumi, Mikkel V. Larsen, Matthias Christandl, Jonas S. Neergaard-Nielsen, Ulrik L. Andersen, *Distributed quantum sensing in a continuous variable entangled network*, Nature Physics 16, 281-284 (2020)

Mikkel V. Larsen, Xueshi Guo, Casper R. Breum, Jonas S. Neergaard-Nielsen and Ulrik L. Andersen, *Deterministic multi-mode gates on a scalable photonic quantum computing platform*, arXiv:2010.14422 [quant-ph] (2020)

School, conference and workshop contributions

- Summer School on Quantum and Nonlinear Optics, Talk: *Towards experimental realization of High-Fidelity Teleportation of Continuous-Variable Quantum States in the telecom band*, PhD school, Gilleje, Denmark June 2017

- 24th Central European Workshop on Quantum Optics, Poster: *Towards experimental realization of High-Fidelity Teleportation of Continuous-Variable Quantum States in the telecom band*, conference, Technical university of Denmark, Denmark June 2017

- VI Quantum Information Workshop and School, Poster: *Towards experimental realization of High-Fidelity Teleportation of Continuous-Variable Quantum States in the telecom band*, PhD school and workshop, Paraty, Brazil August 2017

- Annual Meeting of Danish Physical Society, Poster: *Distributed sensing using Squeezed States of Light*, workshop, Middelfart, Denmark June 2018

- Quantum Technology International Conference, Poster: *Distributed phase sensing using four-mode entanglement*, conference, Paris, France September 2018

- QMATH Masterclass on Quantum Communication and Computation with Continuous Variables, Poster: *Towards a optical quantum state synthesizer using novel photon-number resolving detector*, workshop, University of Copenhagen, Denmark June 2019

- QuantumDTU Summer School on Quantum Technology 2019, Poster: *Towards a optical quantum state synthesizer using novel photon-number resolving detector*, PhD school, Gilleje, Denmark August 2019

Contents

Introduction

When the first few bits of data were transmitted between the computers at the University of California and Stanford Research Institute in 1969, on a precursor network to today's internet, it is not hard to imagine that the researchers involved never could have dreamed of the endless possibilities this technology one day would allow. Similarly it is doubtful that Bardeen, Brattain and Shockley could have fully grasped the potential of their invention and the scope of the ensuring digital revolution. What might seem like fundamental research today, far removed from any practical importance, can in time prove to lay the foundation of technical advances of great importance. It is in this fog of possible direction to pursue, not knowing which direction is correct (if any direction will turn out to be?), that much of current quantum information research plays out.

The first quantum revolution was a revolution of atomic and subatomic physics, which among many things leads to the aforementioned invention of the transistor, which in turn lead to the construction of the computers at UCLA and SRI and to the internet. We are now in the middle of the second quantum revolution. Its beginning was marked by the application of quantum mechanics to information theory and is now concerned with the application of this new theory to the development of new and improved technology. These efforts can be divided into three distinct, but interlinked fields, as exemplified by the pillars of the ongoing European Quantum Flagship program [1]; Quantum Computing / Simulation, Quantum Communication and Quantum Sensing / Metrology. It

is believed that all of these fields will see technology improved by quantum mechanics in the coming decades [2].

A central concept in the development of such improved technologies is the threshold, called *quantum advantage*, at which a quantum improved technology does something (anything) that a similar technology based on classical physics can not do. This threshold was claimed passed last year by Google in the context of quantum computation [3], where they showed that using a 53 qubit processor they could sample distributions of the 2^{53} dimensional computation state space exponentially faster than the best known classical algorithms, though their claim was later refuted by IBM [4]. Recently quantum advantage as also been demonstrated for quantum communication [5] and metrology protocols [6]. While these milestones help to strengthen our belief in the course of the different research direction, they are themselves only stepping stones towards bigger goals. For quantum communication one such goal is the construction of a quantum internet. A network capable of transmitting quantum protected classical information and quantum information encoded in quantum states between distant parties, as well as entangling them, can be used for all three of the main quantum information fields [7]. In the context of quantum communication the obvious candidate for the physical platform on which to build such a network is optics. The main advantage is that quantum information encoded in the electromagnetic field readily can be transmitted through free space and, thanks to the extensive development of telecom technology, through optical fibers.

Tremendous effort has been made in the development of the techniques needed to realise the long distance connections required of a quantum internet [8]. Without resorting to satellite relayed connections, the main obstacle here is the inherent transmission loss of optical fibers and the corresponding primary solution is to rely on quantum repeaters to overcome the loss [9] [10]. On the other hand, for short distance networks, the optical losses might be low enough to allow for direct transmission of simple quantum states. But in a short network it might be more likely that e.g. two quantum computers or several sensing nodes are connected and that more fragile highly non-classical states have to be transmitted. In such a scenario a combination of advanced repeater schemes and error detection and correction codes will eventually be necessary to properly link the nodes [11]. Networks also play an important role for quantum sensing, where an increased interested over the last few years has been given to use of entanglement across network modes as means of improving multi- or distributed parameter estimation protocols [12–14].

The work of this thesis is towards both of these ends and is divided into two projects. In the first project we consider, as a first step, the direct transmission of a continuous variable non-Gaussian state through network channels of various sizes. The state of choice is the photon subtracted squeezed vacuum state, as it

can be reliably produced and serves well as probe of the limits of direct transmission in such conditions. The preservation of measurable Wigner negativity after transmission will serve as the overarching goal and require both low optical loss and stable phase control of the network channel. In the second project we perform a proof-of-principle experimental realization of a distributed sensing protocol, in which an entangled probe state is used to measure the average phase shift of nodes in a small scale network.

The thesis consists of an four main chapters followed by an outlook.

1. **Theory** Here a basic introduction to continuous variable quantum optics is given with a focus on squeezed light and relevant equations used through the thesis presented. A model describing the experimental procedure of creating a 1-PSSqV state is presented together with the theory of tomographic reconstruction from homodyne measurement data, which will be used to analyse experimental results. We also provide a quick walkthrough of the implementation of the maximum likelihood algorithm for the reconstruction process.

2. **Experimental Methods** Here we give a detailed description of the experimental framework for the generation of 1-PSSqV states. We construct a setup to produce continuous wave squeezed light at 1550 nm via parametric down-conversion of a second harmonic field in an OPO cavity. We then tap a small part of the squeezed vacuum field into a trigger channel and frequency filter it to select only the central frequency mode of the OPO output to be measured by a single-photon detector. A click of the single-photon detector then then heralds the creating of the 1-PSSqV state in the signal channel. We also describe the different network configurations the state was transmitted trough.

3. **Non-Gaussian State Transmission** Here the results of the non-Gaussian state transmission project are presented. We analyse the results obtained from three different measurement configurations and compare them to the results expected from our theoretical mode.

4. **Distributed Quantum Sensing** Here the results of the distributed sensing project are presented in the form of the published work together with a short introduction.

5. **Outlook** Concludes on the presented results of the two projects and discusses possible paths forwards.

Continuous Variable Quantum Optics

In this chapter a basic introduction to continuous variable (CV) quantum optics is given. In sec. 2.1 the two main representations of a quantum state of light, the density matrix and the Wigner function, is presented and in sec. 2.2 the properties and generation of one of the the most basic ingredients in any quantum enhanced optical communication, sensing or computational protocol - the squeezed vacuum state - is explored. In sec. 2.3.2 a theoretical model describing an experimentally relevant scheme for producing a non-Gaussian state is derived. The scheme details how the non-Gaussian operation of single photon detection can be used to transform a squeezed vacuum state into a non-Gaussian state - the photon subtracted squeezed vacuum state. Finally in sec. 2.4 the homodyne detection scheme and its use in quantum state tomography presented.

2.1   Representation of quantum states of light

Quantum mechanics is usually explained as the laws of nature at the atomic level. For light this picture translates to quantum optics being the laws of electromagnetism at the single photon level. To unfold them the generic approach is to quantize the electromagnetic field to obtain the Hamiltonian of a harmonic

oscillator, where the electric and magnetic field take on the usual role of position and momentum. A single mode of the electromagnetic field is then described by the Hamiltonian

$$\hat{H} = \hbar\omega \left(\hat{a}^\dagger \hat{a} + \frac{1}{2} \right) \tag{2.1}$$

where $\hat{a}$ and $\hat{a}^\dagger$ are the the non-Hermitian non-commuting annihilation and creation operators with the commutation $[\hat{a}, \hat{a}^\dagger] = 1$, $\hbar$ is Plancks constant and ω the angular frequency of the electromagnetic field. The eigenstate of the quantum harmonic oscillator $\hat{H}$ is then called the energy eigenstates or Fock states $|n\rangle$ and have the eigenvalues $E_n = \hbar\omega(n + 1/2)$, corresponding to the state $|n\rangle$ consisting of n photons i.e. excitation of the electromagnetic field mode. From the definition $\hat{a}|n\rangle = \sqrt{n}|n-1\rangle$ and $\hat{a}^\dagger|n\rangle = \sqrt{n+1}|n+1\rangle$ the photon number operator $\hat{n} = \hat{a}^\dagger \hat{a}$ also shows this $\hat{n}|n\rangle = n|n\rangle$. For $|n=0\rangle$ the state is called the vacuum state or energy ground state corresponding to zero photons. Curiously the nonzero energy of the ground state $E_0 = \hbar\omega/2$ is the first hint the non classical nature of quantum description of light.

2.1.1   Density matrix

The energy eigenstates are conveniently used to span the Hilbert space, as they form a complete set due to the Hermitity of $\hat{H}$. They are then used as the basis to describe any quantum state by its density matrix

$$\hat{\rho} = \sum_i k_i |\psi_i\rangle \langle\psi_i| \tag{2.2}$$

This basis is called the number state basis or Fock basis. The density matrix of a pure quantum state $|\psi\rangle$ is then written as $\hat{\rho} = |\psi\rangle \langle\psi|$, where ψ can be any superposition of photon number states. The diagonal of the density matrix is then the photon number distribution $\text{pr}(n) = \rho_{nn}$ of that state, where $\rho_{mn} = \langle m|\hat{\rho}|n\rangle$. Without further introduction we here present the density matrix representation of the most commonly encountered quantum states as they will be useful to have at hand for later calculations. Their definition and derivation can be found in almost any quantum optics text book [15][16].

State	$|\psi\rangle$	Number state expansion
Vacuum	$|0\rangle$	$\sum\limits_{n=0}^{\infty} \delta_{0n} |n\rangle$
Coherent	$|\alpha\rangle = \hat{D}(\alpha)|0\rangle$	$e^{\frac{-|\alpha|^2}{2}} \sum\limits_{n=0}^{\infty} \frac{\alpha^n}{\sqrt{n!}} |n\rangle$
Sqz. vac.	$|\zeta\rangle = \hat{S}(\zeta)|0\rangle$	$\frac{1}{\sqrt{\cosh r}} \sum\limits_{n=0}^{\infty} \frac{\sqrt{n!}}{(n/2)!} \left(\frac{e^{i\phi} \tanh r}{2} \right)^{\frac{n}{2}} \delta_{0n}^{[2]} |n\rangle$
Fock	$|m\rangle$	$\sum\limits_{n=0}^{\infty} \delta_{mn} |n\rangle$
Odd cat	$|cat_-\rangle$	$\frac{1}{\sqrt{\sinh|\alpha|^2}} \sum\limits_{n=0}^{\infty} \delta_{1n}^{[2]} \frac{\alpha^n}{\sqrt{n!}} |n\rangle$
Even cat	$|cat_+\rangle$	$\frac{1}{\sqrt{\cosh|\alpha|^2}} \sum\limits_{n=0}^{\infty} \delta_{0n}^{[2]} \frac{\alpha^n}{\sqrt{n!}} |n\rangle$

Table 2.1: Typical optical quantum states and their number state expansion coefficients

2.1.2   Phase space and the Wigner function

From the annihilation and creation operators we can define quadrature operators closely resembling the canonical position and momentum operators of a classical harmonic oscillator

$$\hat{x} = \frac{1}{\sqrt{2}} \left(\hat{a}^\dagger + \hat{a} \right) \qquad , \qquad \hat{p} = \frac{i}{\sqrt{2}} \left(\hat{a}^\dagger - \hat{a} \right) \tag{2.3}$$

Using these quadrature operators the Hamiltonian of the quantum harmonic oscillator from eq. 2.1 can be written as $\hat{H} = \frac{\hbar\omega}{2} \left(\hat{x}^2 + \hat{p}^2 \right)$. Note that while the annihilation and creation operators were non-Hermitian[1] the quadrature operators are and have the commutation relation $[\hat{x}, \hat{p}] = i$ corresponding to them being conjugate variables and therefore not precisely measurable at the same time. Instead they must obey the Heisenberg uncertainty principle $\langle \Delta\hat{x}^2 \rangle \langle \Delta\hat{p}^2 \rangle \geq |[\hat{x}, \hat{p}]|/4 = 1/4$. This can also be seen from that fact that while the quadrature expectation values of the number states are zero $\langle \hat{x} \rangle = \langle \hat{p} \rangle = 0$ their variance is

---

[1] Non-Hermition operators are not observables, meaning they do not correspond to a measurable quantity

non-zero even for the vacuum state $\langle \Delta \hat{x}^2 \rangle = \langle \Delta \hat{p}^2 \rangle = n + 1/2$.

The quadrature operators can be combined to represent the quadrature $\hat{q}_\theta$ along any axis in the phase space spanned by the x- and p-axis. We call this quadrature the rotated quadrature

$$\hat{q}_\theta = \cos \theta \; \hat{x} + \sin \theta \; \hat{p} = \tfrac{1}{\sqrt{2}}(\hat{a}^\dagger e^{i\theta} + \hat{a} e^{-i\theta}) \qquad (2.4)$$

Here θ is the angle to x-axis and so we consider $\hat{q}_0 = \hat{x}$ and $\hat{q}_{\pi/2} = \hat{p}$. The eigenstates and eigenvalues of the rotated quadrature operator is then written as $|q_\theta\rangle$ and q respectively. The wave function of a pure quantum state $|\psi\rangle$ can then be calculated as the overlap with the quadrature operator $\psi(q) = \langle q_\theta | \psi \rangle$ and the corresponding quadrature probability function as $\mathrm{Pr}_\theta = |\langle q_\theta | \psi \rangle|^2$. If the state is mixed the quadrature probability has to be calculated using the states density matrix $\mathrm{Pr}_\theta = \langle q_\theta | \hat{\rho} | q_\theta \rangle$. For the number states the explicit expression for the wave function is

$$\langle q_\theta | n \rangle = \frac{e^{-in\theta}}{\sqrt{2^n n! \sqrt{\pi}}} H_n(q) e^{-q^2/2} \qquad (2.5)$$

As we shall see in sec. 2.5.1 this equation will be useful when calculating projection operators in the number state basis. A useful way of visualizing a quantum state in the x-p phase space is using the Wigner function [17]. The Wigner function of a quantum state, defined by its density matrix $\hat{\rho}$, is given defined as

$$W(x,p) = \frac{1}{2\pi} \int_{-\infty}^{\infty} e^{iyp} \left\langle x - \tfrac{y}{2} \right| \hat{\rho} \left| x + \tfrac{y}{2} \right\rangle \, dy \qquad (2.6)$$

In general the Wigner function of any operator $\hat{A}$ is defined in the same way $W_A(x,p) = \frac{1}{2\pi} \int_{-\infty}^{\infty} e^{iyp} \left\langle x - \tfrac{y}{2} \right| \hat{A} \left| x + \tfrac{y}{2} \right\rangle \, dy$. Using the overlap formula $\mathrm{tr}[\hat{A}\hat{B}] = 2\pi \int \int W_A(x,p) W_B(x,p) \, dxdy$ the expectation value of the operator, calculated as $\langle \hat{A} \rangle = \mathrm{tr}[\hat{\rho}\hat{A}]$, can then be calculated from Wigner function in a similar fashion:

$$\left\langle \hat{A} \right\rangle = \mathrm{Tr}\left[\hat{\rho}\hat{A}\right] = 2\pi \int_{-\infty}^{\infty} \int_{-\infty}^{\infty} W(x,p) W_A(x,p) \, dxdy \qquad (2.7)$$

Similar to number state representation we here present, without derivation, the Wigner functions of the same quantum states [15][16]: From the Wigner function it is clear to see that the vacuum state is a Gaussian distribution in the center of phase space with the variance $1/2$, meaning that is a minimum uncertainty state. The coherent state is then simply a vacuum state displaced in phase space, while the squeezed vacuum state is a vacuum state with unequal variances along the p- and x-axis, making it non-classical. Here the variance along the x-axis is reduced below the classical $1/2$ limit but with the variance along the p-axis increased accordingly to satisfy the Heisenberg uncertainty relation. The Fock states are even more non-classical, except for the vacuum state, they all

State	$W(x,p)$	phase space distribution
Vacuum	W_0	$\frac{1}{\pi}\exp\left(-x^2-p^2\right)$
Coherent	W_α	$W_0(x-x_\alpha, p-p_\alpha)$
Sqz. vac.	W_{sqv}	$W_0(xe^{-r}, pe^{r})$
Fock	W_n	$(-1)^n L_n^0(2x^2+2p^2)W_0(x,p)$
Odd cat	W_+	$\frac{1}{2+2e^{-2\alpha^2}}\left[W_0(x-\sqrt{2}\alpha,p)+W_0(x+\sqrt{2}\alpha,p)\right.$ $\left.+2W_0(x,p)\cos\left(2\sqrt{2}p\alpha\right)\right]$
Even cat	W_-	$\frac{1}{2-2e^{-2\alpha^2}}\left[W_0(x-\sqrt{2}\alpha,p)+W_0(x+\sqrt{2}\alpha,p)\right.$ $\left.-2W_0(x,p)\cos\left(2\sqrt{2}p\alpha\right)\right]$

Table 2.2: Wigner functions for typical optical quantum states

have non-Gaussian Wigner functions and have regions in phase space where it is negative. This feature is clear sign of the quantum nature of those states and since their photon number, and thereby energy, is precisely defined they have a completely undefined phase corresponding to rotation symmetry in phase space. But not only the number states can be non-Gaussian, the even and odd Schrödinger's cat states, defined as even $\mathcal{N}_+(|\alpha\rangle+|-\alpha\rangle)$ and odd $\mathcal{N}_-(|\alpha\rangle-|-\alpha\rangle)$ super positions of coherent states opposite in phase space, have regions of negative Wigner function. These states contain either only even or odd photon number contributions.

Conversion to number state basis

From eq. 2.6 we know in principle how to calculate the Wigner function of a quantum state given its density matrix. As we shall see later it will be equally useful to be able to calculate the density matrix given the Wigner function of a state. This can be done by considering that in the number state basis, each matrix element of $\hat{\rho}$ is equal to the expectation value of the corresponding number state projection operator. Using eq.2.7 we can therefore write

$$\rho_{mn} = \text{Tr}\left[\hat{\rho}\,|m\rangle\,\langle n|\right] = 2\pi\int_{-\infty}^{\infty} W(x,p)W_{mn}(x,p)\,dxdy \qquad (2.8)$$

where $W_{mn}(x,p)$ then is the Wigner function of the projection operator $|m\rangle \langle n|$, which has the analytical form

$$W_{mn}(x,p) = \frac{1}{\pi} e^{-x^2-p^2} (-1)^n (x-ip)^{m-n} \sqrt{2^m \frac{n!}{m!}} L_n^{(m-n)}(2x^2+2p^2) \quad (2.9)$$

where $L_n^{(\alpha)}$ is the generalized Laguerre polynomials and the expression being valid for $m \geq n$, with $W_{mn}(x,p) = W_{nm}^*(x,p)$ symmetry for $m < n$. If we on the other hand are in possession of the density matrix, expressed in the number state basis, we can calculate the Wigner function by inserting $\hat{\rho} = \sum_{m,n} \rho_{mn} |m\rangle \langle n|$ directly into eq. 2.6 to get

$$W(x,p) = \sum_{m,n} \rho_{mn} W_{mn}(x,p) \quad (2.10)$$

As we shall see later in sec. 2.5, this will be the case when we perform quantum state reconstruction using the maximum likelihood algorithm, where the outcome is exactly the density matrix in the number state basis and so we will apply eq. 2.10 to obtain the Wigner function of the reconstructed state. Knowing that the off-diagonal elements of a density matrix contains the phase information about the state and that the center of the Wigner function has undefined phase, we expect that $W(0,0)$ should only depend on the diagonal elements of the density matrix. This is exactly the case, since $W_{mn}(0,0) = \frac{1}{\pi}\delta_{mn}(-1)^m$ so that $W(0,0) = \frac{1}{\pi} \sum_n (-1)^n \rho_{nn}$ and, as we shall see in sec. 4.2.2, this expression can be useful when performing optimizing of a parameter in the reconstruction process using the resulting Wigner negativity as a benchmark.

2.1.3 Fidelity and trace distance

The fidelity F between two quantum states $\hat{\rho}_1$ and $\hat{\rho}_2$ is a measure of their closeness in the Hilbert space and takes the value $0 \leq F(\hat{\rho}_1, \hat{\rho}_2) \leq 1$. A fidelity of either 0 or 1 corresponds to $\hat{\rho}_1$ and $\hat{\rho}_2$ being either orthogonal or identical states respectively. If $\hat{\rho}_1 = |\psi_1\rangle \langle \psi_1|$ and $\hat{\rho}_2 = |\psi_2\rangle \langle \psi_2|$ are both pure states, the fidelity is defined as $F(\psi_1, \psi_2) = |\langle \psi_1 | \psi_2 \rangle|^2$. This definition generalizes to the case of either state being impure, so that if $\hat{\rho}_2$ is an impure state the fidelity can be calculated as $F(\psi_1, \hat{\rho}_2) = \langle \psi_1 | \hat{\rho}_2' | \psi_1 \rangle$. For both cases the fidelity can equivalently be written as $F = \text{Tr}[\hat{\rho}_1 \hat{\rho}_2]$. If both states are impure the generalization does not hold and instead a more general expression must be used. In [18] Jozsa defines the necessary conditions for such an expression and then proves that the 'transition probability' formula from [19] satisfy them. The formula is written as

$$F(\hat{\rho}_1, \hat{\rho}_2) = \text{Tr}\left[\sqrt{\sqrt{\hat{\rho}_1} \hat{\rho}_2 \sqrt{\hat{\rho}_1}} \right]^2 \quad (2.11)$$

where $\sqrt{M}$ is the matrix square root defined as $\sqrt{M}\sqrt{M} = M$. From the Wigner functions the fidelity between a pure $|\psi_1\rangle$ and impure $\hat{\rho}_2$ state can be calculated in the same way using eq. 2.7

$$F(\psi_1, \rho_2) = \text{Tr}\left[|\psi_1\rangle\langle\psi_1|\,\hat{\rho}_2\right] = 2\pi \int_{-\infty}^{\infty}\int_{-\infty}^{\infty} W_1(x,p)W_2(x,p)\,dxdy \qquad (2.12)$$

where W_1 and W_2 are the Wigner functions of the states.

Trace distance

Another useful metric for comparing two quantum states is the trace distance T, which similar to the fidelity, is a measure of the distinguishably of between two quantum states and takes the value $0 \leq T(\hat{\rho}_1, \hat{\rho}_2) \leq 1$. Compared to the fidelity of the interpretation of the trace distance is reversed, so that a value of 0 or 1 corresponds to identical or orthogonal states respectively. It is defined as half of the trace distance between the two states [20] $T(\hat{\rho}_1, \hat{\rho}_2) = \frac{1}{2}||\hat{\rho}_1 - \hat{\rho}_2||_{\text{tr}}$, which for hermitian matrices reduces to

$$T(\hat{\rho}_1, \hat{\rho}_2) = \tfrac{1}{2}\text{Tr}\left[\sqrt{(\hat{\rho}_1 - \hat{\rho}_2)^2}\right] \qquad (2.13)$$

Here $||M||_{\text{tr}}$ is the trace norm defined as $||M||_{\text{tr}} = \sqrt{M^\dagger M}$. The trace distance is connected to the fidelity through the Fuchs-van de Graaf inequality $1 - \sqrt{F(\hat{\rho}_1, \hat{\rho}_2)} \leq T(\hat{\rho}_1, \hat{\rho}_2) \leq \sqrt{1 - F(\hat{\rho}_1, \hat{\rho}_2)}$, where it provides useful upper and lower bounds of the fidelity. For the case of either states being pure, the inequality reduces to $1 - F(\psi_1, \hat{\rho}_2) \leq T(\psi_1, \hat{\rho}_2)$ [21].

2.1.4 Loss model

Most linear loss mechanisms acting on a signal state is modelled as state $\hat{\rho}$ being transmitted through a beamsplitter with vacuum as its other input and a transmittance $T = \eta$ corresponding to the loss. The result is that the signal state intensity is reduced by η while the signal mode is admixed with $1 - \eta$ vacuum. The effect of interfering two mode operators $\hat{a}_1$ and $\hat{a}_2$ on a beamsplitter is typically written as

$$\begin{pmatrix}\hat{b}_1 \\ \hat{b}_2\end{pmatrix} = \begin{pmatrix}\sqrt{T} & \sqrt{1-T} \\ -\sqrt{1-T} & \sqrt{T}\end{pmatrix}\begin{pmatrix}\hat{a}_1 \\ \hat{a}_2\end{pmatrix} \quad \text{or} \qquad (2.14)$$

$$= \hat{B}^\dagger(T)\begin{pmatrix}\hat{a}_1 \\ \hat{a}_2\end{pmatrix}\hat{B}(T) \qquad (2.15)$$

with $\hat{B}(T) = \exp\left[\arccos\left(\sqrt{T}\right)(\hat{a}_1\hat{a}_2^\dagger - \hat{a}_1^\dagger\hat{a}_2)\right]$ being the beamsplitter operator. In the density matrix picture the loss is then considered as the partial trace over the transmitted vacuum mode v' after transformation by the beamsplitter

$$\hat{\rho}_{s'}' = \mathrm{Tr}_{v'}\left[\hat{B}^\dagger(\eta)\hat{\rho}_s \otimes |0\rangle_v \langle 0|_v \hat{B}(\eta)\right] \tag{2.16}$$

The matrix elements of $\hat{\rho}'$ can be calculated using the generalized Bernoulli transformation [22]

$$(\hat{\rho}')_{mn} = \langle m| \hat{\rho}_s' |n\rangle = \sum_{k=0}^\infty B_{m+k,m}(\eta)B_{n+k,n}(\eta) \langle m+k| \hat{\rho}_s |n+k\rangle \tag{2.17}$$

where $B_{m+k,m}(\eta) = \sqrt{\binom{n+k}{k}\eta^n(1-\eta)^k}$ is the binomial distribution. In the Wigner function picture linear loss η can be modelled as the convolution of the state with a complex Gaussian G_σ with variance $\sigma = \sqrt{(1-\eta)/2\eta}$

$$W_s'(x,p) = \frac{1}{\eta}\left(W_s \circ G_\sigma\right)\left(\tfrac{x}{\sqrt{\eta}}, \tfrac{p}{\sqrt{\eta}}\right) \tag{2.18}$$

2.2   Squeezed light

First observed by Slusher *et al.* in 1985, squeezed light is perhaps the most fundamental resource for CV quantum information processing (CVQIP) and have been used to facilitate quantum improved protocols across all three fields of quantum computation, sensing and communication. For a detailed review of the history of squeezed light and its importance, see the excellent review by Andersen *et al.* [23]. Mathematically squeezing is expressed by the squeezing operator

$$\hat{S}(\xi) = \exp\left(\tfrac{\xi}{2}\hat{a}^{\dagger 2} - \tfrac{\xi^*}{2}\hat{a}^2\right) \tag{2.19}$$

A squeezed vacuum state, $|\xi\rangle = \hat{S}(\xi)|0\rangle$, is a common starting point of many CVQIP protocols, including our non-Gaussian state and distributed sensing projects, since it can readily be generated experimentally. It has the properties of the expectation value of the quadrature operator being zero $\Delta\hat{q}_\theta = 0$ for any squeezing rate and along any quadrature angle, similar to the vacuum state, while the variance is "squeezed" $\langle\Delta\hat{x}^2\rangle = \frac{1}{2}e^{-2r}$ and "antisqueezed" $\langle\Delta\hat{p}^2\rangle = \frac{1}{2}e^{2r}$ along orthogonal quadrature angles as compared to the vacuum state.

Generation

The mathematical squeezing operator can be implemented through a type-0 degenerate parametric down-conversion process [15]. Such a process can be physically realized by transmitting a pump field at frequency 2ω through a second-order nonlinear medium, in order to down-convert a photon from the pump field into a photon pair in a signal field at frequency ω. The Hamiltonian for such a process is

$$\hat{H} = \hbar\omega_0\hat{a}^\dagger\hat{a} + 2\hbar\omega_0\hat{b}^\dagger\hat{b} + i\hbar\chi^{(2)}\left(\hat{a}^2\hat{b}^\dagger - \hat{a}^{\dagger 2}\hat{b}\right) \tag{2.20}$$

where a and b denotes the signal and pump field modes respectively and $\chi^{(2)}$ is the second-order nonlinear susceptibility coefficient of the medium along the direction of pump field propagation, often simply called the nonlinearity. It is assumed that the pump field is a strong coherent field, so that it can be described classically as $\beta e^{-i2\omega t}$. One can then write the Hamiltonian in the interaction picture as $\hat{H}_{int} = i\hbar\chi^{(2)}\left(\beta^*\hat{a}^2 - \beta\hat{a}^{\dagger 2}\right)$ so that the evolution operator $\hat{U}(t)$ takes the form of the squeezing operator

$$\hat{U}(t) = e^{-i\hat{H}_{int}t/\hbar} = e^{\chi^{(2)}(\beta^*\hat{a}^2 - \beta\hat{a}^{\dagger 2})t} = \hat{S}(\xi) \tag{2.21}$$

with $\xi = 2\chi^{(2)}\beta t$. Here the interaction time t is equivalent to the interaction length, that is the physical length of the nonlinear medium. It is therefore clear that in order to generate strong squeezing, one needs to maintain a strong pump field through a long piece of material with high nonlinearity.

2.2.1 Optical parametric oscillator

Since $\chi^{(2)}$ is small for most optical materials the squeezing levels obtainable by a simple single-pass setup of the pump field through the nonlinear material very is low. Pulsed light can be used to circumvent this issue, but to generate a continuous wave squeezed field, the dominant solution has been to place the nonlinear material inside an optical cavity at resonance with the down-converted fields.
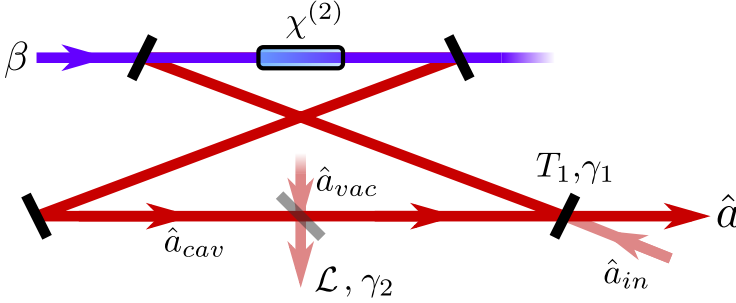
Figure 2.1: Schematic of OPO model parameters

For an optical cavity the *resonance spectrum* consist of a comb of Lorentzian shaped resonance peaks, centred at the fundamental frequency ω_0 and with spacing $\Delta_\omega = 2\pi/t_{cav}$ called the free spectral range of the cavity, where $t_{cav} = l_{cav}/c$ is the round-trip time and l_{cav} is optical cavity round-trip length. The half-width at half-maximum (HWHM) of the resonance peaks is called the bandwidth of the cavity and is equivalent to the decay rate γ of the circulating field and is proportional to the total round-trip loss r. The two main contributing factors can be thought of as the output coupler transmittance T_1 and the intra-cavity losses $\mathcal{L}$, so that $r = \sqrt{1-T_1}\sqrt{1-\mathcal{L}}$. Each loss factor contributes to the bandwidth as $\gamma_1 = (1 - \sqrt{1-T_1})/t_{cav} \approx T_1/2t_{cav}$ and $\gamma_2 = (1 - \sqrt{1-\mathcal{L}})/t_{cav} \approx \mathcal{L}/2t_{cav}$, for $T_1, \mathcal{L} \ll 1$, so that the total decay rate $\gamma = \gamma_1 + \gamma_2$ is the HWHM bandwith of the cavity.

To model the OPO behaviour we use the field operators in both time and frequency domain. In a frame rotating with the central frequency ω_0 the two domains are connected by the symmetric Fourier transformation as

$$\hat{a}(\omega) = \frac{1}{\sqrt{2\pi}} \int_{-\infty}^{\infty} e^{i\omega t}\hat{a}(t) \; dt \tag{2.22}$$

$$\hat{a}(t) = \frac{1}{\sqrt{2\pi}} \int_{-\infty}^{\infty} e^{-i\omega t}\hat{\omega}(t) \; d\omega \tag{2.23}$$

Using the equation of motion of the intra-cavity field $\hat{a}_{cav}$ as an ansatz we can derive the correlation functions of the cavity output mode $\hat{a}_{out}$, from which we can derive the quadrature correlation functions. In the following only the main results will be presented, while the full derivation can be followed in [24] and originally in [25]. Using the parameters shown in fig. 2.1 the equation of motion in the Heisenberg picture is

$$\frac{d\hat{a}_{cav}(t)}{dt} = \epsilon e^{i\phi}\hat{a}_{cav}^\dagger(t) - \gamma\hat{a}_{cav}(t) + \sqrt{2\gamma_1}\hat{a}_{in}(t) + \sqrt{2\gamma_1}\hat{a}_{vac}(t) \tag{2.24}$$

where $\epsilon = \chi^{(2)}|\beta| = \gamma\sqrt{P_p/P_{thr}}$ is the pump rate and ϕ is the pump phase offset. The OPO threshold condition is then $\epsilon = \gamma$ corresponding to the cavity field building faster then it decays. Above threshold ($\epsilon > \gamma$) the cavity output field will have a coherent amplitude and show simple Poissonian statistics, while if the OPO is pumped below its threshold ($\epsilon < \gamma$) the output field will show sub-Poissonian statistics, allowing for *squeezing* to be observed. Using that $\hat{a}_{in} + \hat{a}_{out} = \sqrt{2\gamma_1}\hat{a}_{cav}$ the equation of motion can be solved, yielding the time domain correlation functions of the output field operator

$$\langle \hat{a}(t)\hat{a}(t')\rangle = \frac{\epsilon\gamma_1 e^{i\phi}}{2}\left(\frac{e^{-(\gamma-\epsilon)|t-t'|}}{\gamma-\epsilon} + \frac{e^{-(\gamma+\epsilon)|t-t'|}}{\gamma+\epsilon}\right) \tag{2.25}$$

$$\langle \hat{a}^\dagger(t)\hat{a}(t')\rangle = \frac{\epsilon\gamma_1}{2}\left(\frac{e^{-(\gamma-\epsilon)|t-t'|}}{\gamma-\epsilon} - \frac{e^{-(\gamma+\epsilon)|t-t'|}}{\gamma+\epsilon}\right) \tag{2.26}$$

Here the output mode subscript has been dropped for simplicity. Using the definition of the x and p quadrature operators from eq. 2.3 their time domain correlation functions can be found using the field correlation functions above. Setting $\phi = \pi/2$ for simplicity, corresponding to an amplitude squeezed state, we find that

$$\begin{aligned}
\langle \hat{x}(t)\hat{x}(t')\rangle &= \frac{\delta(t-t')}{2} - \langle \hat{a}(t)\hat{a}(t')\rangle + \langle \hat{a}^\dagger(t)\hat{a}(t')\rangle \\
&= \frac{\delta(t-t')}{2} + \frac{\gamma_1\epsilon}{\gamma+\epsilon}e^{-(\gamma+\epsilon)|t-t'|} \\
&= \frac{\delta(t-t')}{2} + \langle : \hat{x}(t)\hat{x}(t') :\rangle \\
\langle \hat{p}(t)\hat{p}(t')\rangle &= \frac{\delta(t-t')}{2} + \langle \hat{a}(t)\hat{a}(t')\rangle + \langle \hat{a}^\dagger(t)\hat{a}(t')\rangle \\
&= \frac{\delta(t-t')}{2} + \frac{\gamma_1\epsilon}{\gamma-\epsilon}e^{-(\gamma-\epsilon)|t-t'|} \\
&= \frac{\delta(t-t')}{2} + \langle : \hat{p}(t)\hat{p}(t') :\rangle
\end{aligned}$$

(2.27)

(2.28)

Here : . : denotes the normal-ordered form, which is useful to work with since it does not include the $\frac{\delta(t-t')}{2}$ vacuum term. Using the Wiener-Khintchine theorem we can obtain the quadrature power spectrum $S(\omega)$ as the Fourier transform of the quadrature auto-correlation function $S_q(\omega) = \int_\infty^\infty \langle \hat{q}(\tau)\hat{q}(0)\rangle e^{i\omega t}\, d\tau$, where $\langle \hat{q}(\tau)\hat{q}(0)\rangle$ is simply $\langle \hat{q}(t)\hat{q}(t')\rangle$ for $\tau = t - t'$ corresponding to the correlations of the continuous OPO output field being independent on the time of day. Inserting eq. 2.27 and 2.28 we obtain the spectral densities of the quadrature operators

of the OPO output field

$$S_x(\omega) = \frac{1}{2} - \frac{2\epsilon\gamma_1}{(\gamma + \epsilon)^2 + \omega^2} = \frac{1}{2} - \frac{2\eta\epsilon\gamma}{(\gamma + \epsilon)^2 + \omega^2} \qquad (2.29)$$

$$S_p(\omega) = \frac{1}{2} + \frac{2\epsilon\gamma_1}{(\gamma - \epsilon)^2 + \omega^2} = \frac{1}{2} + \frac{2\eta\epsilon\gamma}{(\gamma - \epsilon)^2 + \omega^2} \qquad (2.30)$$

In the final form the output coupler term γ_1 have been replaced by an efficiency term η and the total OPO decay rate. From there it is easy to see that when $\eta = 1$ the output state is pure since the product $S_x S_p = 1/4$ saturates the Heisenberg uncertainty. These spectral densities are very useful, as they are proportional to the spectral densities of the photocurrents produced by homodyne detection when locked to the corresponding quadrature phase and so can be used to fit experimental data in order to extract model parameters. If a quadrature other than x or p is measured the spectral density is given by a geometric combination of the x- and p-spectra

$$S_{q_\theta}(\omega) = S_x(\omega)\cos^2\theta + S_p(\omega)\sin^2\theta \qquad (2.31)$$

corresponding to the definition of $\hat{q}_\theta$, so that $\theta = 0$ becomes the angle where we will measure squeezing (x quadrature) due to our choice of squeezing angle ($\phi = \pi/2$). Plots showing the effect of pump rate and loss on the generated squeezing and anti-squeezed levels as well as the frequency and phase dependence of the power spectrum are shown in fig. 2.2.
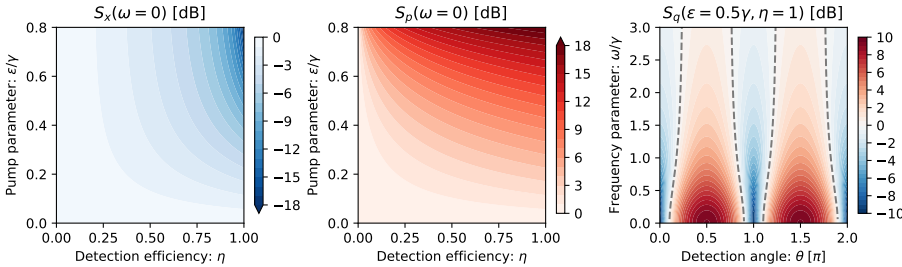
Figure 2.2: Contour plots of eq. 2.29, 2.30 and 2.31 in dB scale, showing the behaviour of the power spectrum for squeezed vacuum. Dotted lines show the vacuum noise crossing

From fig. 2.2(left+middle) we see that the squeezing level is more sensitive to loss than the anti-squeezing and that the observed squeezing is highly reduced for for non-zero loss even for high pump rates. From fig. 2.2(right) we see the typical "McDonalds" squeezing curves when looking across the detection angle

at a fixed frequency and that a larger part of the phase space (quadrature angles) is anti-squeezed then squeezed. This fact will be relevant when we want to use a single temporal mode function to encompass a non-Gaussian state generated from squeezed vacuum.

2.2.2   As a resource for non-Gaussian state generation

Squeezed light can be used as a resource for the conditional generation of non-Gaussian state, by relying on the highly non-Gaussian nature of photon detection. This concept was concretized in 1997 by Dakna *et al.*, when they proposed a simple scheme to generate a state similar to a small amplitude Schrödinger's cat state by subtracting photons from a squeezed vacuum using a beamsplitter and counting them [26]. We call these states photon subtracted squeezed vacuum states; PSSqV. The first experimental demonstrations with pulsed light were realized in 2004 [27] and 2006 [28] and using using continuous wave light in 2006 [29] and 2007 [30]. Many more advanced schemes have later followed, such as the first demonstrations of two photon subtraction [31] and three photon subtraction [32]. Proposals have also been made on how to generate state similar to larger amplitude Schrödinger's cat states [33, 34] as well as experimental demonstrations [35–37]. Relevant to us is the first demonstrations of non-Gaussian states at the telecom wavelength showing Wigner negativity [38, 39]. Highly pure PSSqV states have also been generated by tight optical filtering of the subtracted squeezed vacuum mode [40]. Recently the generation of optical Schrödinger's cat like states have also been proposed for a generalized photon subtraction scheme [41]. For further details on the various production schemes and possible applications of non-Gaussian states see the 2020 review by Lvovsky *et al.*

In the following section we will, in short, present two models of the single PSSqV state (1-PPSqV), as this will be the state we generate experimentally in cha. 5.

2.3   Photon subtracted squeezed vacuum

Here we first briefly introduce, as a reference, the idealized representation of the photon subtracted squeezed vacuum state as a single mode state generated from a number resolving detector. Afterwards a more realistic model of the procedure required to experimentally generate the photon subtracted squeezed vacuum state is presented. The model was developed by Mølmer in 2006 [42] in connection to the first experimental demonstration of the procedure the same

year [43] and is based on the multi-mode description of the OPO output field. A more detailed walkthrough of the model, included derivation of many intermediary terms, is given in the thesis of Neergaard-Nielsen[24].

The basic principle of the generation scheme is to transmit a squeezed vacuum state through a weakly reflective beamsplitter and then detect one or more photons in the reflected *trigger* path, thereby collapsing the state into a photon subtracted squeeed vacuum state.

2.3.1 Single mode with number-resolved detection

In the single mode picture the state incident on the beamsplitter is written as $|\psi_{in}\rangle = |\xi\rangle_s |0\rangle_t$ and the output state calculated as $|\psi_{bs}\rangle = \hat{B}(T) |\psi_{in}\rangle$, with the beamsplitter operator of eq. 2.15 and using the formula $\hat{B}(T) |n, 0\rangle = \sum_{k=0}^n \sqrt{B_k^n(T)} |k, n-k\rangle$ [22]. By conditioning this two-mode state on the detection of m photons in the trigger mode the state in the signal subspace will collapse into

$$|\psi_m\rangle_s = \frac{t \langle m|\psi_{bs}\rangle}{\sqrt{\Pr_t(m)}} = \frac{1}{\sqrt{\Pr_t(m)}} \sum_{n=0}^\infty \langle n+m|\xi\rangle \sqrt{B_n^{n+m}(T)} |n\rangle_s \qquad (2.32)$$

where $\Pr_t(m) = \sum_n |\langle n, m|\psi_{bs}\rangle|^2$ is the probability of detecting the m photons in the trigger mode. We see that depending on the parity of m the 1-PSSqV state will be a super position of either even or odd photon numbers. For the case of subtracting a single photon the state becomes equivalent to a slightly less squeezed single photon state [44]

$$|\psi_1\rangle_s = \frac{1}{\sinh s} \hat{a} \hat{S}(s) |0\rangle = \hat{S}(s) |1\rangle \qquad (2.33)$$

where $s = \text{arctanh}(T \tanh r) \leq r$ is a modified squeezing parameter owing to the admixing of vacuum through the unused port of the beamsplitter used to subtract the single photon. That is a 1-PSSqV state generated from initial squeezing parameter r and beamsplitter transmittance T corresponds to a squeezed single photon with squeezing parameter s. We also note that $s \to r$ as $t \to 1$. The number state expansion and Wigner function of the 1-PSSqV state is summarized below, where $k_{sqv}(r, \phi, n+1)$ is the coefficient of the squeezed vacuum state from tab. 2.1.

State	$|\psi\rangle$	Number state expansion
1-PSSqV	$|\text{sqv-1}\rangle = \hat{a}\hat{S}(\xi)|0\rangle$	$\frac{\sqrt{1+n}}{\sinh r}k_{sqv}(r,\phi,n+1)$
	$W(x,p)$	Phase space distribution
	W_{sqv-1}	$W_1(xe^{-r},pe^{r})$

2.3.2 Conditioned multi-mode model

The multi-mode model is based on the covariance matrix formalism. Here a two mode Gaussian state can always be rotated such that its covariance matrix has the generic form

$$\Gamma = \left(\begin{array}{c|c} \Gamma_{AA} & \Gamma_{AB} \\ \hline \Gamma_{\mathbf{AB}} & \Gamma_{\mathbf{BB}} \end{array}\right) = \begin{pmatrix} \Gamma_{11} & 0 & \Gamma_{13} & 0 \\ 0 & \Gamma_{22} & 0 & \Gamma_{24} \\ \Gamma_{13} & 0 & \Gamma_{33} & 0 \\ 0 & \Gamma_{24} & 0 & \Gamma_{44} \end{pmatrix} \tag{2.34}$$

corresponding to no x-p correlations in either subsystem. While building our model we utilize that the vacuum noise term of the auto-correlation functions does not influence the transformation of the autocovariance. We therefore conveniently choose the normal-ordered form of the auto-correlations and simply add the vacuum term in the end to obtain the full covariance matrix expression of the final two mode state. A schematic of the sequential steps involved in building the model is shown in fig. 2.3.
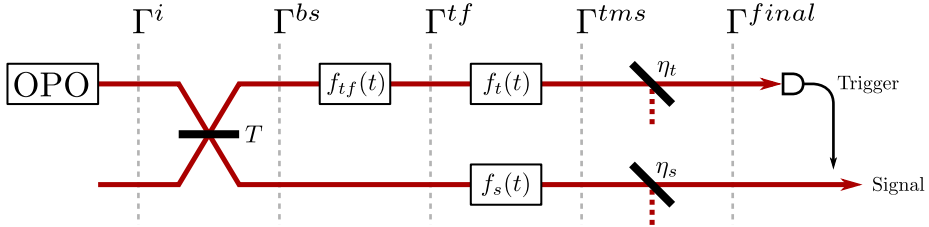
Figure 2.3: Outline of multi mode model structure

1. **OPO output** The *initial* uncorrelated two-mode state is then the squeezed vacuum state in the signal mode (AA) and vacuum in the trigger mode (BB), with the signal subspace having the entries : $\Gamma_{11}^{i}(t-t') := 2\langle : \hat{x}(t)\hat{x}(t') : \rangle$

and $: \Gamma_{22}^i(t - t') := 2 \langle : \hat{p}(t)\hat{p}(t') : \rangle$ from eq. 2.27 and 2.27 respectively.

$$: \Gamma^i := \left(\begin{array}{c|c} : \Gamma_{AA}^i(t - t') : & 0 \\ \hline 0 & 0 \end{array} \right) \tag{2.35}$$

2. **Tapping** Part of the signal mode is then coupled to the trigger mode by a beamsplitter interaction. The two-mode state after the *beamsplitter* is calculated as $: \Gamma^i :\rightarrow: \Gamma^{bs} := B(T) : \Gamma^i : B(T)^T$ with the $B(T)$ matrix similar to the one used in eq. 2.14:

$$: \Gamma^{bs} := \begin{cases} : \Gamma_{AA}^{bs} : & = T : \Gamma_{AA}^i : \\ : \Gamma_{AB}^{bs} : & = -\sqrt{T(1-T)} : \Gamma_{AA}^i : \\ : \Gamma_{BB}^{bs} : & = (1-T) : \Gamma_{AA}^i : \end{cases} \tag{2.36}$$

3. **Trigger filtering** The trigger mode is then *frequency filtered* to select only the central frequency resonance mode of the OPO output. The transformation $: \Gamma^{bs} : \rightarrow : \Gamma^{tf} :$ is calculated as the convolution of the covariance matrix elements with the trigger filter function. We use a single-sided exponential function as the filter function, corresponding to the temporal response of a physical filter cavity as used in our experimental setup (optical lowpass filter). The trigger mode subspace (BB) is filtered twice, while the covariance subspace (AB) only once, with the integrations from $]-\infty, t']$ for AB and from $]-\infty, t]$ and $]-\infty, t']$ for BB, corresponding to the output field of the frequency filter at time t not being affected by the input field at some later time:

$$: \Gamma^{tf} := \begin{cases} : \Gamma_{AA}^{tf} : & =: \Gamma_{AA}^{bs} : \\ : \Gamma_{AB}^{tf} : & = \kappa \int : \Gamma_{AB}^{bs}(t - \tau) : e^{-\kappa(t'-\tau)} \, d\tau \\ : \Gamma_{BB}^{tf} : & = \kappa^2 \int \int : \Gamma_{BB}^{bs}(\tau - \tau') : e^{-\kappa(t+t'-\tau-\tau')} \, d\tau d\tau' \end{cases} \tag{2.37}$$

4. **Temporal mode selection** The subtraction and detection of a photon from the OPO output field, leads to the conditioned state existing as altered temporal correlations within a distinct a temporal mode around the trigger time. By temporally filtering the mode operator of the otherwise stationary OPO output field we can define an operator for the temporal mode as $\int f_s(t)\hat{a}_s(t)dt$, where $f_s(t)$ is a filter function corresponding to the desired temporal mode. Since we are filtering the mode operator, the temporal mode function (TMF) is an amplitude filter and should therefore be normalized as $\int |f_s(t)|^2 dt = 1$. Intuitively the temporal mode of the 1-PSSqV should resemble the autocovariance function (eq. 2.27 and 2.28) of the OPO output field around the trigger time, since it is only within these correlations that entanglement between the trigger and signal mode can lead to the signal mode being affected by the photon subtraction

in the trigger mode. In practice the TMF is applied to the recorded time traces during data analysis, though it can be applied directly in the experiment by shaping the amplitude of the LO according to the TMF or by filtering the homodyne photocurrent if the conditioned state has been filtered to have a TMF resembling the electrical filter response as in [40]. An advantage of applying the TMF in post, is that its shape can be optimized to maximize e.g. the Wigner negativity of the reconstructed state. This is important as choosing a wrong TMF can lead to either not including the full correlations of the conditioned state or including some of the background squeezed vacuum. To this end we therefore choose not to explicitly choose the TMF in our model. The transformation of the state after the trigger filtering $: \Gamma^{tf} : \rightarrow : \Gamma^{tms} :$ into the *temporal mode selected* state is then calculated by the integration of the temporal correlations around the trigger time weighted by the TMF and so here the all integrations are from $]-\infty, \infty[$.

$$: \Gamma^{tms} := \begin{cases} : \Gamma^{tms}_{AA} : & = \int \int f_s(t) f_s(t') : \Gamma^{tf}_{AA} : \, dt dt' \\ : \Gamma^{tms}_{AB} : & = \int \int f_s(t) f_t(t') : \Gamma^{tf}_{AB} : \, dt dt' \\ : \Gamma^{tms}_{BB} : & = \int \int f_t(t) f_t(t') : \Gamma^{tf}_{BB} : \, dt dt' \end{cases} \tag{2.38}$$

5. **Channel loss** The loss of the trigger and signal channel transform the state as $: \Gamma^{tms} : \rightarrow : \Gamma^f := \underline{\eta} : \Gamma^{tms} : \underline{\eta}$ where $\underline{\eta}$ is a two-mode diagonal matrix with $\sqrt{\eta_s}$ and $\sqrt{\eta_t}$ entries corresponding to mixing the signal and trigger modes with auxiliary vacuum modes using beamsplitter matricies $B(\eta_s)$ and $B(\eta_t)$ as in step 2. The full covariance matrix of the final two-mode state just before detection in trigger channel is then obtained by adding back the vacuum noise as $: \Gamma^f : \rightarrow \Gamma^f = \hat{\mathbb{1}} + : \Gamma^f ::$

$$\Gamma^f = \begin{cases} \Gamma^f_{AA} & = \eta_s : \Gamma^{tms}_{AA} : +1 \\ \Gamma^f_{AB} & = \sqrt{\eta_s \eta_t} : \Gamma^{tms}_{AB} : \\ \Gamma^f_{BB} & = \eta_t : \Gamma^{tms}_{BB} : +1 \end{cases} \tag{2.39}$$

Having already chosen the mode function of the trigger filter we are free to choose the temporal mode functions $f_t(t)$ and $f_s(t)$ of the trigger and signal modes respectively. For the trigger mode we choose a delta function $f_t(t) = \delta(t)$, corresponding to a very narrow timing resolution of the photon detector compared to the length of the correlations of the detected field, which is reasonable for a our setup with a timing resolution of 70 ps and a OPO bandwith of 8 MHz $\propto$ 125 ns. For the signal mode we choose a double exponential function $f_s(t) = \sqrt{\gamma_s} e^{-\gamma_s t}$ of width γ_s, which should be a reasonable guess since the ideal mode function for low gain and no trigger filtering have been found to be a double exponential of width equal to the OPO bandwidth [45]. With these

choices of mode functions and following the approach outlined above, analytical expressions for the entries of Γ^f was obtained by Neergaard-Nielsen [24]:

$$\Gamma_{11}^f = 1 + T\eta_s\Gamma_{AA}^{(-)} \qquad\qquad \Gamma_{22}^f = 1 + T\eta_s\Gamma_{AA}^{(+)}$$
$$\Gamma_{33}^f = 1 + (1-T)\eta_t\Gamma_{BB}^{(-)} \qquad \Gamma_{44}^f = 1 + (1-T)\eta_t\Gamma_{BB}^{(+)} \qquad (2.40)$$
$$\Gamma_{13}^f = \sqrt{T(1-T)}\sqrt{\eta_s\eta_t}\Gamma_{AB}^{(-)} \qquad \Gamma_{24}^f = \sqrt{T(1-T)}\sqrt{\eta_s\eta_t}\Gamma_{AB}^{(+)}$$

with

$$\Gamma_{AA}^{(\pm)} = \frac{\pm 4\gamma\epsilon(\gamma\mp\epsilon+2\gamma_s)}{(\gamma\mp\epsilon)(\gamma\mp\epsilon+\gamma_s)}$$

$$\Gamma_{BB}^{(\pm)} = \frac{\pm 2\gamma\epsilon\kappa}{(\gamma\mp\epsilon)(\gamma\mp\epsilon+\gamma_s)} \qquad\qquad (2.41)$$

$$\Gamma_{AB}^{(\pm)} = \frac{\mp 4\gamma\epsilon\kappa(\gamma\mp\epsilon+\kappa+\gamma_s)}{(\gamma\mp\epsilon)(\gamma\mp\epsilon+\kappa)(\gamma\mp\epsilon+\gamma_s)(\kappa+\gamma_s)}$$

We note that the x and p correlations between the two modes remain symmetrical with respect to the sign change of ϵ. With the covariance matrix of the two mode system just before a trigger click in hand, we now turn our attention to the calculation of the resulting state conditioned on a click in the trigger mode. The Wigner function of an arbitrary N-mode Gaussian state, described by its covariance matrix Γ, can be calculated as $W_\Gamma(\xi) = [\pi^N\sqrt{\det\Gamma}]^{-1}e^{-\xi^T\Gamma\xi}$ and the Wigner function of the conditioned state as

$$W_{cond}(\xi_s) = \frac{2\pi\int\int W_\Gamma(\xi)W_E(\xi_t)\,d\xi_t^2}{2\pi\int W_\Gamma(\xi)W_E(\xi_t)\,d\xi^4} \qquad (2.42)$$

where $\xi_s = (x_s, p_s)$, $\xi_t = (x_t, p_t)$ and $\xi = (x_s, p_s, x_t, p_t)$ is the signal, trigger and two mode coordinates and $W_E(x,p) = \frac{1}{2\pi} - \frac{1}{\pi}e^{-x^2-p^2}$ is the Wigner function of the trigger mode on-POVM $\hat{E}_t^{on} = \hat{\mathbb{1}}_t + |0\rangle_t\langle 0|$, calculated in similar fashion as eq. 2.6. The form of eq. 2.42 can be understood by looking at the equivalent expression for density matrices $\hat{\rho}_s^{on} = \text{tr}_t[\hat{E}_t^{on}\hat{\rho}_\Gamma]/\text{tr}_{s,t}[\hat{E}_t^{on}\hat{\rho}_\Gamma]$ [24], where the traces can be evaluated using eq. 2.7. Here it is more clear that the conditioned state $\hat{\rho}_s^{on}$ is obtained by operating on the state $\hat{\rho}_\Gamma$ with the on-POVM and tracing out the trigger mode corresponding to integrating the product of the state and on-POVM Wigner functions across the trigger mode. Using the generic form of a covariance matrix of a (properly rotated) two mode Gaussian state (eq. 2.34) an analytical expressions for eq. 2.42 can be found as

$$W_{cond}(\xi_s) = \left[\frac{\exp\left(-\frac{x_s^2}{\Gamma_{11}} - \frac{p_s^2}{\Gamma_{22}}\right)}{\pi\sqrt{\Gamma_{11}\Gamma_{22}}} - \frac{2\exp\left(-\frac{(1+\Gamma_{33})x_s^2}{\Gamma_{11}(1+\Gamma_{33})-\Gamma_{13}^2} - \frac{(1+\Gamma_{44})p_s^2}{\Gamma_{22}(1+\Gamma_{44})-\Gamma_{24}^2}\right)}{\pi\sqrt{(\Gamma_{11}(1+\Gamma_{33})-\Gamma_{13}^2)(\Gamma_{22}(1+\Gamma_{44})-\Gamma_{24}^2)}}\right]$$
$$\times \left[1 - \frac{2}{\sqrt{(1+\Gamma_{33})(1+\Gamma_{44})}}\right]^{-1} \qquad (2.43)$$

Here the first term in the numerator is the unconditioned state $W_{uncond}(\xi_s) = [\pi\sqrt{\Gamma_{11}\Gamma_{22}}]^{-1}e^{-x_s^2/\Gamma_{11}-p_s^2/\Gamma_{22}}$ corresponding to having simply traced out the trigger mode and the denominator term is the probability of a trigger click $\mathrm{pr}_{on} = 1 - 2[\sqrt{(1+\Gamma_{33})(1+\Gamma_{44})}]^{-1}$.

A parameter accounting for the effect of fake counts can be included in the model as a mixing of the conditioned state with the unconditioned state by a factor Ξ, called the modal purity, which is the fraction of true to total (true+fake) counts:

$$W_{cond}(\xi_s, \Xi) = \Xi W_{cond}(\xi_s) + (1 - \Xi)W_{uncond}(\xi_s) \qquad (2.44)$$

In this perspective fake counts are any clicks from the SSPD not originating from the detection of a subtracted photon. These are typically the detector dark counts and counts from scattered light, mainly the control beams used for locking and phase control of the experiment. Our full model is then obtained by inserting the covariance matrix entries of eq. 2.40 into eq. 2.44. The parameters of the model are summarized in tab. 2.3.

γ	Total OPO decay rate, OPO bandwidth
ϵ	Pump rate, $\gamma\sqrt{P/P_{thr}}$
T	Tapping ratio, beamsplitter transmittance
κ	Trigger filter width, FC bandwidth
γ_s	Signal temporal mode width
η_s	Total signal channel efficiency
η_t	Total trigger channel efficiency
Ξ	Modal purity

Table 2.3: Parameters of the multi mode model with on/off detection for photon-subtracted squeezed vacuum generation.

Optimal filter and mode functions

Here we investigate the effects of the widths of the signal TMF and the trigger filter in our model on the Wigner negativity of the heralded state. We set all efficiencies to unity and use a beamsplitter ratio of $T \approx 1$. First we see the effect of TMF width by setting the trigger filter width to infinity. This is of course nonsensical in the real experiment, but will allow us to isolate the effect. We then see if the trigger width affects the optimal TMF width and finally use the optimal TMF width to see the effect of the trigger width. The results are shown in fig. 2.4.
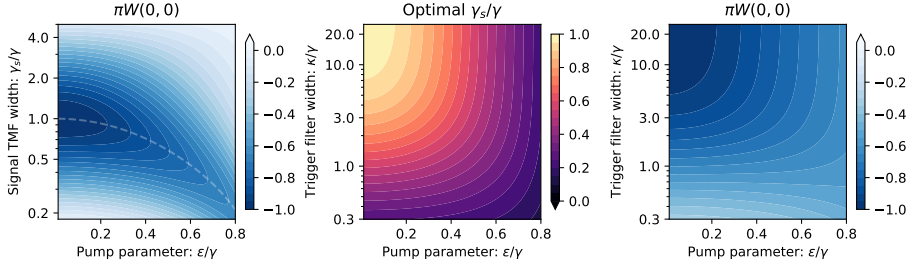
Figure 2.4: Effect of signal TMF width and trigger filter width on the Wigner negativity predicted by the model.

For the isolated TMF width we see that as the pump rate increases the optimal filter width decreases as well as the obtained Wigner negativity. The reduction in Wigner negativity can be understood as the bandwidth of the x and p quadrature being pushed apart by the epsilon term in the denominator of eq.2.29 and 2.30. The larger the pump rate is the more the temporal mode of the state is skewed and the less a single temporal mode function can encompass it. The shortening of the optimal TMF width can then be attributed to the shortening of the anti-squeezed bandwidth weighing heavier than the lengthening of the squeezed bandwith, since more of the phase space is anti-squeezed than squeezed. We then see that the trigger filter width should at least be 8 times larger than the OPO bandwidth to not cause the optimal TMF width to decrease and thereby decreasing the Wigner negativity. Though here we have to keep in mind that we are using a sharp double exponential function as our TMF and that the effect of the trigger filter is to smoothen out the temporal correlations and so using a different TMF shape could negate this effect. It is also worth keeping in mind that while the TMF is applied in the data analysis and therefore easily can be varied, the trigger filter width κ is set by the bandwidth of the physical filtering system and so might not be easy adjust or even possible to adjust.

Loss mechanisms
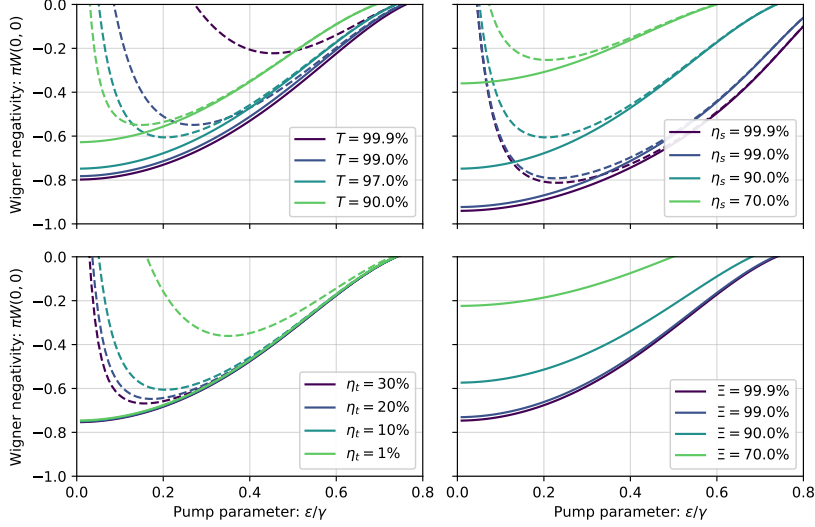
Figure 2.5: Wigner negativity as a function of pump rate for various values of T, η_t, η_s and Ξ. Values a unity unless otherwise.

Here we investigate the effect of the remaining parameters of the model; T, η_s, η_t and Ξ. If we disregard their effect on the modal impurity their behaviour is straight forward; if they are decreased so is the Wigner negativity as is seen from the solid lines of fig. 2.5. The reduction is worst for the signal channel efficiency and modal impurity, who essentially describe the same mechanism of mixing the signal state with vacuum. We see that the reduction is linear and that a decrease from 99% to 90% results in a roughly $\tilde{2}0\%$ reduction of the Wigner negativity across the pump range. The dashed lines include the coupling of the modal impurity to the other parameter and is modelled as

$$\Xi(\epsilon, T, \eta_t) = \frac{\langle \hat{n}_{tc} \rangle - \langle \hat{n}_{dc} \rangle}{\langle \hat{n}_{tc} \rangle} = \frac{\langle \hat{n} \rangle \, (1 - T) \eta_t}{\langle \hat{n} \rangle \, (1 - T) \eta_t - \langle \hat{n}_{dc} \rangle} \tag{2.45}$$

where $\langle \hat{n}_{tc} \rangle$ and $\langle n_{dc} \rangle$ is the total and dark count rates, respectively, observed from the SSPD when running the experiment and $\langle \hat{n} \rangle = \langle \hat{a}^\dagger(t) \hat{a}(t) \rangle = \gamma_1 \epsilon^2 / (\gamma^2 - \epsilon^2)$ is the photon number expectation value of the OPO output mode, which corresponds to the photon production rate in Hz. For the calculation of the dashed lines in fig. 2.5 zero internal loss is assumed ($\gamma_2 = 0 \rightarrow \gamma = \gamma_1$) and typical experimental parameters are used to set $\langle n_{dc} \rangle = (1 - \Xi') \langle \hat{n}' \rangle \, (1 - T') \eta_t' / \Xi'$ with $\epsilon'/\gamma = 0.4$, $T' = 0.97$, $\eta_t' = 0.1$, $\Xi' = 0.995$. The prime denotes the specific value

since the dark count rate should ideally not depend on any model parameters. In a real experiment the photon detector will unfortunately not only see dark counts but also counts from scattered light or unattenuated light from control beams and their relation to the different loss mechanism depends on the specific layout of the experimental setup.

Fidelity

Finally we investigate the fidelity between our model and a real odd cat state and the single mode 1-PSSqV. We use the Wigner function from our model and the Wigner functions from tab. 2.2 and 2.3.1 and calculate the fidelity using eq. 2.12 for various pump rates and amplitude or squeezing parameters. The result is shown in fig. 2.6. In general we see that the fidelity decreases with increasing pump rate, as we would expect from the decreased Wigner negativity and that to obtain a fidelity above 0.9 the pump rate has to be $\epsilon/\gamma < 0.4$. We also note that the fidelity to the single-mode 1-PSSqV is slightly higher than to the real odd cat state, while both a significantly higher than to the single photon fock state.
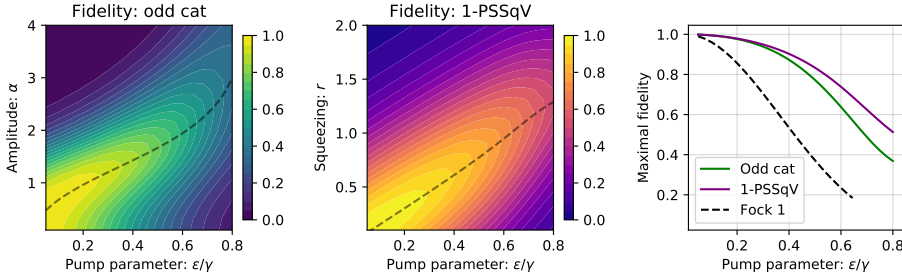
Figure 2.6: Fidelity between the conditioned multi-mode 1-PSSqV state and the real odd cat state and single-mode 1-PPSqV. All efficiencies of the model is set to unity with $T \approx 1$ and $\kappa \approx \infty$ and for each pump rate the optimal TMF width is used. Dotted lines indicate the maximal fidelity trajectory.

2.4   Homodyne detection

To characterize a continuous variable state a phase sensitive measurement of the light field is needed, though unfortunately there exists no current detector technology that can direly measure the phase of an incoming electromagnetic field at

optical frequencies. Instead interference can be used to reveal the desired phase information about a state. A measurement technique that does this is the balanced homodyne detection. Proposed in 1989 by Vogel [46] and experimentally demonstrated four years later [47], homodyne detection is a phase-sensitive measurement of the quantum noise of the electric field defined by an optical mode. From a practical point of view the homodyne measurement allows us to measure the quadrature values q_θ of a state along any angle in phase space. The measurement consists of interfering the signal field with a strong local oscillator (LO) field on a balanced (50:50) beamsplitter and measuring the two output modes with photodetectors. The resulting photocurrents are then subtracted to remove the classical noise of the LO field and amplify the phase sensitive noise of the signal field. To see how the scheme works we consider the field operators $\hat{a}_1$ and $\hat{a}_2$ of the two incoming fields

$$\hat{b}_1 = \frac{1}{\sqrt{2}}\left(\hat{a}_2 + \hat{a}_1\right) \quad \Rightarrow \quad \hat{n}_{b,1} = \hat{b}_1^\dagger \hat{b}_1 = \frac{1}{2}\left(\hat{n}_{a,2} + \hat{n}_{a,1} + \hat{a}_2^\dagger \hat{a}_1 + \hat{a}_1^\dagger \hat{a}_2\right)$$

$$\hat{b}_2 = \frac{1}{\sqrt{2}}\left(\hat{a}_2 - \hat{a}_1\right) \quad \Rightarrow \quad \hat{n}_{b,2} = \hat{b}_2^\dagger \hat{b}_2 = \frac{1}{2}\left(\hat{n}_{a,2} + \hat{n}_{a,1} - \hat{a}_2^\dagger \hat{a}_1 - \hat{a}_1^\dagger \hat{a}_2\right)$$

In the classical picture the photocurrent i produces by a diode is proportional to the absorbed field intensity $i \propto |E|^2$, while in the quantum regime its the photon number of the mode $\hat{a}$, so that $i \propto \hat{n}$. The subtracted photocurrent from the homodyne detector i_{hd} is then

$$i_{hd} = i_1 - i_2 \propto \hat{n}_{b,1} - \hat{n}_{b,2} = \hat{a}_2^\dagger \hat{a}_1 + \hat{a}_1^\dagger \hat{a}_2 \tag{2.46}$$

Setting $\hat{a}_1 = \hat{a}_s$ as our input signal state to be measured and $\hat{a}_2 = |\alpha_{lo}|e^{i\theta}$ as the local oscillator field, we get

$$i_{hd} \propto |\alpha_{lo}|\left(\hat{a}_s e^{-i\theta} + \hat{a}_s^\dagger e^{i\theta}\right) = \sqrt{2}|\alpha_{lo}|\hat{q}_{s,\theta} \tag{2.47}$$

2.4.1 Imperfect homodyne detection

Optical loss

Any loss, both before and during, the homodyne measurement can be modelled as the input signal state having been transmitted through a beamsplitter with transmission η, so that $\hat{a}_1 = \sqrt{\eta}\hat{a}_s + \sqrt{1-\eta}\hat{a}_v$. Inserting this expression into eq. 2.46 gives

$$i_{hd} \propto |\alpha_{lo}|\left[(\sqrt{\eta}\hat{a}_s + \sqrt{1-\eta}\hat{a}_v)e^{-i\theta} + (\sqrt{\eta}\hat{a}_s^\dagger + \sqrt{1-\eta}\hat{a}_v^\dagger)e^{i\theta}\right]$$
$$= \sqrt{2}|\alpha_{lo}|(\sqrt{\eta}\hat{q}_{s,\theta} + \sqrt{1-\eta}\hat{q}_v) \tag{2.48}$$

Unbalanced

If the detection is unbalanced ($T \neq \frac{1}{2}$) we cannot use eq. 2.46. Instead we have that

$$\hat{b}_1 = \sqrt{1-T}\hat{a}_2 + \sqrt{T}\hat{a}_1 \quad \Rightarrow \quad \hat{n}_{b,1} = (1-T)\hat{n}_{a,2} + T\hat{n}_{a,1} + \sqrt{T-T^2}(\hat{a}_2^\dagger\hat{a}_1 + \hat{a}_1^\dagger\hat{a}_2)$$

$$\hat{b}_2 = \sqrt{T}\hat{a}_2 - \sqrt{1-T}\hat{a}_1 \quad \Rightarrow \quad \hat{n}_{b,2} = T\hat{n}_{a,2} + (1-T)\hat{n}_{a,1} - \sqrt{T-T^2}(\hat{a}_2^\dagger\hat{a}_1 + \hat{a}_1^\dagger\hat{a}_2)$$

which leads to the homodyne photocurrent containing the uncorrelated photon number operators

$$i_{hd} = i_1 - i_2 \propto \hat{n}_{b,1} - \hat{n}_{b,2} \tag{2.49}$$

$$= (1-2T)(\hat{n}_{a,2} - \hat{n}_{a,1}) + 2\sqrt{T-T^2}(\hat{a}_2^\dagger\hat{a}_1 + \hat{a}_1^\dagger\hat{a}_2) \tag{2.50}$$

If we assume that the mode $\hat{a}_2$ contains the strong local oscillator field and that $T = \frac{1}{2} + k$, where k is some small fraction ($k \ll 1$) symbolizing the unbalance, it is possible to obtain a balanced photocurrent by attenuating the $\hat{b}_2$ mode by an amount $1 - \eta_2$ that compensates for the larger portion of the $\hat{a}_2$ mode. In [48] it was found that for small imbalances this compensation leads to a loss of the homodyne signal corresponding to the imbalance, i.e. for a 4% imbalance ($T = 48/52$) the compensation needed to balance the homodyne photocurrent results in a loss, equivalent to eq. 2.48, of 4%.

2.5   Quantum state reconstruction

We will now consider the essential task of estimating what quantum state we have measured, based on collected experimental data. If we imagine $\{|j\rangle\}$ as the set of all possible outcomes of our measurement, we can write our dataset $\{f_j\}$ as the frequency f_j of each outcome. In general if one has a model of a system it is possible to calculate the probability pr_j of having measured $|j\rangle$ given some specific model parameters. In our case of trying to estimate an unknown quantum state, the elements of its density matrix play the role of model parameters and our job is to find the density matrix $\hat{\rho}_0$ that maximizes the likelihood of providing our dataset. To do this we use a likelihood function defined as

$$\mathcal{L}(\hat{\rho}) = \prod_j \mathrm{pr}_j^{f_j} \tag{2.51}$$

where $\mathrm{pr}_j = \langle j|\,\hat{\rho}\,|j\rangle = \mathrm{Tr}\left[\hat{\Pi}_j\hat{\rho}\right]$ is the probability of measuring $|j\rangle$ given $\hat{\rho}$. We immediately see that $\mathcal{L}$ if maximized when $\hat{\rho} = \hat{\rho}_0$, since the probabilities will

then exactly match the data ($\text{pr}_j = f_j$). In [49] Lvovsky presents an iterative method for maximizing this likelihood which is suitable for homodyne data. The approach is to introduce the operator

$$\hat{R}(\hat{\rho}) = \sum_j \frac{f_j}{\text{pr}_j} \hat{\Pi}_j \tag{2.52}$$

where $\hat{\Pi}_j = |j\rangle \langle j|$ is the projection operator. Noticing that as $\hat{\rho} \to \hat{\rho}_0$ we get $\text{pr}_j \to f_j$ which leads to $\hat{R}(\hat{\rho}) \to \hat{\mathbb{1}}$ since $\{|j\rangle\}$ is assumed to be a complete set so that $\sum_j \hat{\Pi}_j = \hat{\mathbb{1}}$. In the limit we then have $\hat{R}(\hat{\rho})\hat{\rho}\hat{R}(\hat{\rho}) = \hat{\rho}$, which forms the basis of an iterative process

$$\rho^{(k+1)} = \mathcal{N}\left[\hat{R}(\hat{\rho}^{(k)})\hat{\rho}^{(k)}\hat{R}(\hat{\rho}^{(k)})\right] \tag{2.53}$$

in which an initial $\hat{\rho}^{(0)}$ is asymptotically transformed towards the maximum-likelihood estimator $\hat{\rho}_0$ so that the likelihood monotonically increases. Each step of the iteration is normalized to unity trace by $\mathcal{N}$. We call this reconstruction approach the *MaxLik* algorithm, short for maximum likelihood.

2.5.1 Tomography from homodyne data

We now consider the special case that the data set $\{f_j\}$ is from a series of homodyne measurements of a single mode quantum state. We imagine our dataset as consisting of a total of N_f quadrature values, corresponding to the LO having been locked at different phase angles, while N_θ quadrature values where recorded at each angle. Since the eigenstates of the homodyne measurement, which are the quadratures states $|q_\theta\rangle$, are continuous valued, the set $\{|q_\theta\rangle\}$ has to be binned for the probability pr_θ to be finite. We therefore define the probability of observing the quadrature variable $\hat{q}_\theta$ within a bin spanning $]q_l; q_{l+1}[$ as

$$\text{pr}_{\theta,l} = \int_{q_l}^{q_{l+1}} \text{pr}_\theta(q) \, dq = \int_{q_l}^{q_{l+1}} \langle q_\theta| \hat{\rho} |q_\theta\rangle \, dq = \text{Tr}\left[\hat{\Pi}_{\theta,l}\hat{\rho}\right] \tag{2.54}$$

with $\hat{\Pi}_{\theta,l} = \int_{q_l}^{q_{l+1}} |q_\theta\rangle \langle q_\theta| \, dq$ being the projection operator for the lth bin at the phase θ. The integration is across the bin width dq. We then denote the number of observations in the lth bin as $N_{\theta,l}$ so that $N_\theta = \sum_j N_{\theta,l}$. As we are now using two indices θ and j to index our dataset $\{f_{\theta,j}\}$ we can modify eq. 2.52 to reflect it

$$\hat{R}(\hat{\rho}) = \sum_\theta \frac{N_\theta}{N_f} \sum_l \frac{f_{\theta,l}}{\text{pr}_{\theta,l}} \hat{\Pi}_{\theta,l} \tag{2.55}$$

Here $\sum_\theta$ is the sum over the LO angles and the factor N_θ/N_f ensures that the contribution to the sum from each angle is correctly weighted if N_θ is not equal

for all angles. We also note that the bins have to cover the entire range of quadrature values, so that we fulfil the completeness requirements of $\sum_l \mathrm{pr}_{\theta,l} = 1$ and $\sum_l \hat{\Pi}_{\theta,l} = \hat{\mathbb{1}}$, but as we will see in the section below, this is of course not feasible in a real world implementation of the algorithm. The derivation here only considered a single mode state, but it can readily be extended to multi-mode states, though the measurement data requires increases exponentialy with the number of modes the states occupies. Newer methods relying on neural Networks have therefore been developed for circumvent this difficulty [50]. Using the MakLik algorithm we reconstruct the density matrix, but to only observe Wigner negativity data obtain from photon-number-resolving measurements have been used to directly reconstruct the Wigner Function [51].

Loss compensated reconstruction

One of the advantages of this implementation of the MaxLik algorithm is the possibility of directly including and compensating for any detection inefficiencies in the reconstruction procedure. This is done by exchanging the projection operator $\hat{\Pi}_{\theta,l}$ with the POVM [52]

$$\hat{E}_{\theta,l} = \sum_{m,n,k} \sqrt{B_m^{m+k}(\eta) B_n^{n+k}(\eta)} \int_{q_l}^{q_{l+1}} \langle m|q_\theta \rangle \langle q_\theta|n \rangle \; dq \, |n+k\rangle \langle m+k| \quad (2.56)$$

which corresponds to measuring with a detector of η efficiency. The MaxLik algorithm will then directly reconstruct a state, where the loss from the detection have been compensated. For m and n the summation is from 0 to the eventual truncation of the photon number state space (explained below), and for k its from 0 to largest of m or n.
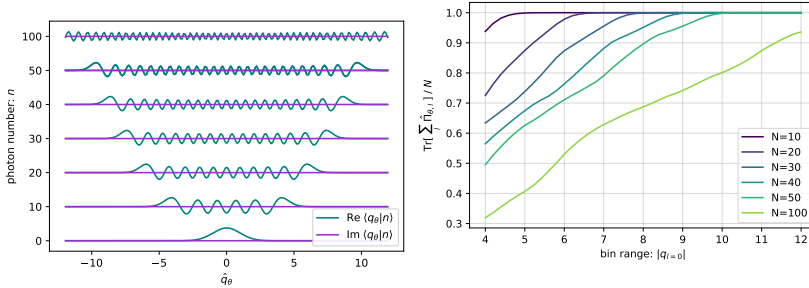
Uncertainty of MaxLik reconstruction

To estimate the uncertainty of the MaxLik reconstruction process we will use the bootstrap method. Here the density matrix reconstructed from experimental data is used to generate several sets of simulated data corresponding to having measured that reconstructed state with homodyne detection. Using the MaxLik algorthim on the simulated sets then provides a series of simulated density matrices. From these statistical uncertainties can be derived, such as the average distance to the original density matrix or the standard deviation of the resulting Wigner negativity.

2.5.2 Implementation of MaxLik

When implementing the MaxLik algorithm we choose to use the number state basis. In it we can directly use eq. 2.5 to calculate the matrix elements of the projection operator as

$$(\hat{\Pi}_{\theta,l})_{mn} = \int_{q_l}^{q_{l+1}} \langle m|q_\theta\rangle \langle q_\theta|n\rangle \ dq \tag{2.57}$$

But since the Hilbert space is infinite dimensional, we need to choose a highest photon number state N to include as the truncation point of our resulting N+1 dimensional space. This space of course has to be large enough so that the state $\hat{\rho}$ we are trying to reconstruct can be fully expressed, meaning that the largest photon number component of $\hat{\rho}$ should be much smaller than N. This truncation also influences how large a range of quadrature values our binning needs to cover in order for the completeness requirements to be met. Since we already assumed that N is the largest photon number component in our space, we need to choose the starting $q_{l=0}$ and ending $q_{l=N_b}$ point of our binning, such that $\int_{q_0}^{q_{N_b}} \langle q_\theta|N\rangle \ dq = 1 = \sum_{i,l} \text{Tr}\left[\hat{\Pi}_{\theta,l}\right]/N$, where q_0 and q_L is the This is is especially important to note for small amplitude quantum states such as PSSqV, since one could, from just observing the recorded quadrature values, make a choice of $q_{l=0}$ and $q_{l=N_b}$ large enough to not truncate $\{f_{\theta,l}\}$, but too small to not truncate the largest photon number component of $\hat{\Pi}_{\theta,l}$.

Figure 2.7: Wavefunctions $\langle q_\theta|n\rangle$ of photon number states used to calculate $\hat{\Pi}_{\theta,l}$

Figure 2.8: Overview of the bin range needed to satisfy $\text{Tr}\left[\hat{\Pi}_{\theta,l}\right]/N = 1$ for different truncation points N.

This issue is illustrated in fig. 2.7 and 2.8 and from them we see that a sensible choice could be $N = 30$ and $-q_0 = q_{N_b} = 10$, which is indeed what we will use for the simulated data and analysis of the experimental data presented in

chap. 4. Using the approach outlined below we also investigate the effect of the number of phase angles and the number of bins on reconstruction process. We use the fidelity and trace distance as metric and the results of this analysis is shown in sec. A.1. The conclusion is that using a azimuthal resolution of 30° and a bin range of 200, should suitable for a 1-PSSqV state.

Walkthrough of implementation

To see how to implement the MaxLik algorithm on experimental data collected by homodyne detection, we start by building a simulated dataset. With the expression for an odd cat state from tab. 2.1 we generate a $N = 30$ (31x31) density matrix of a state with mean photon number 2, rotate it 90° and subject it to 20% loss. We then generate simulated datasets of 20000 points by sampling from the inverted cumulative distribution at 30° phase intervals. From these datasets we build quadrature histograms by binning the data in the range -10 to 10 with 200 bins, giving a quadrature resolution of 0.1. Finally we combine all histograms into a single vector for convenience. By combining the data to a single vector the frequency reduces to a single subscript j and we avoid the sum over the phase angles.

These steps are shown in fig. 2.9. The MaxLik algorithm (eq. 2.53) is then run for 1000 iterations using eq. 2.52 and the identity matrix as $\rho^{(0)}$ and the result is shown in fig. 2.10. Here we see that already after 100 runs there is excellent agreement between the probability vector and the input data vector f_j. To check that the MaxLik algorithm really did construct our input state we use eq. 2.11 and 2.13 to calculate the fidelity and trace distance. Here we see that around 100 steps are needed for the direct reconstruction process to reach > 0.99 fidelity to the lossy input state, while the loss compensated reconstruction needs more than 10000 steps to reach > 0.99 fidelity to the pure state. We conclude the walktrough of our implementation of the MaxLik algorithm by inspecting the evolution of the state during the reconstruction process. We do this by looking at both the R operator, density matrix and corresponding Wigner function. This is shown in fig. 2.12 and 2.13.
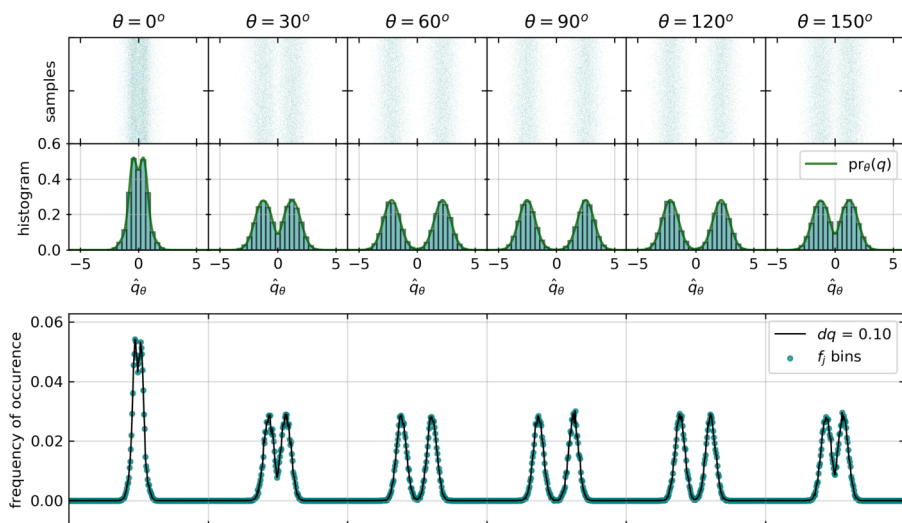
**Figure 2.9:** Preparation of simulated data for the MaxLik algorithm.
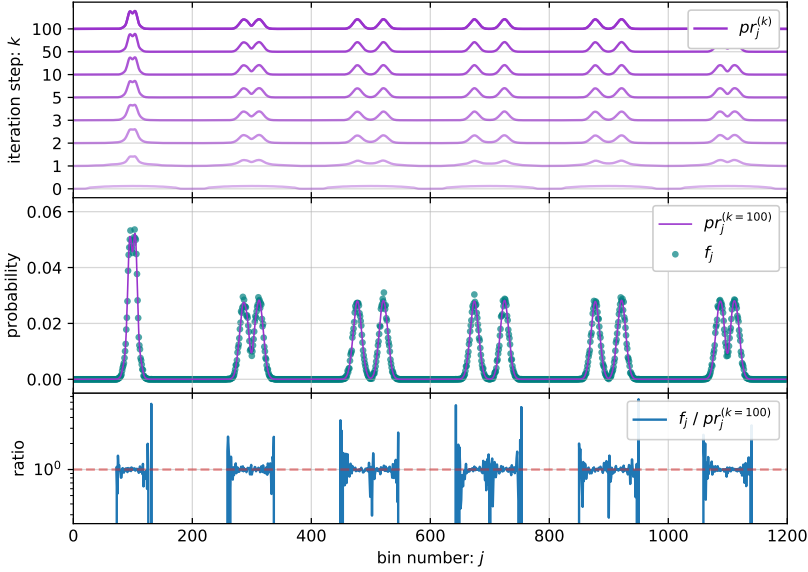
Figure 2.10: Result of running MaxLik on simulated data. (**top**) Evolution of the probability vector p_j during the MaxLik run. (**middle**) Agreement between the probability and frequency vectors. (**bottom**) Ratio between frequency and probability vector for 100 runs. The ratio should ideally be one for all bins, but is of course zero where the f_j bins were empty. At the transition to non-empty bins at the edges of the distributions we see that the ratio oscillates wildly. This is due numerical instability, as f_j is small and pr_j becomes close to 0.
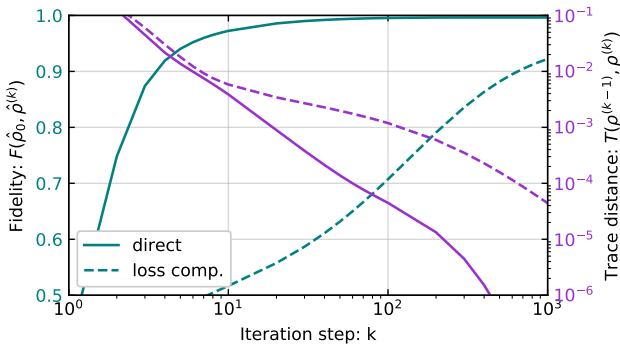
Figure 2.11: (**left axis**) Fidelity of the state to the input state during the direct and loss compensated ($\eta = 0.8$) reconstruction process. (**right axis**) Trace distance between steps during the reconstruction process.
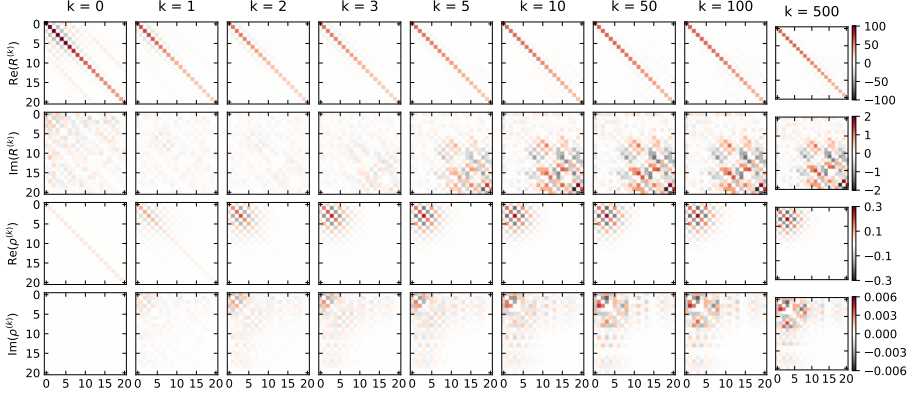
Figure 2.12: Evolution of the R operator and state density matrix during the reconstruction process. We see that initially all information about the state is contained in the R operator and that it is pushed towards the identity matrix as the density matrix is build up. We also note that the imaginary part of R outside of the photon number range supported by the density matrix is increased. This can most likely be attributed to numeral instability similar to what we saw in fig. 2.10(bottom), as there is little feedback from the MaxLik algorithm in the range of photon numbers beyond range supported by density matrix.
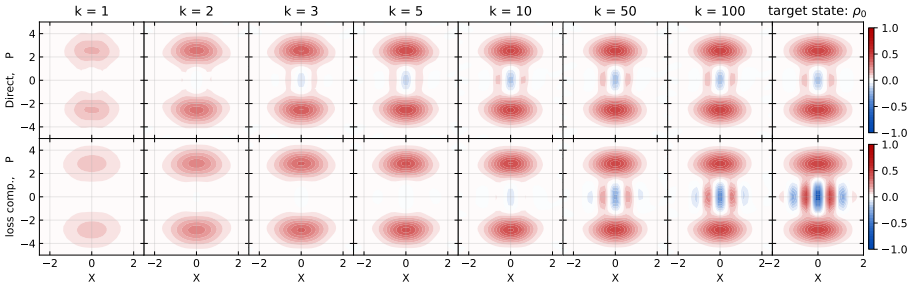
Figure 2.13: Evolution of the Wigner functions during the reconstruction process. Calculated using 2.10 on a 100x100 −10 to 10 x-p quadrature grid. Scaled is −π to π range.

Experimental Methods

A schematic overview of the experimental setup used for non-Gaussian state generation is shown in fig. 3.1. The key features of the setup will be be outlined below while a more in depth description of the three stages is given in the following sections. A detailed description of the setup used for the distributed sensing project can be found in the sec. A.5 of the appendix.

Coherent laser light at the fundamental frequency ω from a master laser source is split into a fundamental pump field α, to be frequency up-converted by a second-harmonic generation (SHG) cavity, and a local oscillator (LO) field α_{lo}, to function as a phase reference for homodyne measurement. The up-converted field β is then used to pump an optical parametric oscillator (OPO) cavity below its threshold with vacuum as its input, in order to generate a squeezed vacuum field by spontaneous parametric down-conversion. The squeezed vacuum field is then transmitted through a very weakly reflecting beamsplitter, in order to tap a small portion of the field into a *trigger channel*, while the rest of the squeezed vacuum field continues into a *signal channel*. In the trigger channel a filtering cavity (FC) system ensures that only the central frequency mode of the squeezed vacuum field is being transmitted to a single photon counting module (SPCM). In the signal channel the main part of the vacuum field is mixed with the strong LO field on a balanced beamsplitter for its quadrature values to be recorded by homodyne detection (HD). A single photon detection in the trigger channel then heralds that a photon was subtracted from the central frequency mode of

the squeezed vacuum field in the signal channel. Using the trigger signal the quadrature values of the photon-subtracted squeezed vacuum state is recorded by the HD and the non-Gaussian features of the state can be uncovered.
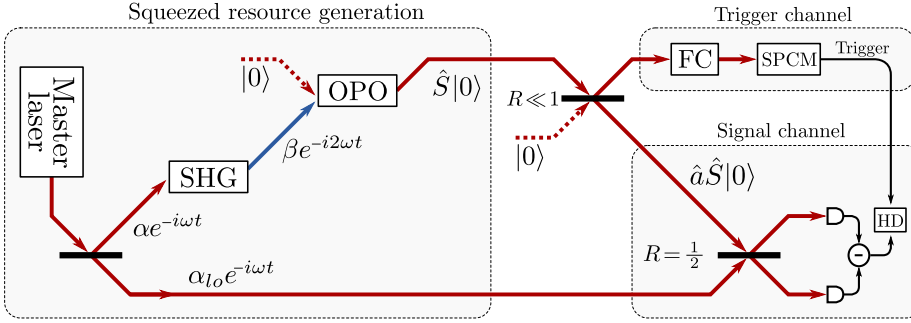
Figure 3.1: Simplified overview of the experimental setup.

3.1   Squeezed resource generation

For both the non-Gaussian state transmission and distributed sensing projects a squeezed vacuum field is used as the initial quantum resource. To generate the continuous squeezed vacuum field we design and build a free space optical setup. As mentioned in the chapter introduction the setup follows the conventional technique of generating squeezed vacuum from spontaneous parametric down-conversion in an OPO cavity pumped below threshold. The pump field is likewise generated by second-harmonic generation in a cavity from the same master laser field supplying the LO field, used for homodyne detection, to ensure good phase coherence. A schematic of the setup is shown in fig. 3.2

The setup can be divided into seven key features; [1] The master laser source, [2] fiber coupling of the local oscillator field, [3] beam chopping stage to implement a sample-hold measuring scheme, [4] fiber coupling of the filter cavity locking beam, [5] second harmonic generation cavity, [6] Optical parametric oscillator cavity, [7] splitting of OPO output into signal and idler beam and gain locking of the OPO.
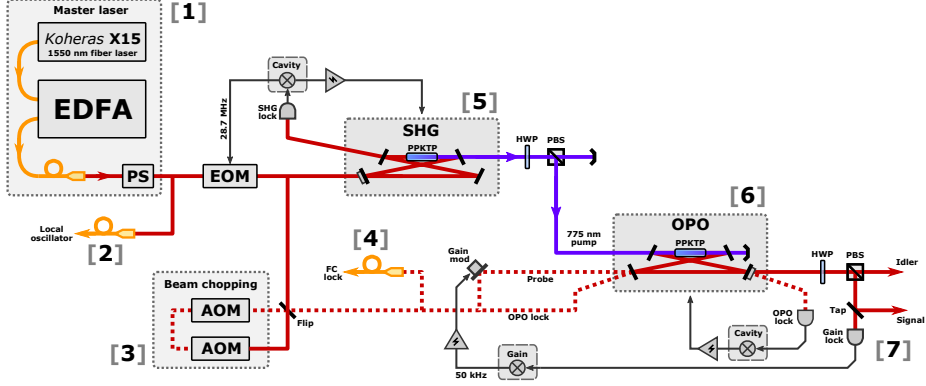
**Figure 3.2:** Schematic overview of the setup for squeezed vacuum generation.

## 3.1.1   Key features of non-Gaussian state generation setup

[1] Master laser

Since the motivation for our experiments are proof-of-principle implementations of quantum communication protocols for short distance networks we naturally want to work in the telecom band in order to utilize existing optical fibercomponents and infrastructure. We specifically chose to work at 1550 nm as this wavelength in general provides the lowest loss optical fibers and components. For our experiment we use a Erbium-doped fiber laser from NKT (`KOHERAS BASIK X15`) as the main laser. The X15 model has a linewidth of $< 0.1kHz$, typical phase noise below $-120dB/Rad/\sqrt{Hz}$ at 1 Hz and up and coherence length of 10s of kilometres. We then use an erbium-doped fiber amplifier (EDFA) from NKT to amplify the optical power from 40mW to a maximum of 2W. The laser light is guided by a single-mode fiber (SMF) and coupled out onto the optical table through a fiberport.

Unfortunately the output fiber of the EDFA is not polarization maintaining (PM) and we therefore observe some small drift of the polarization of the main laser output in range of a few Hz. This polarization drift in turn leads to drift of the optical power as we use polarization beamsplitters (PBS) to divide the beam to different parts of the setup. To mitigate this problem we use a simple polarization stabilizer (PS) consisting of a motorized half-wave plate (HWP), PBS, photo-detector, ADC and PID controller. A schematic overview of the PS can be seen in fig. 3.3. The HWP is set so that a small portion of the main beam is tapped off by the PBS and the optical power is monitored by the

detector. The resulting voltage signal is digitized and used as error signal for a digital PID controller connected to the driver of the motorized waveplate. The feedback loop of the PS then allows us to stabilize drifts in both optical power and polarization originating from the main laser source and to choose a locking point resulting in a desired optical power after the PS. For reliable operation of the PS it is important to choose the locking point so that the signal-to-noise ratio (SNR) of the error signal is sufficient.
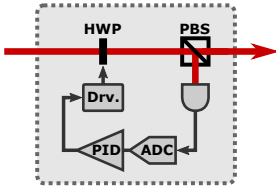
Figure 3.3: Polarization stabilizer (PS)
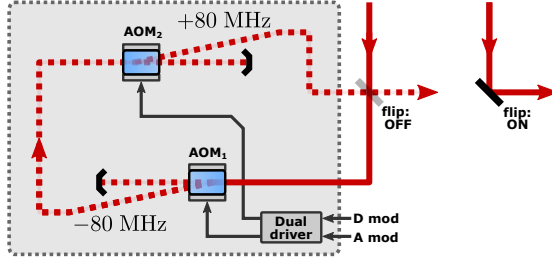
Figure 3.4: Beam chopper (BC)

[2] Local oscillator fiber coupling

Just after the PS part of the main laser field is tapped off using a half-wave plate (HWP) and polarization beamsplitter (PBS) combo. Since the beam is linearly polarized after the PS stage, turning the HWP tuned the power splitting of the PBS. The LO field is coupling to polarization maintaining (PM) single mode fiber (SMF) through a fiber collimator at 80% efficiency. A z-translation degree of freedom on the collimator can be used to adjust the coupling efficiency and thereby tune the LO power at the homodyne station. Detuning the coupling efficiency slightly also increases the stability of LO power, since it becomes less sensitive to mechanical drift. By fiber coupling the LO we also circumvent the need to use a mode matching cavity to clean the LO mode before interference with the signal for homodyne detection.

[3] Beam chopping

To avoid the strong beams used for phase control and cavity locking to couple through the trigger channel and into the SPCM and saturating it, we use a "sample-hold"-scheme when running the experiment. The scheme consists of continuously switching the control and probe beams on and off at a fixed

frequency and have been used extensively for heralded non-Gaussian state generation [53]. When the beams are on (*sample*) all phase and cavity locks are active and the experiment is being stabilized, when the beams are off (*hold*) all the feedback controls are kept constant, while the generated state is being measured. When using this scheme it is important to keep the hold period short enough so that drifts of phase and cavity locks are negligible and the sample period long enough to properly restabilize the experiment before holding it. Usually a longer sample period compared to the hold period is used. The specific settings used when running the experiment are listed in sec. 3.4.3.

In the setup we use a beam chopper (BC) consisting of two acousto-optic modulators to chop (turn on and off) the beam before it is split into a probe and lock beam (see fig. 3.4). An AOM operates by transcending an input electrical RF signal into standing sound waves across a transparent crystal, thereby deflecting part of an incoming light field due to the acousto-optic effect. Depending on the incident angle θ_{in}, the deflected part has its frequency either increased or decreased by the sound wave frequency, while the amplitude of the deflected part depends on the RF signal strength. The angle of deflection θ_{out} is related to the RF signal by $2\Lambda \sin \theta_{out} = m\lambda_0/n$, where Λ is the wavelength of the sound wave, λ_0 is the incident light wavelength, n is the refractive index of the crystal material and $m = 0, \pm 1, \pm 2, ...$ is the deflection order [54]. We use AOMs from ISOMET and drive them with a 80 MHz dual driver in an up-down configuration. In this configuration the beam is first up-shifted by 80 MHz (+1st order) with 60% efficiency and then down-shifted again with -80 MHz (-1st order) with 60% efficiency. The dual driver ensured that the total frequency shift is exactly cancelled. The driver has both an input for digital modulation (D mod), which turns the driver on and off, and analogue modulation (A mod), which tunes the strength of the modulation, and even when both inputs are zero, and there is no standing wave inside the AOM crystal, a small portion of the incident field will still scatter into the 1st order mode. Using both inputs in conjunction gives the highest possible extinction ratio, where we measure $\sim 120 \; dB$. Before the BC a flip mirror allows for the BC stage to be skipped if desired.

[4] Filter cavity lock beam fiber coupling

After the BC stage part of the beam is tapped off the be used as the locking beam for the FC in the trigger channel. The beam is again tapped using a HWP+PBS combo and coupled into SMF at 70% efficiency through a graded index (GRIN) lens. An electro-optic modulator (EOM) in the beam path before the BC stage is driven at 28.7 MHz by the SHG lockbox, to create a phase modulation used for Pound-Drever-Hall locking. This locking scheme is used for both SHG, OPO and FC cavities, since all their lockboxes are synchronized.

Further details regarding the locking schemes are given in sec. 3.4.2. The fiber coupling efficiency is not critical, since the FC only needs low power to lock and so any reflection will be minimal.

[5] SHG cavity

The frequency doubling of the fundamental 1550 nm light field into the second harmonic field at 775 nm is done by a nonlinear crystal placed at the waist of a tightly focused cavity mode, resonant to the fundamental field. The nonlinear conversion efficiency of the crystal is low (less than $1\%/W$) and so the cavity is used to enhance the input field to several watts of circulating power. As a result up to 60% total power conversion from the fundamental to the second harmonic field is realised. The cavity uses a compact bowtie configuration with the crystal waist between two curved mirror. The input field is coupled in through a 90% reflective mirror, while the rest are high-reflectivity (HR) to the fundamental field. All mirrors are transparent to the second harmonic field and so it simply coupled out through one of the curved mirrors. Details regarding the crystal and cavity design is given in sec. 3.1.2. The cavity is locked with the PDH locking scheme [55] using a PZT-actuator clamped to one of the flat cavity mirrors. An EOM in the input beam path creates a 28.7 MHz phase modulation, which is used to derive the error signal from a photodetector signal measuring a small part of the circulating light is leaking out through one of the high-reflector mirror. After the SHG cavity a HWP+PBS combo and a beamdump is used to control the power of the pump field coupled into the OPO cavity, thereby tuning the pump rate ϵ.

[6] OPO cavity

The parametric down-conversion of the OPO cavity is carried out by a nonlinear crystal identical to the one used for second-harmonic generation. Here the cavity is used to define the mode of the generated field and is designed identical to the SHG. The pump is coupled through the curved mirrors and dumped on the other side of the cavity. The generated fundamental field is leaked out through a 90% transmitting outcoupling mirror. The OPO is also locked using the PDH scheme and PZT-actuated mirror, with a locking beam coupling in through a HR mirror into the counter-propagating direction relative to the down-converted field. A photodetector with a 28.7 MHz resonant amplification circuit measures the locking beam coupling out through the outcoupler mirror. The OPO lockbox is synchronized to the SHG lockbox and so the same modulation is used. The crystal is AR coated and has a 1.15° degrees angled facet to ensure that the

locking beam does not couple to the co-propagating direction. A probe beam is also coupled into the OPO in the co-propagating direction to serve has a phase reference between the down-converted field and the local oscillator during homodyne measurement.

[7] Idler tapping and gain locking

Finally the output field of the OPO is divided into two channels, *signal* and *trigger*, by a HWP-PBS combination. We denote the beam in trigger channel as idler and the beam in signal channel as signal. Since the OPO output field is linearly polarized, turning the HWP effectively tunes the splitting ratio T between the two channels. Note that in our model we assumed the signal state to be the transmitted part, but in the experiment we use the reflection of the PBS as the signal part, since it has a higher extinction ratio, leading to cleaner polarization mode as compared to the transmitted part. From our model we know that the optimal choice of T depends on the dark count rate, but in the lab one also has to consider the overall stability of the setup when running the experiment and so even if a sufficiently low dark count rate would theoretically allow a very low tapping ratio, the time required to gather enough measurement statistics could become longer than the stability of some parts of the setup. As a starting point we choose to tap 3% corresponding to setting $T = 0.97$ in the model, since this value has been used in previous photon subtraction experiments [40].

When the probe beam is coupled into the OPO it will be either amplified or deamplified by the phase sensitive parametric interaction with the pump beam in the nonlinear crystal. The amount of amplification or de amplification relative to the no pump level is called the gain and is given by

$$G(\phi_p) = \frac{\cos^2 \phi_p}{(1-x)^2} + \frac{\sin^2 \phi_p}{(1+x)^2} \qquad (3.1)$$

where $x = \epsilon/\gamma = \sqrt{P_{in}/P_{thr}}$ is the pump parameter and P_{thr} the oscillating threshold of the OPO. This equation can be calculated from eq. 2.24 by exchanging $|\alpha_p|e^{i\phi_p}$ with the vacuum terms. The gain is then the fraction of the square of the steady state solution to the cavity field with and without the pump field. The phase between the pump and probe field is locked by tapping off 1% of the signal field and measuring it with a photodetector. By modulating the phase of the probe beam with a PZT-mirror, the relative phase between the probe and pump beam can be locked, using an AC locking scheme, to either amplification $\phi_p = 0$ or deamplification $\phi_p = \pi/2$. Consequently this locking angle sets the squeezing angle and so in our setup we lock to deamplification resulting in amplitude squeezing. See sec. 3.4.2 for more details regarding the locking scheme.

3.1.2   SHG and OPO design

Here we will present a short overview of the steps and considerations involved in designing the second-harmonic generation (SHG) and optical parametric oscillator (OPO) cavities used in the setup. Further details can be found in my master thesis [56]. In essence the design process is as follows:

1. Choose crystal material and design phase matching method to facilitate desired nonlinear process.

2. Based on crystal specifications design an optical cavity to enhance the nonlinear interaction.

For both steps an essential parameter to consider is the single-pass nonlinear conversion efficiency E_{nl}, which is a measure of the effectiveness of the power conversion between the fundamental and harmonic fields involved in the nonlinear process. For SHG we write $P_{2\omega} = E_{nl}P_\omega^2$ and so we would like our design choices during step (1) and (2) to maximize E_{nl}. In 1968, when studying the optimization of SHG and parametric generation (PG), Boyd and Kleinman arrived at a theoretical expression for E_{nl} in the experimentally relevant context of focused Gaussian beams [57]:

$$E_{nl} = \frac{16\pi^2 d_{eff}^2 l_{cry}}{\epsilon_0 c \lambda_\omega^3 n_\omega n_{2\omega}} e^{-\alpha' l_{cry}} h_{BK}(\sigma, \beta, \kappa, \xi, \mu) \tag{3.2}$$

where h_{BK}, called the BK-h factor, is the Boyd-Kleinman focussing function containing all the experimentally tunable parameters

$$h_{BK}(\sigma, \beta, \kappa, \xi, \mu) = \frac{e^{\mu\alpha' l_{cry}}}{4\xi} \int \int_{-\xi(1-\mu)}^{\xi(1-\mu)} \frac{e^{-\kappa(\tau+\tau')+i\sigma(\tau-\tau')-\beta^2(\tau-\tau')^2}}{(1+i\tau)(1-i\tau')} \, d\tau d\tau'$$

$$\tag{3.3}$$

An overview of the involved parameters can be found in tab. A.4. From the optimization of the BK-h factor (fig. 3.5) we obtain several key insights. If negligible absorption $\kappa = 0$ is assumed then the optimal focus position is in the middle of the crystal $\mu = 0$ and there then exists both an optimal focus strength ($\xi_m = l_{cry}/2z_R$) and optimal, non zero, phase mismatch ($\sigma = z_R\Delta k$), which are both determined solely by the crystal length. We therefore have the following two design constraints, which are independent of non-linear process or cavity geometry:

- The optimal focusing strength $\xi_m = 2.837$ determines the cavity design through the optimal Rayleigh length of the resonant cavity mode $z_{R,m} = l_{cry}/2\xi_m = l_{cry}/5.675$.

- The optimal phase mismatch $\sigma_m = 0.574$ determines the crystal design through the optimum wave vector mismatch $\Delta k_m = \sigma_m/z_{R_m} = 3.255/l_{cry}$.

Phase matching

The phase mismatch of non-linear process is defined as the wave vector mismatch $\Delta k = k_{in} - k_{out}$ of the fields inside the crystal. For SHG and SPDC the fields are $\Delta k_{SHG} = 2k_\omega - k_{2\omega}$ and $\Delta k_{SPDC} = k_{2\omega} - 2k_\omega$ respectively, so that $\Delta k_{SHG} = -\Delta k_{SPDC} = \frac{4\pi}{\lambda_\omega}(n_\omega - n_{2\omega})$. This means that we will be able to use the same crystal for both SHG and SPDC. For plane waves this mismatch should be zero to fully utilize the crystal length, since a non zero mismatch will eventually lead to the accumulated phase difference between the two fields exceeding π thereby causing the process to reverse and power to be transferred back to the pump field. This exact length is called the coherence length $l_{coh} = \pi/\Delta k$. But from the Boyd-Kleinman theory we know the optimal wave vector mismatch Δk_m for focused Gaussian beams.
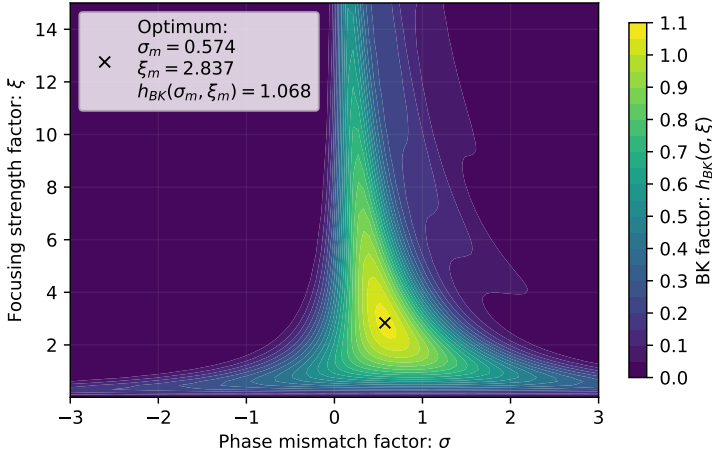
Figure 3.5: The σ- and ξ-dependence of the BK-h factor under the assumption that $\beta = \kappa = \mu = 0$, so that eqn. 3.3 reduces to a single, real-valued, integral: $h_{BK}(\sigma, \xi) = \frac{1}{4\xi} \left[\int_{-\xi}^{\xi} \frac{\cos \sigma\tau + \tau \sin \sigma\tau}{1+\tau^2} \, d\tau \right]^2$ [58]

For crystal material we choose periodically poled potassium titanyl phosphate (PPKTP) from `Raicol Crystals`, as their crystals had previously shown good performance for both SHG of 775 nm pump light and SPDC into 1550 nm squeezed light [59–61]. Here periodically poling is a method of obtaining quasi-

phase matching (QPM) by having the nonlinearity of the crystal periodically change sign, so that a phase grating of period Λ_{pol} is formed, effectively imposing an additional momentum of $G = -2\pi/\Lambda_{pol}$ to the phase matching condition. In practice the alternating nonlinearity is achieved by periodically poling the crystal with a strong electric field along its length, forming domains of length $\Lambda_{pol}/2$ with every other domain flipped. By carefully engineering the poling period Λ_{pol} it should then be possible to fulfil the QPM condition $\Delta k_m = \Delta k + G$.

A downside of using QPM is that the effective nonlinearity d_{eff} is scaled by a factor $2/\pi$, while the upside is that periodically poling works for any crystal direction, so that one with the largest nonlinearity d_0 can be utilized. The principle of using periodically poling to obtan QPM is best illustrated for plane waves, where the optimal phase mismatch is 0 resulting in the mth order QPM condition $\Lambda_{pol} = 2m\pi/\Delta k = ml_{coh}, \ m \in 1, 3, 5, ...$ Here the poling period should be an odd integer number of coherence lengths. This effect is illustrated in fig. 3.6.

In general both the dispersion and birefringence of the crystal will be temperature dependent, and so we need to know the exact temperature dependence of refractive index to calculate the phase mismatch accurately. From the litterature we use the formula obtained by Emanueli and Arie [62] for the temperature dependence and the base indexes obtained by Fradkin *et al.* [63], Kato *et al.* [64] and Fan *et al.* [65]. Further details and an overview of all involved parameters can be found my thesis [56]. We plot the phase mismatch as a function of crystal temperature and poling period to see if we can reach the optimal mismatch with reasonable values. The results are shown in fig. 3.7. From fig. 3.7 we see that we should be able to obtain optimal phase matching for a range of poling periods and temperatures. In the end we choose to use a 16 mm crystal, where Raicol recommends a poling period of ~ 24.7 μm and operating temperature of $\sim 30 - 50$ ^{o}C, which appears to match well with the parameters suggested by using the Fradkin numbers. We also note that even if the poling period is slightly off, we have some leeway in the temperature to reach the optimal mismatch. The parameters suggested by using the Kato and Fan numbers are quite far off from the recommended parameters, so we choose to disregard them. We conclude our crystal analysis by investigating the dependence of the BK-h factor on different parameters of the model 3.3. The results of this analysis is shown in fig. 3.8.

Cavity geometry

From the optimization of the BK-h factor for our choice of crystal length ($l_{cry} = 16mm$), we know that we should design our SHG and OPO cavities
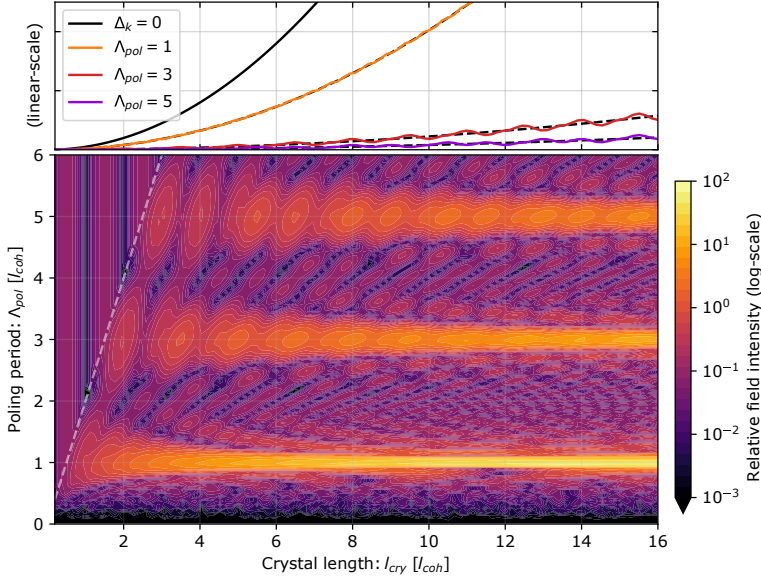
Figure 3.6: Illustration of the effect of using periodically poling to obtain quasi phase matching for planar waves. Calculated using $E_{2\omega} \propto \int_0^{l_{cry}} d(z) e^{i\Delta k z} dz$, where $d(z)$ is a $\pm d_0$ step function along the crystal length with Λ_{pol} as period, emulating the periodically poled nonlinearity d_0. We see that the field is only effectively build up, when the QPM condition of $\Lambda_{pol} = m l_{coh}$, $m \in 1, 3, 5, ...$ is satisfied. The upper line plot shows the linear scaling of the quasi phase matched field build-up for comparison, together with the corresponding perfectly phase matched field build-up using the effective nonlinearity $d_{eff} = (2/m\pi) d_0$. The overlap of the curves shows that using the effective nonlinearity for perfect phase matching correctly captures the effect of mth-order QPM.

such that the resonant mode has a waist size inside the middle of the crystal of $\omega_{0,m} = \sqrt{\lambda_0 z_{R,m}/\pi n(\lambda, T_m)} = \sqrt{\lambda_0 16 \text{ mm}/(\pi 1.82 \times 5.675)} = 27.7 \ \mu m$. Of the three main cavity geometries (linear, triangle, bowtie) we choose the bowtie, as this geometry design has several key advantages for our purpose. Besides being practically easy to design, build and work with due to the several degrees of freedom, the main advantage is, from the perspective of OPO, that it supports a running wave resonant mode, meaning that the two directions of propagation inside the cavity does not interfere, and the output coupler mirror will be angled relative to the output signal beam path. This means that we can use a counter propagation lock beam relative to the signal beam and that any back reflection from signal path, such as FC lock or LO light, into the OPO will not interfere with the signal field. This both helps to reduce the contamination of the
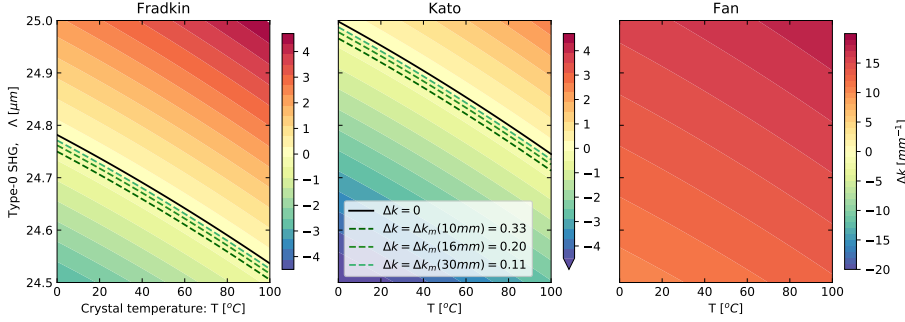
Figure 3.7: Phase mismatch of type-0 SHG for three different PP-KTP crystal lengths calculated using refractive index values from literature. $\Delta_k = \Delta k_{\text{SPDC-0}}^{(\omega)}(T) + G$ with $\Delta k_{\text{SHG-0}}^{(2\omega)}(T) = \frac{4\pi}{\lambda_\omega} \left| n_z(\frac{\lambda_\omega}{2}, T) - n_z(\lambda_\omega, T) \right| = \Delta k_{\text{SPDC-0}}^{(\omega)}(T)$ and $G = -2\pi/\Lambda_{pol}$

squeezed light field in the signal path and to reduce the possibility of light being scattered into the idler path and coupling to the SSPD. The facet of the crystal is, for the same reason, cut at an angle of 1.15^o. Further details regarding the mechanical design can be found in my master thesis [56].

Using the cavity design approach as outline in sec. A.2.2 of the appendix with the bowtie geometry definition of tab. A.3, with crystal length $l_{cry} = 16mm$, crystal refractive index $n = 1.82$, mirror curvature $R = 50mm$, cavity round-trip length $l_{cav} = 310mm$ and folding angle $\theta = 6^o$, we obtain the resonant solution shown in fig. **??**. Here fixing l_{cav} and θ lets us vary l_1 as the only free parameter. We see that with a distance of 58 mm between the curve mirrors, the resonant mode will have the optimal waist size inside the crystal and that the low folding angle ensures very low astigmatisme of the mode. The finesse $F = \pi\sqrt{r}/(1 - r)$ of the cavity is a similar measure of how well the cavity stores the resonating light field and is related to the full-width at half-maximum (FWHM) bandwidth as $2\gamma \approx \Delta_\omega/F$. The parameters of our cavity is summarised in tab. 3.1.

3.1.3 SHG performance

For the performance of the SHG cavity the metric we consider is the total conversion efficiency of the fundamental field into the second harmonic field, which will be determined by the nonlinear conversion efficiency E_{nl}. The input-output power conversion is easily measured experimentally, but in order to relate the result into the corresponding nonlinear conversion efficiency we need to
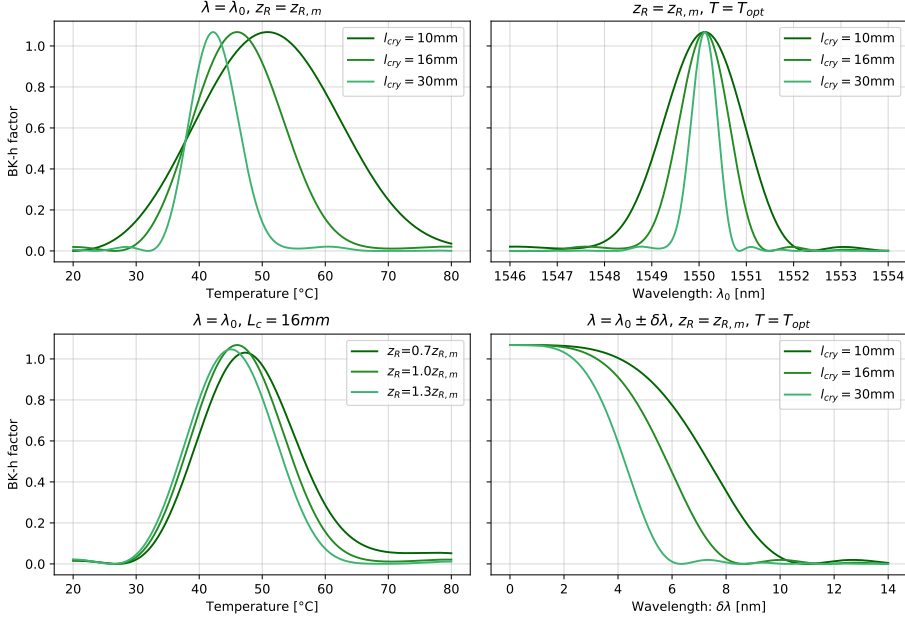
Figure 3.8: Dependence of the BK-h factor (eq. 3.3) on different model parameters. The temperature dependence comes from the refractive index (fig. 3.7). (**top-left**) Temperature has to be controlled to at least within 1 ^{o}C to maintain a stable nonlinear conversion. (**bottom-left**) Even a $\pm30\%$ deviation from the optimal focus, will not result in drastic reduction of the BK-h factor. (**top-right**) We are not concerned with the overall wavelength dependence of the fundamental field since our fiber laser is stable. (**bottom-right**) Phase matching bandwidth of the down-conversion process. This will be important when we design the frequency filtering of the trigger channel needed to suppress all the frequency sideband modes of the OPO output.

consider how the intra-cavity field is related to the input power. We start with the simple expression for the relationships between the input, intra-cavity and reflected fields [66]

$$\frac{P_{cav}}{P_{in}} = \frac{T_1}{(1-r)^2} \qquad \frac{P_{refl}}{P_{in}} = \frac{1-(T_1-r)^2}{(1-T_1)(1-r)^2} \tag{3.4}$$

Here T_1 is the input coupler transmission, which is 0.1 for our SHG and $r = \sqrt{1-T_1}\sqrt{1-\mathcal{L}}\sqrt{1-E'_{nl}P_c^{(\omega)}}$ is the total round-trip field amplitude attenuation caused by the combination of outcoupling, linear loss $\mathcal{L}$ and nonlinear loss due to the frequency conversion, where E'_{nl} is the nonlinear conversion efficiency without accounting for the absorption of second harmonic field in the

|		
Crystal	Length, l_{cry}	16 mm
	Height x width	2 mm x 1 mm
	Poling period, Λ_{pp}	27.7 μm
	Operating temperature, T_m	$\sim 45\ ^o$C
Geometry	Crystal waist	27.7 μm
	Cavity length, l_{cav}	310 mm
	Mirror curvatures, R	50 mm
	Folding angle, θ_{cav}	6°
Spectral	Outcoupler, T_1	10%
	FSR, $\Delta\omega$	967 MHz
	Bandwidth, γ	8 MHz
	Finesse	~ 60
	Escape efficiency, η_{esc}	0.98

Table 3.1: Design specifications of the SHG and OPO cavities

crystal ($\alpha' = 0$ in the model). This correction is needed since the amount of lost fundamental field, relevant in the context of intra-cavity field attenuation, is independent on loss of the harmonic field due to absorption. The absorption of the fundamental field can then be included in the linear loss term for convenience. The full nonlinear conversion efficiency is then calculated using $P_{out}^{(2\omega)} = E_{nl}(P_c^{(\omega)})^2$ with $P_c^{(\omega)}$ obtained numerically from eq. 3.4. The result is shown in fig. 3.9.

3.1.4   OPO performance

From a classical perspective the OPO performance can be benchmarked by the observed parametric gain. The measurement is straight forward; a probe is coupled to the OPO and the gain at various pump powers is recorded. From this measurement the threshold of the OPO can be determined, which is an important parameter since it tells us what pump power to inject for a desired pump rate ϵ. The results of such a measurement is shown in fig. 3.10. The threshold is related to the nonlinear conversion efficiency by $P_{thr} = (T + \mathcal{L})^2/4E_{nl}$ [67] and for the OPO we measure an escape efficiency of $\eta_{esc} = 0.97$ corresponding to an intra-cavity loss of $\mathcal{L} \approx 0.3\%$. With a measured threshold of 788 mW this should correspond to a nonlinear conversion efficiency of approximately $0.34\%/W$, which is seen to agree reasonable well with our result from the SHG performance test.

From a quantum perspective the OPO performance is benchmarked by the amount of squeezing produced, though this in reality is a benchmark of the com-
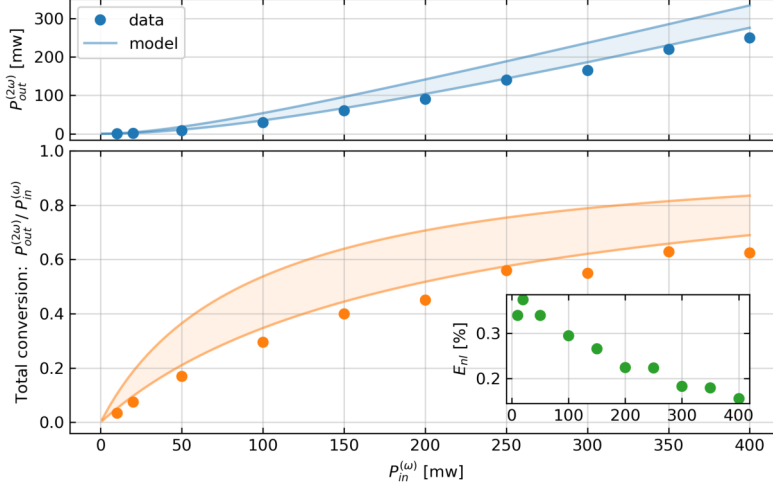
Figure 3.9: Plot of the measured performance of the SHG cavity. We observe a maximum total conversion of 0.63 at 350 mW, but with a resulting low conversion efficiency of 0.18%. The obtained nonlinear conversion efficiency ranges between 0.16%/W and 0.38%/W as seen from the insert. These values are lower than the 0.7%/W expected by Raicol and can be attributed to a combination of misalignment of the cavity field and irregularities in the poling period long the crystal. The model is calculated using eq. 3.2 with d_{eff} as the lowest and highest value reported in literature and the linear loss estimated by measuring the depth of the cavity resonance dip in reflection, when the crystal temperature is tuned outside the interaction bandwidth.

bined performance of the OPO, signal channel and homodyne detector. Since we plan to run our experiment using the sample-hold scheme we are interested in investigating the stability of our setup. It should of course be so stable, so that no difference in the measured squeezing level is seen during the hold period. To see this we record a sequence of 1000 individual time traces of the OPO output locked to both squeezing and antisqueezing. We divide the long traces into several shorter segments and compute the variance and power spectrum of the noise relative to noise of corresponding shot noise segments. The results of this analysis are shown in fig. 3.11.

We observe a maximum squeezing level of close to -5 dB at $1-2MHz$ relative to the vacuum level with a corresponding anti squeezing level at $7.5-8.5$ dB. The reduction in squeezing and antisqueezing at low frequencies can be con-
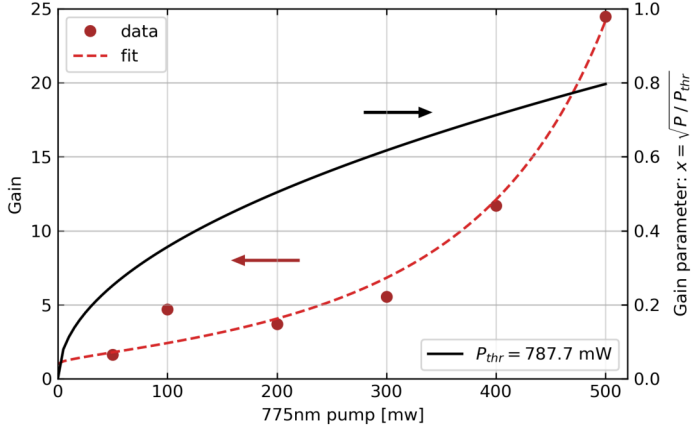
Figure 3.10: Plot of the measured gain at different pump powers. Fit of eq. 3.1 gives a threshold power of $P_{thr} = 788 \pm 1$ mW. The right axis shows the scaling of the corresponding pump parameter $x = \sqrt{P/P_{thr}}$

tributed to phase noise of the local oscillator lock, which affects the squeezing level more severely than the antisqueezing as seen be the identical squeezing at 1 and 2 MHz. During the measurement the coupling efficiency of the signal into SMF was 89%, while the other measurement parameters were estimated to be 0.53 pump rate, total homodyne efficiency 0.90, escape efficiency 0.97, gain lock tapping 0.99 which gives a total efficiency of 77%. Taking the phase noise into account the best fit to the power spectrum are obtained using $\gamma = 2\pi \times 6.9$ MHz, $x = 0.53$, $\eta = 0.78$ and $\phi_{ac} = 9^o$ phase noise during the squeezing measurement. Though the bandwidth appears to be somewhat smaller than expected by the OPO design, we often get get a lower bandwidth when fitting using a phase noise term, since they affect the shape of the squeezing trace in a similar fashion and with the large phase noise used by the fitting routine the uncertainty is large. Our two main take away conclusions is that the squeezing level seems to stay constant during the hold time and that our measurement suffers from large phase noise of the LO lock at frequencies below 2 MHz, which will have to be improved.

The setup for squeezing light generation also contains an additional identical OPO (not shown here), and has been used for the deterministic generation of a 2-dimensional cluster state [68] and later the deterministic implementation of a multi-mode gate set on it [69].
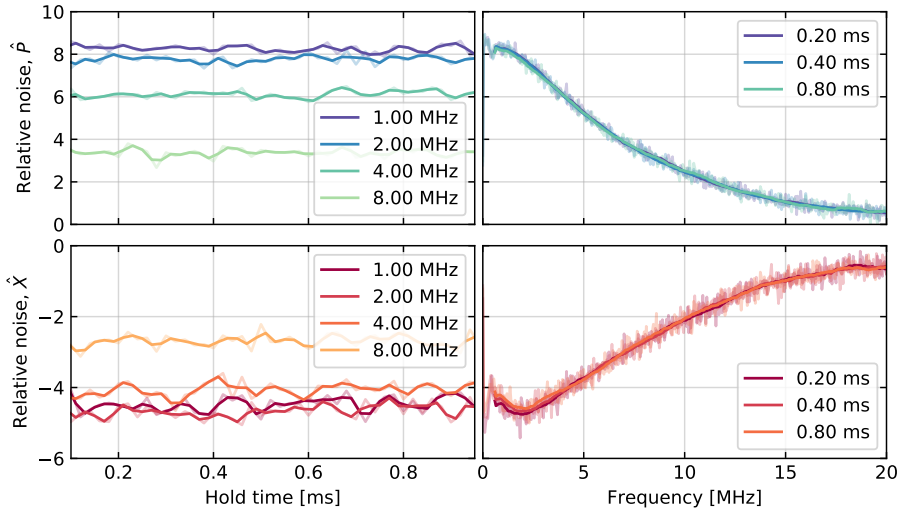
Figure 3.11: Typical squeezing levels using fiber coupled homodyne detector and sample-hold measurement scheme.

3.2   Trigger channel

As we know from our model and plan of the experimental layout the job of the trigger channel is to filter away all the undesired longitudinal modes of the OPO, so that only photons subtracted from the central frequency mode are coupled to the single photon detection module (SPDM) for heralding. A conceptual schematic of the trigger channel is shown in fig.3.12. Here a linear filtering cavity (FC) and a dense wavelength division multiplexing (DWDM) filter work in combination to provide the frequency filtering necessary for suppression of the higher and lower order longitudinal OPO modes, while a superconducting single photon detector plus amplifier electronics work as the SPCM, converting the subtracted photons into electrical trigger signals for heralding. After the FC a free space AOM is used to protect the SSPD from saturation when running the experiment with the sample-hold scheme, by blocking the strong idler beam during the sample period. The refracted part of the idler beam, containing only single photons from the central frequency mode of the OPO, is coupled into SMF through a gradient-index (GRIN) lens and after passing the DWDM filter leaves the optical table and is guided through 10 m of fiber into the SSPD in an adjacent technical room. Here the inherent broadband detection of the SSPD makes the +80 MHz frequency shift of the refracted beam by the AOM irrelevant.

The FC locking beam is turned to an orthogonal linear polarization, as compared to the idler beam, and coupled into the FC from the backside using a PBS, while a second PBS on the front side couples the locking beam out again and into a locking detector. The FC is locked using the PDH scheme (see sec. **??** for details). An isolator (ISO) ensures that neither probe light reflected on the FC or light from the FC locking beam couples back into the OPO.
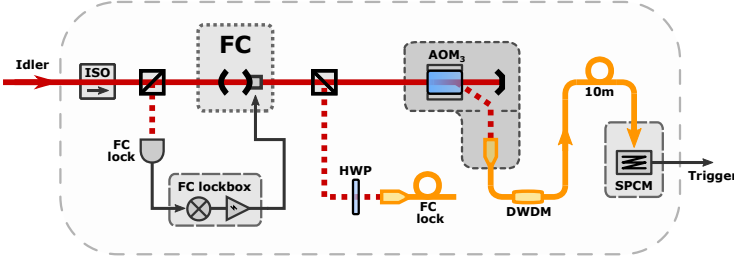

Figure 3.12: Schematic overview of trigger channel

3.2.1   Frequency filtering

From fig. 3.8(bottom-right) we expect the bandwidth of the SPDC process for a 16 mm crystal to be $5 - 6$ nm corresponding to $622 - 746$ GHz and with a designed OPO FSR of around 1 GHz it is clear that many hundreds of OPO modes will be available for the SPDC process to populate. Though in reality the number of available modes will be smaller since both the upper and lower mode pair will have to be simultaneously resonant within the cavity. The exact number of available modes can in principle be calculated by considering that the dispersion of the crystal will cause the relative resonance frequencies the upper and lower modes to be detuned. As a result, when the detuning becomes larger than the OPO bandwidth, the SPDC process will be suppressed, due to the energy conservation requiring equal spacing of the modes from the fundamental frequency. But as we shall see from the use of the DWDM filter, we need not take this effect into account.

From our model we know that the bandwidth of our trigger filter should ideally be several times larger than the OPO bandwidth, but it should of course not be comparable to the FSR of the OPO. In reality it is quite difficult to construct a single frequency filter which has both a narrow bandwidth and a very large if not infinite FSR. To this end we choose to employ two filters; firstly a narrow (2.2 mm) linear filter cavity with a bandwidth of $\gamma_{FC} \approx 24\ 2\pi$MHz and FSR of $\Delta\omega_{FC} \approx 75\ 2\pi$GHz, secondly we take advantage of the SSPD being fiber coupled and use a standard 50 GHz DWDM C-band filter centred at 1550 nm as a

passive bandpass filter. An overview of the two filter spectra relative the OPO and full SPDC is presented in fig. 3.13, where it is clear from the lower plot that the bandpass spectrum of the DWDM allows us to disregard the reduced SPDC spectrum as discussed above.
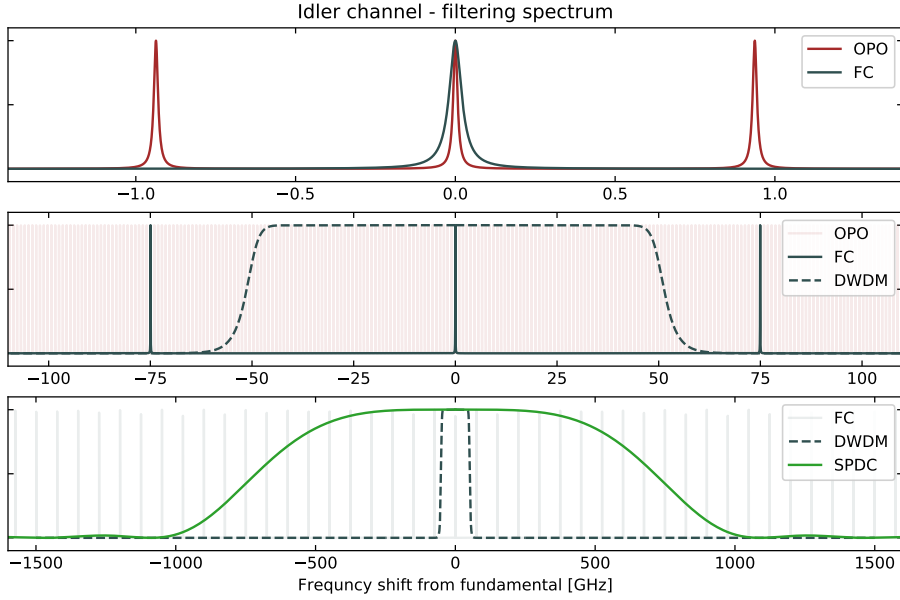
Figure 3.13: Overview of the combined filtering of the filter cavity (FC) and dense wavelength division multiplexing (DWDM) bandpass filter. OPO bandwith is $\gamma_{OPO} \approx 8$ 2πMHz with FSR $\Delta\omega_{OPO} \approx 1$ 2πGHz, FC bandwith is $\gamma_{FC} \approx 24$ 2πMHz with FSR $\Delta\omega_{FC} \approx 75$ 2πGHz, DWDM bandwith is $\gamma \approx 50$ 2πGHz and the full SPDC bandwidth is $\Delta\omega_{SPDC} \approx 685$ 2πGHz.

We measure a typical transmission efficiency of the FC of $\sim 80\%$ followed by a typical efficiency of the remaining channel (AOM, fiber coupling, DWDM) measured at the fiber output before the SSPD of $\sim 40\%$. We therefore estimate the total optical transmission efficiency of the trigger channel to be $\sim 30\%$. Together with an estimated SSPD efficiency of 60% the total trigger channel efficiency is then $\eta_t \approx 20\%$. More effort could be made to increase this efficiency, but from our model, with the low dark counts we are able to achieve, we expect negligible improvements.

Filter cavity geometry

The filter cavity is build around a Thorlabs cage system and uses two identical 500 mm curved 1/4"-inch mirrors with $T = 0.2\%$ transmission coatings. One mirror is mounted together with a ring PZT-actuator in a specially designed holder. The mirror sits in a small aluminium socket that is clamped to the PZT-actuator by a preload mechanism. The aluminium socket allows the mirror to sit extended forward, so that the cavity distance in principle can be made arbitrarily short. For our measurements we set it to 2.2 mm and the cavity finesse is ~ 1600. The holder is mounted in a typical tip-tilt stage, while the second mirror is kept fixed without any degrees of freedom. The waist size is calculated using the cavity design guide outlined in sec. A.2.2 of the appendix and a plot of the design consideration is seen in fig. A.6. Further details regarding the cavity design can be found in my thesis [56].

## 3.2.2   Superconducting single photon detector

To detect the photons subtracted from the squeezed vacuum signal, we employ a fiber-coupled superconducting single photon detector (SSPD) based on a nio-bium titanium nitride (NbTiN) nanowire cavity stack developed at the National Institute of Information and Communications Technology in Kobe, Japan [70]. The stack consists of a few nm thick meandering NbTiN nanowire sandwiched between a layer of SiO, with a ~ 100 nm thick Ag mirror on top, and a layer of SiO_2 towards the Si substrate, forming a doubled sided cavity around the nanowire to increase the absorption probability [71]. The filling factor of the nanowire have been optimized for high system detection efficiency (SDE) and high counting rate simultaneously for 1550 nm [72]. The reported specifications of the sensor are a SDE of $\sim 70\%$, with a maximum timing jitter of 68 ps and dark count rate of 100 Hz. The sensor package is housed in a Gifford-McMahon (GM) cryocooler [73], which is pumped to a vacuum pressure of $\sim 5 \times 10^{-5}$ Pa and cooled to ~ 2 K by a helium compressor.

An overview the SSPD and readout electronics is shown in fig. 3.14. A Battery powered voltage source supplies a steady bias current to the SSPD nanowire through the dc arm of a bias tee. The nanowire is cooled below its critical temperature and the the voltage is set so that the bias current is just below the critical current. An absorption of a photon will then create a small resistive hotspot at the absorption location, causing the current density to rapidly in-crease in the vicinity of the hotspot end eventually exceeding the critical density. This causes a resistive barrier to form across the nanowire and, aided by joule heating from the bias current, eventually blocking the current flow. The drop

in current is readout as a voltage pulse through the AC arm of the bias tee and amplified by a low noise amplifier. Even after the amplifier the voltage pulse is quite small and short and we therefore use a discriminator to convert the pulse to a signal more suitable signal for triggering an oscilloscope. The shape of the pulses after the amplifier and discriminator can be seen in fig. 3.15.
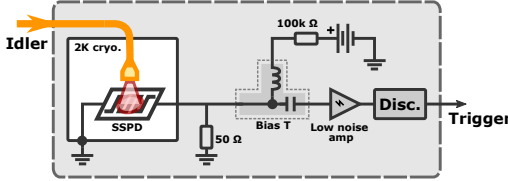
Figure 3.14: Single photon counting module (SPCM) consisting of a superconducting single photon detector (SSPD) and readout electronics
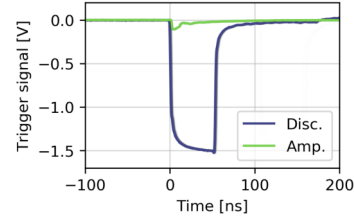
Figure 3.15: Electrical trigger signal after low noise amplifier (Amp.) and discriminator (Disc.). Overlay of 200 traces is shown.

For every input pulse the discriminator can output a pulse on two different channels at the same time and so we use one channel as the trigger for an oscilloscope during data collection and the other we connect to a 8-channel Counter/Timer Device (PCI 6602 form National Instruments) installed on a lab computer. From a homemade LabView program we then monitor the count rate and collect count statistics when running an experiment. The program is especially useful since we also input the hold signal and program one counter to use it as a gate, thus allowing us to monitor both the total count rate and the equivalent hold period count rate. It is this count rate we use to estimate the modal purity.

During the measurements for the cat state transmission projected presented in cha. 4 we observed typical SDEs of $\sim 60\%$ and could maintain count rates of up to a few million Hz before latching with dark count rates between 10 and 50 Hz. Here *dark count rate*, $\langle \Delta n_{dc}^2 \rangle$, is considered to be the observed count rate when the SSPD fiber is disconnected from the trigger channel, not to be confused with the *fake count rate*, $\langle \Delta n_{fake}^2 \rangle$, which we consider as the observed count rate when running the experiment and blocking the OPO pump beam. Both rates are counted during the hold period, as mentioned above. This rate therefore includes the dark count rate and the counts originating from all other sources than subtracted signal photons. As we use LED lights in the laboratory very little ambient light couples to the SSPD and the fake count rate is therefore mainly caused by scattered light probe and lock light. To minimize the fake counts we installed several sections of blackout hardboard to wall off the parts of the setup containing the strongest beams, as well as encapsulating the SSPD

fiber coupling setup.

3.3   Signal channel

As motivated in the introduction the aim of the *non-Gaussian* project is to successfully transmit a CV non-Gaussian quantum state between two physically distant locations. A successful transmission is benchmarked by the survival of non-Gaussianity through the verification of a measurable Wigner negativity at the receiver side. The desired setup for the signal channel is therefore quite straight forward: after a small part of the beam is tapped off for the trigger channel the signal beam is coupled into SMF through an anti reflective (AR) coated graded index (GRIN) lens. The non-Gaussian signal state is then transmitted through a fiber channel, to the receiver location where it is characterized by quantum tomography. The tomography is performed on quadrature statistics collected by measuring the state with homodyne detection at various locked local oscillator (LO) angles. To perform the state characterization at the receiver location a portable fiber coupled homodyne measurement station (HMS) with all the necessary components for locking, triggering and data collection is used. The only signals needed to be transmitted between the sender (lab A) and receiver location are then the signal state, LO and trigger signals. An overview the signal channel is shown in fig. 3.16 and a description of the three different configurations used for fiber network channel is given in sec. 3.3.2.

To transmit the electrical SSPD trigger signals a electrical-to-fiberoptic ($E \rightarrow O$) converter from Highland Technology is used to convert the signals to 1310 nm optical TTL pulses, which are then combined with the LO on a 1310/1550 wavelength division multiplexer (WDM) and coupled into a separate SMF channel adjacent to the signal channel. On the HMS an identical WDM and corresponding fiberoptic-to-electrical ($O \rightarrow E$) converter first splits the LO and trigger signals and then converts the trigger pulses back to electrical TTL signals. The $E \rightarrow O$ conversion happens with a < 250 ps risetime, < 12 ps typical RMS link jitter and total propagation delay of 1.2 ns, while the $O \rightarrow E$ happens with a < 750 ps risetime, < 12 ps typical RMS link jitter and total propagation delay of < 10 ns. The low jitter time is especially important to ensure that the photon subtracted part of the homodyne photocurrent arrives at the digital sampling oscilloscope (DSO) a fixed delay relative to the arrival of a SSPD trigger click. If the trigger delay varies, the photon subtracted part will not appear at the exact same point in time of the recorded time traces. As a result the temporal mode function can not be placed correctly for all time traces, leading to additional background squeezed vacuum being included ultimately reducing the observable Wigner negativity.
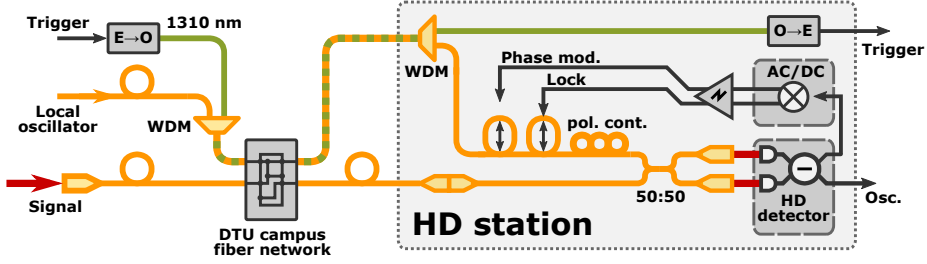
**Figure 3.16:** Schematic overview of the signal channel

3.3.1   Homodyne measurement station

The HMS relies on a SMF fiber based homodyne measurement setup. Here both signal and LO beams are SMF coupled and interfered on a fiber 50:50 beam-splitter (BS) before directly outcoupling onto the homodyne detector diodes through GRIN lenses. The main advantage of the fiber setup is that almost perfect mode overlap between the signal and LO is inherently guaranteed by the fiber BS and with carefully taped SMF fibers the polarization is well maintained leading to close to unity homodyne visibility being achievable using manual polarization controller. In order to scan the phase of the LO we use a homemade *fiber stretcher*, which is based on a 3D printed, Pacman like, structure with a PZT-actuator stack placed in the mouth of the Pacman and the fiber tightly wound around the circumference (see fig. A.12). Applying a voltage to the PZT-actuator then pushes the structure apart stretching the fiber, leading to a phase change at the fiber output and by making the radius of the Pacman larger than the critical bending angle of the fiber, the fiber stretcher introduces no additional losses, besides the unavoidable 0.18 dB/km propagation loss of SMF-28 fiber. To implement the arbitrary phase lock, AC/DC lock for short, two fiber stretchers are used: one for modulating the LO phase and one for scanning and locking. A thorough description of the AC/DC locking scheme is given in sec. 3.4.2.

The HMS consists of a two-level 300×450 mm optical breadboard tower housing the homodyne detector, outcoupling GRIN lenses, 50:50 coupler, manual polarization controller and two fiber stretchers on the upper level together with the WDM, $O \rightarrow E$ converter and Red Pitaya board on the lower level. The breadboard tower is placed on top a rolling cart, with the required electrical components on a lower shelve. These are dual lab power supplies to provide the ± 9 V and ± 19 V required to power the homodyne detector and a pream-plifier. The preamplifier together with a high-voltage amplifier (HVA) amplifies the $0 - 2$ V output of the Red Pitaya to the $0 - 150$ V range permitted to drive

the fiber stretcher PZT-actuators. A function generator (FG), identical to the FG in lab A, is used to generate a similar sample-hold signal in lab B. The two FGs are not synchronized, but by carefully detuning the frequency of the lab B FG and adjusting the phase, the two sample-hold signals can be overlapped and drift by only $\sim 10\ \mu$s over 2 mins. A network router to connect a laptop to the Red Pitaya and DSO to control the AC/DC lock and program the measurement procedure.
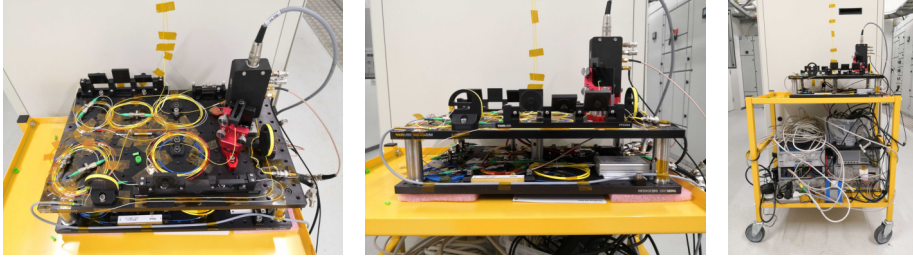
Figure 3.17: Photographs of the HMS placed in lab C (bld. 340)

We know from the theoretical description of homodyne detection (sec. 2.4) that the measurement hinges on the precise cancellation of the classical laser noise of the local oscillator. For a free-space homodyne setup this cancellation is usually achieved by carefully tuning the splitting ratio of the interference beamsplitter, but tuning the coupling ratio of a fixed 50:50 fiber coupler is not possible and so any asymmetry in the splitting ratio has to be balanced by attenuation of one of the fiber arms after the coupler. To this end we use a homemade 3D printed *fiber attenuator*, which consists of a small solid structure with a channel for the fiber, raising it a few mm above the table. The channel has a short gap with an arm piece reaching over. The end of the arm piece is fixed to the table with an M6 screw and by turning the screw the arm piece is lowered, thereby pushing down on the fiber across the gap inducing bending loss. The amount of loss is then controlled by the screw (see fig. A.13).

To reduce optical losses the outcoupling GRIN lenses are spliced to the 50:50 coupler and from the LO side we measure a 48.1% and 47.8% transmission efficiency out of the diodes. The exact splitting ratio is also very slightly polarization dependent and due to the high gain of the HD this leads to a measurable change in DC output when adjusting the LO polarization during HD visibility optimization. And since the polarization is changed whenever a fiber mating sleeve has been disconnected, we routinely have to reoptimize the visibility and rebalance the HD by adjusting the attenuation. From sec. 2.4.1 we know that for small asymmetry in the splitting ratio the attenuation required to balance the HD leads to a loss corresponding to the asymmetry ratio. We therefore

estimate the typical optical loss of the HD, before detection, to be 5% and a 99% visibility.

Homodyne detector

Besides the direct noise cancellation other important performance metrics of a homodyne detector (HD) is the quantum efficiency of the diodes, detection bandwidth and noise clearance of the electrical circuit. The detection efficiency should be as close to unity as possible to not impart additional loss during the detection process and the bandwidth should be large enough to detect all frequency components of the measured field. Finally the detector circuit should handle a high enough LO power to provide a flat frequency response across the relevant bandwidth range at a noise level far above the electrical circuit dark noise. To meet these requirements we use high quantum efficiency AR coated $100\ \mu$m diodes optimized for 1550 nm at a $10 - 15^o$ angle of incident. In order for the photocurrents to be correctly subtracted, the diodes are placed close to each other on opposite sides of the HD PCB. A simplified schematic of the HD circuit is shown in fig. 3.21(a). Here the difference photocurrent is converted to a voltage signal by a trans-impedance amplifier stage and the signal split into a DC and 100 Hz highpass filtered AC output. To confirm that our detector is correctly shotnoise limited across its bandwidth, we measure the balanced noise for different LO powers check that the noise power scales linearly with the optical power. From the measurements we confirm our designed bandwidth of 30 MHz and find that we have 20 dBm of clearance between the electronic noise and shot noise when using a LO power of 1 mW. By ensuring proper focus of the light into the HD diode and comparing the optical input power to the output voltage we estimate a $\eta_q \approx 97\%$ quantum efficiency of the full HD circuit. To total efficiency of the homodyne measurement is therefore estimate to be $\eta_{hd} = 0.95 \cdot 0.99^2 \cdot 0.97 \approx 0.90$.

3.3.2   Measurement configurations

Here we give a description of the three different network configurations and the accompanying modifications of the HMS used for each.

Configuration (1)

Here the network channel is a ~ 1 m SMF fiber placed on the same table as the non-Gaussian state generation setup. We measure the state using only the detector part of the HMS and place the two-level optical breadboard tower on the optical table on pedestals. We further bypass the electrical-to-optical and optical-to-electrical conversion of the trigger signals and feed them directly to the DSO and reuse the 50 kHz gain modulation of the probe beam to generate the AC locking signal for the AC/DC LO lock. Never leaving the optical table results in the setup having excellent long term phase stability, as seen from the squeezing measurements in fig 3.11.

Configuration (2)

Here the network channel is a 60 m SMF connecting lab A to an adjacent lab B. The fiber is pulled through a ventilation tube and into a basement corridor and placed in a standard cable try running along the corridor ceiling. Inside lab A and B the fiber is carefully taped to reduce phase noise, while no special precautions are taken to secure the fiber along the corridor. A map of the basement corridor and the fiber connection can be seen in fig. A.7 of the appendix. Here we measure a channel efficiency of $\sim 95\%$. The less than unity efficiency is mainly caused by the APC/APC couplings in mating sleeves. In general we find that the efficiency for SMF APC/APC connections can very between $100\% and 90\%$, that there can be difference between mating sleeves, that disconnecting and reconnecting the same fiber from the same sleeve does not guarantee that same efficiency and that some fibers, due to imperfections of the fiber tip, never can be coupled with high efficiency using mating sleeves. The precise estimation of optical efficiency therefore becomes difficult when many connection are involved.

For this configuration we first used a homemade *fiber modulator* to modulate the phase at 20 kHz, which provided a clear AC locking signal in lab B. The modulator consisted of stripping the ends of two fiber pigtails and splicing them together without adding a protective sleeve leaving roughly 2 cm of exposed fiber. The bare fiber was then glued to the feet of a U-shaped piece of 3D printed material with a PZT-actuator element squeezing in between the feet below the fiber (see fig. A.13. Modulating the PZT-actuator length then pushed the feet apart thereby stretching the fiber and inducing a phase shift.

While the design does work, the exposed fiber is extremely delicate and in our experience both samples we assembled broke within a few hours of use. Instead to chose to use a second *fiber stretcher*, from which we found a resonance at

14 kHz to give the best result. We also tried to modulate and lock with a single fiber stretcher, but due to the scanning of the PZT-actuator during calibration the AC error signal would be uneven across the scan, thereby prohibiting correct calibration.

Configuration (3)

Here the network channel consists of a 70 m SMF connecting lab A to a node (B307) of the DTU campus fiber network. From there a connection is patched through two other nodes into a separate building (340) on campus. We denote the technical room in which the B340 node is placed as lab C and use a ~ 3 m SMF fiber made from two spliced SC and APC pigtails to couple out of the B340 node and into the HMS. An overview of the entire channel is sketched in fig. 3.18 and a map of the campus network can be seen in fig. A.8. Including the initial 70 m fiber we estimate the total channel length to be ~ 400 m. The patched connection in which the LO and trigger signals are transmitted consists of 10 years old fibers and we measure a total transmission efficiency, from incoupling in lab A to outcoupling in lab C (before the HMS), of $\sim 75\%$. The connection in which the Signal is transmitted uses newer fibers and here we measure an efficiency of $\sim 90\%$. We also find that cleaning the SC/SC couplings at each network node greatly improved the efficiency and so this should be done for any network channel transmitting sensitive quantum states.

To improve the AC locking signal we modify the HMS by removing the second fiber stretcher and instead use a fiber coupled EOM to generate the phase modulation. But since the EOM uses PM fiber we have to use a fiber polarization controller and polariser before the EOM in order to rotate the polarization into the PM fiber and maximize the transmission efficiency. With the polarization controller we get a transmission efficiency of the LO through the polariser and EOM of $\sim 60\%$.
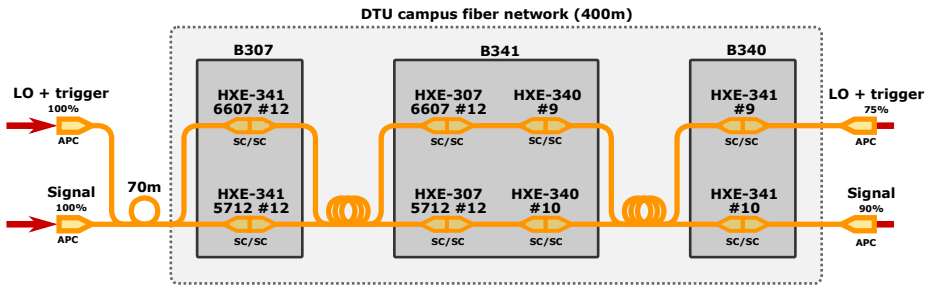

Figure 3.18: test

3.4 Experimental control

An integral challenge to all quantum optics experiments is the stabilization of optical phases and cavity lengths. In general, even on a damped optical table and with sturdy optics mounts or taped fibers the path lengths of different beams are always drifting slightly causing the relative phases to fluctuate. Active feedback is therefore needed to lock the relative phase between interfering beams. The same is true for optical cavities, where it is typically the case the master laser frequency is much more stable than the cavity length (resonance frequency). For a beam to couple resonantly with a cavity, the optical length of the cavity therefore has to be locked to the resonant length defined by the laser frequency.

The general scheme for such locks is a close loop control system, where the interference (or cavity resonance) signal is monitored and used to derive an error signal that is fed to an proportional-integral-derivative (PID) controller which drives the physical feedback mechanism. An excellent introduction to practical feedback control for experimentalist is [74].

3.4.1 Red Pitaya and PyRPL

In our experimental setup all such locks are handled by Red Pitaya (RP) field-programmable gate array (FPGA) boards running the PyRPL (Python Red Pitaya Lockbox) software package [75]. Besides the FPGA chip, the RP is equipped with 2 x analog input and output SMA ports, sampled at 125 MHz using 14 bits. The PyRPL package provides high-level functions and user-interface in python together with a custom FPGA design in Verilog, which implements the various digital signal processing (DSP) modules used for the feedback control systems - *lockboxes* for short. These modules include a two-channel oscilloscope, two arbitrary function generator, four PID controllers with four-order filters, three demodulation (IQ) modules, an infinite impulse response (IIR) filter and a network and spectrum analyser. On a lab computer we therefore have a programmable interface with real-time display and tuneability of all our locks and lockbox parameters. A photograph of the RP setup can be seen in fig A.10 of the appendix.
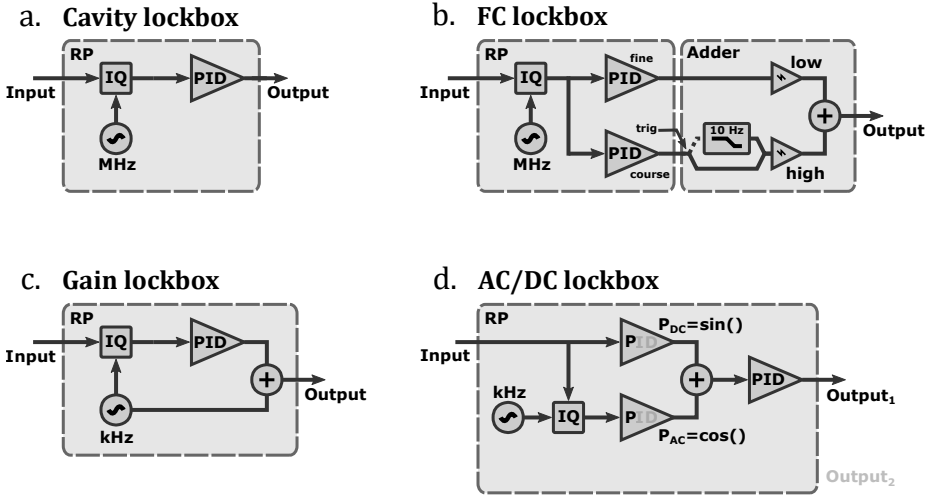
Figure 3.19: Overview of the various cavity and
in PyRPL. The cavity lockbox is used to lock th
the AC/DC lockbox is used to lock the LO phas

3.4.2   Cavity and phase locks

SHG and OPO cavity locking

The lockbox used for the SHG and OPO cavity
In the SHG lockbox the demodulation module o
which is amplified and fed to the EOM in the beg
generate a phase modulation sideband on the ma
up into SHG pump, OPO lock and FC lock bea
the phase reference for the Pound-Drever-Hall (P
a small portion of the circulating cavity light is

mirrors, connected to the PID output through a HVA. In practice we do not use the differential (D) parameter of the PID module and optimize the P and I values by hand.

The exact same locking scheme is used to lock the OPO cavity. But by synchronizing the clock of the SHG and OPO RP boards, the OPO RP does not need to output any modulation signal to the EOM and can reuse the 27.8 MHz phase modulation to generate the error signal.

FC locking

The lockbox used for the FC lock is shown in fig. 3.19(b). The FC RP is also synchronized to the SHG RP, so that the same 27.8 MHz phase modulation signal can be used to lock the FC using the PDH scheme. But due to the high finesse of the FC compared to the SHG and OPO cavities and the finite resolution of the RP DAC a more elaborate locking procedure is used. An error signal is generated in the usual fashion via demodulation, but is then fed to two different PID modules whose output are connected to an external *adder* box. Before adding the two signals, one arm of the adder is amplified with a low gain, while the other arm is amplified with a high gain. The idea is to use the *fine* (low gain) PID to handle small high frequency fluctuations and the *course* (high gain) PID to handle the slower and larger drifts as well as scanning the cavity length. The locking procedure is as follow:

1. The fine PID is inactive and the course PID is set to scan the cavity length slowly (low P and I). A python timer in PyRPL is set to check the input signal value every 10 ms.

2. Once the value is at 50% of the resonance peak height the fine PID is and the course P, I, lockpoint and filter settings are changed.

3. If the lock is lost (input signal goes low) the locking procedure is immediately repeated.

A 10 Hz LPF of the course arm is also included in the adder box, which can be activated by the RP. But in practice we found that switching the filter on caused the lock to break, due to a slight change in phase delay of the course arm relative to the fine. And in general we could maintain a stable lock by tuning the PID parameters and relying on the digital LPF of course arm.

Gain phase locking

The lockbox used for the gain lock is shown in fig. 3.19(c). It implements a AC-locking scheme, similar to the PDH scheme used for cavity locking. As described in sec. 3.1.1 a PZT-actuated mirror in the probe path is used to modulate the probe phase at $f_p = 50$ kHz before the OPO. After the OPO the probe is measured by tapping 1% off from the signal path. Through the parametric gain the input signal at lockbox is then proportional to $\cos(\phi_p + \phi_q + M\cos(2\pi f_p t))$, where ϕ_q is the global phase of the down-converted field equal to the pump phase, ϕ_p is the global probe beam phase and M is the modulation depth, which is assumed small compared to the amplitude of the interference fringe. Disregarding the high frequency part we call this signal the DC signal, since it is obtained directly without any modulation. By demodulation (convoluting with $\cos(2\pi f_p)$ and low-pass filtering) a signal proportional to $-\sin(\phi_q - \phi_p)$ can be obtained. We call this signal the AC signal and use it as the error signal, since it both centred around 0 due to the LPF and is shifted 90° relative to the DC signal. Locking the error signal to 0 then corresponds to locking at the top (amplification) or bottom (de-amplification) of the interference signal between the probe and pump beam. Changing between the two locking regimes is simply done by changing the sign of P and I in PyRPL. The only practical difference to the cavity locks is here then, that the both the modulation and feedback is performed by the same PZT-actuated mirror.

To allow for the PZT-actuated mirror to operate at high frequencies a design based on [76] was used. Here a quarter inch mirror and single-disk (low capacitance) PZT is glued to a tapered brass base with lead filling. The small mirror and tapered interface effectively reduces low frequency drumhead modes, while the lead filling dampens sharp longitudinal resonance modes of the structure.

LO phase locking

The lockbox used for the LO lock is shown in fig. 3.19(c). It implements a AC/DC-locking scheme, where a DC and AC error signal is combined to form a new error signal, shifted by an arbitrary phase in between the two. Since the gain lock sets the relative phase between the pump and probe beam $\phi = \phi_q - \phi_p$, locking the phase between the probe beam and LO $\phi_p - \phi_{lo}$ effectively locks the relative phase between the LO and squeezed vacuum signal field.

From the DC output of the homodyne detector both a DC and AC error signal is derived and fed to individual PID modules. The AC signal is obtained by modulating the LO phase with a fiber stretcher at $f_{lo} = 14$ KHz and demodu-

lating. In both PID modules the I and D values are set to 0 and the P value is used to tune the amplitude of the error signal. By modifying the FPGA code, the output of the PID modules are hardcoded to be summed and used as input to a third PID module. The PID filters should be chosen so that the DC signal is a clean cosine and the AC signal a clean sine. By setting the lockpoint of the DC PID any detector offset can be compensated and by tuning the quadrature factor applied in the IQ module after the demodulation the amplitude of the AC signal can be scaled to the DC signal amplitude.

Once the DC and AC error signals have been properly calibrated, setting $P_{dc} = \sin(\theta)$ and $P_{ac} = \cos(\theta)$ leads to the input signal of the third PID being a sine shifted by θ relative to the AC signal. Thus setting $\theta = 0$ leads to pure AC locking corresponding to locking to the squeezed quadrature, while $\theta = 90^o$ leads to pure DC locking corresponding to locking to the anti-squeezing quadrature. The advantage of this method is that it can be implemented using a single RP board, while the downside is that it requires precise calibration of the error signals to lock to the correct intermediate phase. If either the pump, probe or LO power is changed the locking parameters also have to be reoptimized. Fortunately, thanks to PyRPL, most of the calibration can be automatized.

3.4.3 Sample-hold scheme

When running the experiment we use a *sample-hold* scheme, where first all locking beams and stabilization feedbacks are active during a sample period and then turned off and held constant during a hold period, where measurement data is collected. When running the non-Gaussian experiment we use a sample-hold period of 10 ms, where the locking beams are on for 7 ms, followed by a 0.3 ms dead time before AOM_3, in the trigger channel blocking the SSPD, is opened for 2.5 ms and data is collected followed by another 0.2 ms dead time. The scheme is outlined in fig. 3.20.

Using PDH and AC locking schemes and an on/off switching of the locking beams faster than the drift and bandwidth of the locks, it is in principle not necessary to modify the locks as they will not "see" that the error signal is turned on and off. But since we are using rather slow 100 Hz chopping with a 3 ms hold time, we modify the PyRPL FPGA code in two ways to accommodate; (1) when the sample signal, given to the RP through the extension connectors, is low corresponding to the lock beams being off, the input value of the PIDs is set to 0 so that they keep a constant output value and (2) when the sample signal is high again there is a 1.05 ms delay until the PID output value is updated, ensuring the error signal has time to build up and not cause a sudden jump of the lock due to drifts during the hold period. The 1.05 ms corresponds

to the time needed when a 1 kHz LPF of the error signal is used. The signals used to drive the sample-hold scheme are generated by a 2-channel FG, shown in fig. 3.21. Here channel 1 is the sample signal (100 Hz 70% duty cycle square wave) and is given to the RPs and dual driver of the beam chopping AOMs and channel 2 is the hold signal (100 Hz 25% duty cycle square wave) and is given to the SSPD AOM and the DSO as the qualified trigger for when to trigger on SSPD clicks.
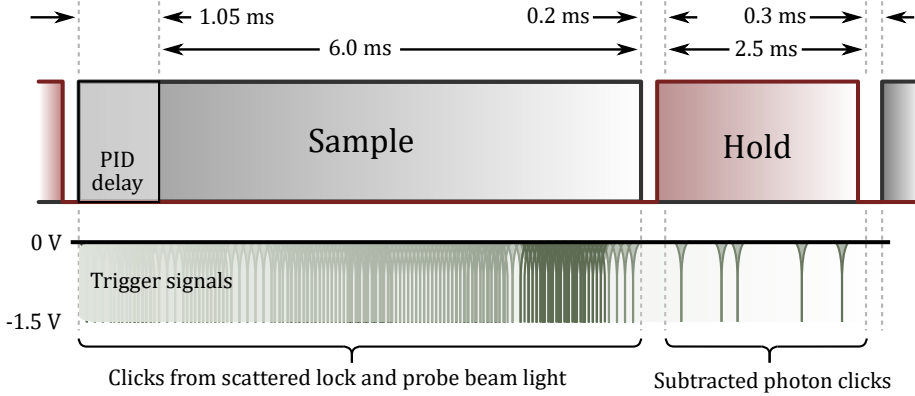
Figure 3.20: The sample-hold scheme. When sample is high lock beams and feedbacks are on, when sample is low lock beams are off and feedbacks kept constant. When hold is high the SSPD is open and the DSO triggered on the SSPD clicks. The high count rate during the sample period is due to strong lock beams scattering through the SSPD AOM, even when it is off.
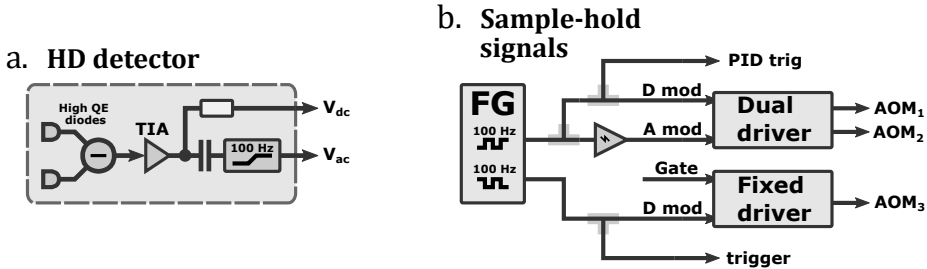
Figure 3.21: (a) Simplified homodyne detector circuit. A trans-impedance amplifier (TIA) stage converts the subtracted photocurrent of the two diodes to a voltage, which is then split into a DC and AC arm. The AC arm is high-pass filtered at 100 Hz to remove any technical DC noise. **(b)** Overview of the signals used to drive the sample-hold scheme. Channel 1 is the sample signal and channel 2 is the hold signal. The A mod signal of the dual driver is amplified to be $0 - 10$ V and the gate signal of the fixed driver is left floating.

CHAPTER 4

Non-Gaussian State Transmission

In this chapter the data collected from the non-Gaussian state transmission project will be analysed and the obtained results compared to the theoretical model developed in sec. 2.3.2. The data presented will the best obtained from three different experimental configurations. In configuration (1) the homodyne stage was placed in lab A on the same optical table as the squeezed light generation stage, in configuration (2) the portable homodyne station was placed in a separate adjacent laboratory (lab B) and in configuration (3) the station was placed in a completely separate building (lab C). The technical details of the configurations are given in sec. 3.3.2. For all configurations the data sets yielding the best results, namely the lowest obtained Wigner negativity, are used for the analysis.

4.1   Experimental run and data collection

When running the experiment our aim is to produce photon subtracted squeezed vacuum states and subsequently verify the quality of those states. To this end we will employ quantum state tomography using data collected via homodyne measurement in order to reconstruct the density matrix and Wigner function of the

generated state. The negativity of the Wigner function will be our benchmark for the performance of our experimental setup. In order for the tomographic reconstruction to be successful we will need both sufficient azimuthal resolution and statistics of the measures state. Based on the analysis of sec. 2.5, we choose to collect 5000 traces at each of six equally separated angles; 0°, 30°, 60°, 90°, 120°, 150°. Since the photon subtracted squeezed vacuum state is π-symmetrical, only data between 0° and 180° needs to be collected. From the model we expect the temporal mode of the photon subtracted squeezed vacuum state to extend roughly 60 ns in time, and therefore choose a trace length of 1 μs with a sampling rate of 500 MS/s, giving a time resolution of 2 ns. Saving a long enough time traces is beneficial for two reasons; firstly the trace has to be long enough to encompass any potential timing delay between the SSPD trigger signal and homodyne photocurrent corresponding to the temporal mode reaching the oscilloscope and secondly it will allow us to extract information about the unconditioned squeezed state away from the signal temporal mode. The experiment is run using the setup in described in cha. 3. Running the experiment consists of:

1. Lock SHG, OPO and FC cavities and then lock the parametric gain to deamplification as described in sec. 3.4.2.

2. Set the OPO pump beam power and transmittance of the tapping beamsplitter (3%).

3. Engage the sample-hold scheme in lab A. For configuration (2) and (3) synchronize the locally generated sample-hold signal to the lab A signal using the SSPD trigger signals as reference.

4. Set the HD DC signal to zero offset by attenuation and calibrate the homodyne AC/DC lock as described in sec. 3.4.2.

5. Trigger the oscilloscope with the SSPD clicks using the hold signal as a qualifier and set the oscilloscope to record a sequence of time traces.

6. For each desired phase angle lock the LO phase and record a measurement sequences.

7. Block the signal channel and record a shot noise sequence.

8. Block the LO and record an electronic noise sequence.

9. Block the OPO pump beam and note down the SSPD fake counts.

Before running the experiment other parameters of the setup should also be checked and optimized if necessary. Typically this includes the OPO threshold

(optimized through pump beam alignment and crystal position and temperature), fiber coupling to the signal GRIN lens, LO polarization for HD interference, GRIN lens coupling to the HD diodes, shielding position to reduce SSPD fake counts as well as locking parameters of cavity and phase locks.

4.2 Data analysis

The data analysis consists of three main steps. Firstly we use the portion of the time traces away from the signal temporal mode to compute power spectrum of the quadrature fluctuations at the different measurement angles of the unconditioned "background" squeezed vacuum. By normalizing to the shot noise spectrum we can then perform curve fitting using the power spectral density formula 2.31 to check if the fitted parameters correspond to the measurement settings. Secondly we determine the shape of the temporal mode function, which we will use to extract the quadrature values from our time traces. Each time trace results in a singular value and so for each measurement angle we build a distribution of quadrature values. Finally we employ the maximum likelihood algorithm, as explained in sec. 2.5, on our set of distributions in order to reconstruct the density matrix corresponding to the quantum state most likely to have produced those exact statistics. From the resulting density matrix we can then directly use eq. 2.10 to calculate the states Wigner function and (hopefully!) confirm the presence of Wigner negativity. The reconstructed Wigner function also serves as an illuminating point of comparison to our theoretical model.

4.2.1 Fitting of unconditioned squeezed vacuum

Before computing the power spectrums we need to determine the position of the photon subtraction event within the time traces. We find the event by computing the time dependent quadrature variance $\left\langle \Delta \hat{q}_\theta(t)^2 \right\rangle$ of the traces locked to the $\hat{x}$ and $\hat{p}$ quadrature, as we expect the noise variance of the photon subtracted state to be larger than the surrounding squeezed vacuum. This is shown in fig. 4.1, where we clearly see a large increase in the noise variance of the anti-squeezed trace as well as a minor increase in the squeezed noise variance. The negative offset of the peak relative to the oscilloscope trigger time ($t = 0$) is due to the timing difference between the arrival of the homodyne photocurrent of the conditioned state and the electrical trigger signal from SSPD electronics. The shape of the peak also reveals some hints about the correlations between the signal and trigger fields and, as we shall see in the next section, can serve

as a guide to determining a suitable temporal mode function.
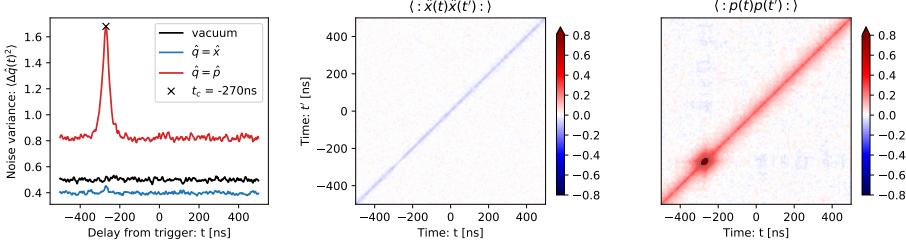
Figure 4.1: (**left**) Noise variance of the vacuum, squeezing and anti-squeezing traces of the D_2 data set. The large peak in the anti-squeezing trace at -192 ns indicates the photon subtraction event. (**right**) Full normal ordered autocovariance matrices of the squeezed and anti-squeezed quadrature, calculated by subtraction the shotnoise covariance matrix.

The variance traces of 4.1(left) could be modelled by taking the expectation value of the convolution of a filter function, corresponding to the homodyne detector impulse response, across the signal quadrature correlations after conditioning. With the conditioned state located in the first half of the time traces at -192 ns relative to the trigger time, we choose to use the second half of the time traces to compute the background noise power spectrum. This procedure is followed for all the presented data sets. We note that the diagonal of the covariance matrix describes the time dependent normal ordered quadrature variance $\langle : \Delta\hat{q}(t)^2 : \rangle = \langle : \hat{q}(t)\hat{q}(t) : \rangle$. From our initial test of a squeezing measurement we expect our LO lock to suffer from some phase fluctuations and include this in our model of the power spectrum by assuming that the actual phase locking point is a normal distribution with a small standard deviation ϕ and that the fluctuations can be different for the AC and DC lock. From [77] this corresponds to a phase offset in the locking angle of ϕ when locked to squeezing and antisqueezing. We therefore modify eq. 2.31 to reflect this

$$\tilde{S}(\theta) = \left[S_x \cos^2 \delta\theta_{ac} + S_p \sin^2 \delta\theta_{dc} \right] \cos^2 \theta$$
$$+ \left[S_p \cos^2 \delta\theta_{ac} + S_x \sin^2 \delta\theta_{dc} \right] \sin^2 \theta \qquad (4.1)$$

As described in sec. 3.4.2 the AC/DC locking scheme requires precious calibration of the AC and DC error signal for the locking points in between 0° and 90° to be accurate. We therefore choose to first fit only the squeezing and antisqueezing traces using eq. 4.1 to obtain en estimate of the bandwidth, pump rate, efficiency, ac and dc phase fluctuations. Afterwards we use the resulting fitting parameters to fit a phase locking offset of the $\{30^o, 60^o, 120^o, 150^o\}$ traces. The result of this analysis is shown in fig. 4.2.
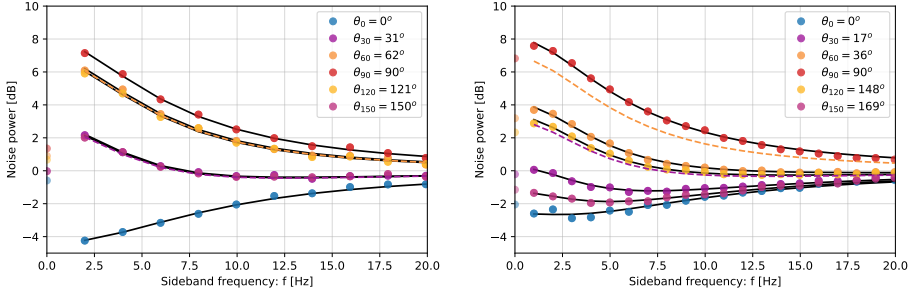
Figure 4.2: Power spectrum fitting of background squeezed vacuum of dataset D_2 (left) and D_3 (right). The dotted lines indicate the expected position of the $\{30^o, 60^o, 120^o, 150^o\}$ traces based on the $\{0^o, 90^o\}$ fit. The fitted locking angles of D_2 are seen to match well with the intended locking angles, while the D_3 fit show both a significant offset from the intended locking angle and a large mismatch between the symmetrical angles.

In order for the fitting routine to estimate uncertainties the phase noise of the DC lock is fixed to 0 during the fit ($\phi_{dc} = 0$). This is justified as the result of the fit is unchanged by including it or not, as its effect is negligible compared to the phase noise of the AC lock ϕ_{ac}. The fitting results are:

$$\gamma_1 = 7.9 \pm 0.2 \text{ MHz} \qquad \gamma_3 = 7.5 \pm 0.2 \text{ MHz}$$
$$\epsilon_1 = 0.48 \pm 0.02 \, \gamma_1 \qquad \epsilon_3 = 0.49 \pm 0.02 \, \gamma_3$$
$$\eta_{s,1} = 0.76 \pm 0.05 \qquad \eta_{s,3} = 0.73 \pm 0.05$$
$$\phi_{ac,1} = 4 \pm 3.5^o \qquad \phi_{ac,3} = 11 \pm 1.2^o \qquad (4.2)$$

The uncertainties are estimated as the 95% uncertainty interval and the fits are generally seen to match the measured data well. The uncertainties of the fitted angles are all within $\pm 1^o$. The difference in OPO bandwidth between the two measurement series is a result of the large phase fluctuations, which causes the fitting routine to be slightly over parametrized as discussed in sec. 3.1.4. The fitted pump rate agrees reasonably well with the 200 mW of 775 nm pump power used for the measurements and the estimated OPO threshold of 788 mW, as $\sqrt{200/788} \approx 0.5$. The fitted efficiencies are also within range of the expected loss, based on the estimation of the loss budget from sec. 3.1.4. But it is worth keeping in mind that when fitting with both the bandwidth γ, pump rate ϵ, loss η and squeezing phase noise ϕ_{ac} the fitting routine is over parametrized and so the fitting result can not be trusted as the true values of the measurement. We therefore only only on the obtained numbers as rough estimates and as a check that the automated measurement process was carried out correctly. Our main take away is e.g. that the AC/DC lock of the homodyne measurement seem to

work correctly for configuration (1), where the measurement is done on the same optical table and low phase drifts of the signal and LO is expected and that for configuration (2) the change of AC locking mechanism and an increased phase drift from the long fiber channel between the two rooms cause the AC/DC lock to become unstable.

4.2.2   Choice of signal temporal mode function

In order to perform the tomographic reconstruction of our state we need to extract quadrature values from our time traces. As described in the derivation of our theoretical model this is done applying a mode function $f_s(t)$ to the time trace and integrating it. Each trace then results in a single quadrature value. The mode function should ideally completely overlap the true temporal mode of the conditioned state for the tomography to give the best result. In order to determine this optimal mode function shape we follow two approaches: firstly we choose three different double-sided exponential functions and perform the full tomographic reconstruction while varying their bandwidth parameters to find the mode shape that results in the largest Wigner negativity, secondly we employ the slightly more elegant approach of expanding the autocovariance function into eigenfunctions and using the function corresponding to the largest eigenvalue as the mode function. This approach relies on the conditioned state having higher variance than the background squeezed vacuum and was first introduced by Morin *et al.* in the context of continuously measured time traces [78]. This approach has been used in previous photon subtraction experiments [79, 80] to provide the optimal mode function and have recently been expanded to also include complex mode functions [81]. To perform the eigenfunction expansion we consider our data as not continuous, but instead discretely binned in time due to our 2 ns measurement resolution. In the discrete scenario the eigenfunction expansion turns high-dimensional principal components analysis (PCA) [82], where we have 1000 dimensions corresponding to the 1 μs measurement time. An excellent description of this equivalence is given in the master thesis of Larsen [83]. The result of using PCA on the covariance matrices in fig. 4.1 is shown in fig. 4.3.
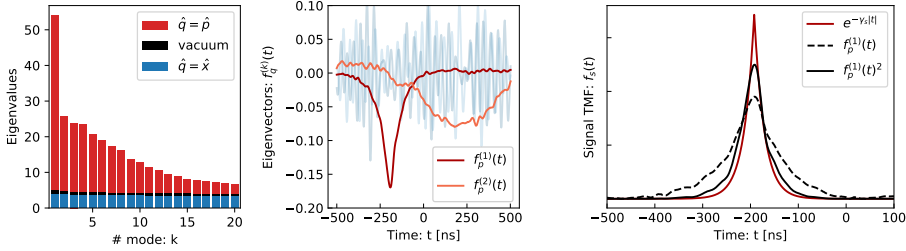
Figure 4.3: (**left**) Eigenvalues of the covariance matrices of D2. (**middle**) Corresponding eigenvectors of the largest and second largest eigenvalues. Red and blue is for the $\hat{p}$ and $\hat{x}$ quadrature respectively. (**right**) The corresponding normalized mode function. The dotted line is the leading eigenvector and solid line is square of that, while the red is the naive guess with a bandwith of 7.5 2πMHz.

From fig. 4.3 we curiously see that the leading eigenvector is quite broad compared to the naive guess and that its square looks more reasonable. This can be explained by the fact that the PCA mode function is only based on the anti-squeezing quadrature which has the bandwidth $\gamma - \epsilon$ and for the high pump rate used here ($x \approx 0.48$) this difference becomes significant. To circumvent this problem an average between then PCA-x and PCA-p can be used, but this is not possible for us due to the low variance of the squeezing measurements. As we will see, we find that using the square of the PCA gives better results and this can be explained by the fact that the square is roughly equal to twice the bandwidth $PCA(t, \gamma)^2 \approx PCA(t, 2\gamma)$. This can also be considered by trying to perform the average using $e^{-\gamma_x|t|} = e^{-|t|/t_x}$, but since the variance of squeezing is so low infinite bandwidth is needed to see the correlations and so $t' = (t_x + t_p)/2 \rightarrow t' = t_x/2$ since $\gamma_p = \infty \rightarrow t_p = 0$.

We normalize all mode functions as $f_s(t) = f_s(t)/\sqrt{\int |f(t)|^2 dt}$ so that $\int f(t)^2 dt = 1$. Using this normalizing the pre-factor on double-sided exponential functions is not required. The functions we use are:

$$f_{s,1}(t) = e^{-\gamma_1|t-t_c|}$$
$$f_{s,2}(t) = e^{-\gamma_1^2|t-t_c|^2/2} \tag{4.3}$$
$$f_{s,3}(t) = \frac{1}{\gamma_1}e^{-\gamma_1|t-t_c|} - \frac{1}{\gamma_2}e^{-\gamma_2|t-t_c|}$$

The result of the brute force optimization for the D_2 dataset is shown in fig. 4.4. Similar optimizations were performed for D_1 and D_3 datasets as well and the results are summarized in tab. 4.1 and 4.2. In general we find that the maximal Wigner negativity is obtained when using a slightly smoothed signal TMF, such

as $f_{s,2}$ or $f_{s,3}$, compared to the sharp shape of $f_{s,1}$. This is to be expected as both the optical filtering of the trigger filter cavity and any electrical lowpass filtering of the detection circuit will result in a smoothing the signal temporal mode. In the summarised results the *PCA mode function* used is the square of the mode function suggested by the PCA analysis, since using the direct mode function did not result in any Wigner negativity. The obtained lower Wigner negativities confirm our suspicion that using the PCA method of deriving the optimal TMF is not the best choice for our data, due to the missing support from the squeezing quadrature.
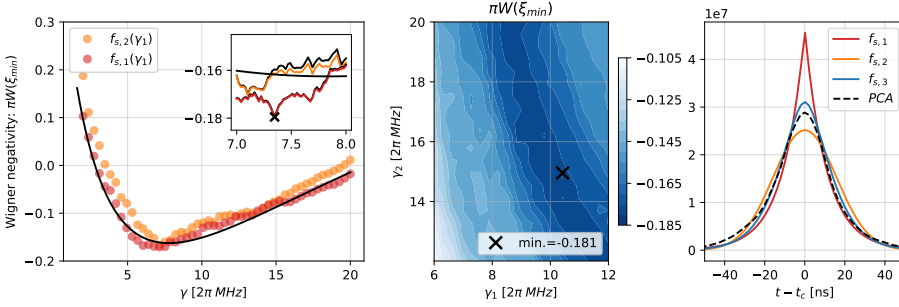
Figure 4.4: (**left+middle**) Optimization of the signal TMF for three different filter functions for the D_2 set. (**right**) The resulting optimal mode functions with the PCA mode being the squared eigenvector. The solid line in the left plot is a fit of the $f_{s,1}$ data points to the model with $\gamma_0 = 8.0$, $\epsilon = 0.48\gamma_0$, $T = 0.97$, $\eta_t = 0.2$ and $\Xi = 0.995$ fixed and the fit returning $\gamma = 7.8 \pm 0.14$, $\kappa = 32 \pm 2$, $\eta_s = 0.728 \pm 0.003$. All frequency numbers are in 2πMHz. The insert shows a higher resolution optimization around the optimal filter width. Here the black curves lying close to the red and orange is the Wigner negativity at $\xi = (0,0)$, showing that the value does not deviate much. This is further supported by that fact that the minimal Wigner values were obtained are all $\xi_{min} < 0.03$.

From our TMF optimization analysis we find that for the D_1 and D_2 measurement series, using the correction to the phase space locking angle obtained from the unconditioned squeezed vacuum power spectrum fitting, does in fact not result in a larger Wigner negativity. While for the D_3 series, taken using configuration (2), a Wigner negativity could be obtained when using the corrected angles. This can be explained from the fact that

		D_1	D_2	D_3
$\{\theta_0\}$	$f_{s,1}$	7.80	7.35	
	$f_{s,2}$	8.76	7.10	
	$f_{s,3}$	12.47, 14.32	10.42, 14.95	
$\{\theta'_k\}$	$f_{s,1}$	5.42	7.34	7.10 (8.45)
	$f_{s,2}$	8.53	7.10	7.45 (8.34)
	$f_{s,3}$	6.76,15.64	10.42,14.95	11.37, 12.43 (9.74, 19.53)

Table 4.1: Table of the optimal decay parameters of the different TMF of the different data sets. Values are in 2πMHz units. The used angles were obtained from the power spectrum fitting of the background squeezed vacuum as $\{\theta_0\} = \{0^o, 30^o, 60^o, 90^o, 120^o, 150^o\}$, $\{\theta'_1\} = \{0^o, 38^o, 68^o, 90^o, 111^o, 139^o\}$, $\{\theta'_2\} = \{0^o, 31^o, 62^o, 90^o, 121^o, 150^o\}$ and $\{\theta'_3\} = \{0^o, 17^o, 36^o, 90^o, 148^o, 169^o\}$.

|		D_1	D_2	D_3
$\{\theta_0\}$	$f_{s,1}$	-0.182	-0.180	$-$
	$f_{s,2}$	-0.206	-0.170	$-$
	$f_{s,3}$	-0.202	-0.181	$-$
	PCA^2	-0.162	-0.171	$-$
$\{\theta'\}$	$f_{s,1}$	-0.151	-0.173	-0.047 (-0.087)
	$f_{s,2}$	-0.172	-0.166	-0.052 (-0.097)
	$f_{s,3}$	-0.185	-0.174	-0.046 (-0.094)
	PCA^2	-0.144	-0.165	-0.042 (-0.080)

Table 4.2: Table of the minimum Wigner negativities obtained for the optimized TMF of tab. 4.1. Values are $\pi W(\xi_{min})$, which have been found to be very close to $\pi W(0,0)$ at the optimal mode function. The second set of values for D_3 has been obtained by disregarding the $\{30^o\}$ measurement sequence.

4.3   Inspection of reconstruction process

As seen from tab. 4.2 a Wigner negativity was observed for 1-PSSqV states measured using configuration (1) and (2). For configuration (3) technical difficulties sadly prevented us from measuring any Wigner negativity. We now then further investigate the tomographic reconstruction process using a datasets from each configuration and applying the optimal $f_{s,1}$ TMF to compare to our model. For configuration (2) we want to ensure the validity of using the corrected locking angles for the reconstruction and for configuration (3) we want to figure out what experimental imperfections prevents us from measuring a Wigner negativity.

4.3.1 Configuration (1)

We start by plotting the quadrature histograms for each measurement angle (as in fig. 2.9) and compare them to the expected marginal distributions of the Wigner function calculated from our model using the parameters obtained from the power spectrum fitting of the background squeezed vacuum. The result is shown in fig. 4.5, where we find good agreement between the measured (red dots), expected (green lines) and reconstructed (black line) quadrature distributions.
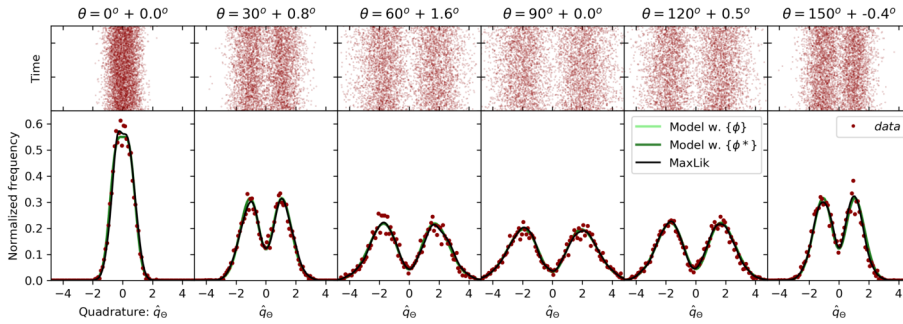
Figure 4.5: Quadrature distributions and histograms of the D_1 dataset, together with the expected marginal distributions using both the set $\{\phi\}$ and corrected $\{\phi^*\}$ locking angles. The quadrature values are extracted using the fitted parameters of eq. 4.2 and $f_{s,1}(t)$ with $\gamma_1 = 7.35\ 2\pi$MHz. The black curve is the marginal distributions of the reconstructed Wigner function. The overlap of all three curves with the measured histograms indicates that the state generation setup and measurement is working as intended.

Using the uncorrected locking angles and quadrature histograms shown in fig. 4.5 we perform the MaxLik reconstruction and the result is shown in fig. 4.6. The reconstructed state has a Wigner negativity of $-0.18\pm0.001\pi$ with a fidelity of 0.98 to the state expected form the model. The fidelity can be increased to ~ 1 by slightly increasing the signal channel efficiency. We therefore feel confident that our model accurately describes the 1-PSSqV state that our setup produces and that our HMS is capable of correctly measuring it. Looking at the density matrix ρ that the MaxLik algorithm directly produces we also see expected behaviour. Our 1-PSSqV states are produced from amplitude squeezed vacuum and so the anti-squeezed quadrature is along the p-axis leading to negative off diagonal terms as well as non-zero imaginary parts. We also see that all ρ_{mn} elements with odd $m-n$ are close to zero, as should be expected from a π-symmetrical state. Due to high pump rate ($x = 0.48$) that was used for the D_1

set the state contains photon number contributions all the way up to $n = 10$ with a mean photon number of 2.46 as well has strong correlations between them as seen from the off-diagonal terms. Rotation invariant (2π-symmetrical) states, such as the fock states, have no off-diagonal terms and so the presence of the off-diagonal terms is also an indication of the CV nature of the state. The diagonal of the density matrix is the photon number distribution and from it we see a small glimpse of the *cat*-like nature of our state - the super position of odd photon number states. This is seen from the fact that ρ_{33} is larger than ρ_{22} and partly by the similar height of the ρ_{55}, ρ_{77} and ρ_{99} terms with their even counterpart. Here the high loss $\eta_s \approx 0.75$ has caused the superposition to degrade. Finally the trace distance of the evolution of the state during the reconstruction process confirms that the algorithm had reached a stable solution after 500 iterations.
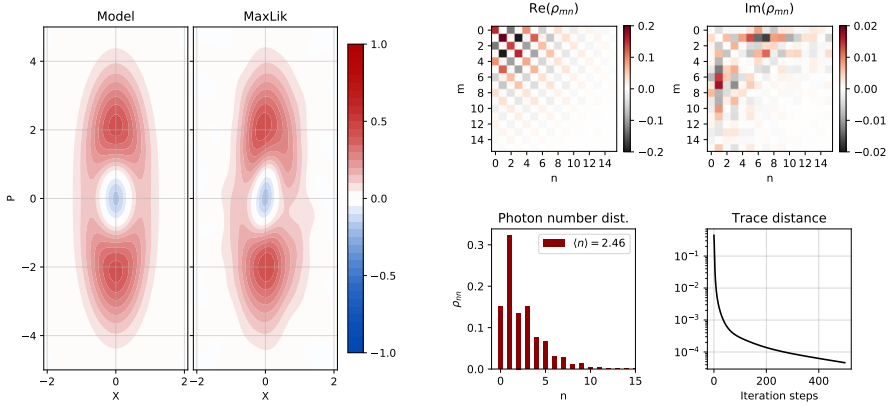
Figure 4.6: (**Left**) Visual comparison of expected and reconstruction Wigner functions of the D_1 dataset. (**Right**) Density matrix output of the MaxLik algorithm together with the photon number distribution and trace distance evolution.

4.3.2 Configuration (2)

Follow the same procedure for configuration (2), as we did for configuration (1), we plot the results in fig. 4.7. Looking at the quadrature histograms we see, as we expected from the power spectrum fitting, that there is a larger discrepancy between the measured and expected quadrature distribution for the set locking angles (light green curve). Using the corrected locking angles appear to result in better agreement between the measured and expected quadrature distributions, though the $\{30°, 150°\}$ measurements still appear off, with $\{30°\}$ slightly worse.
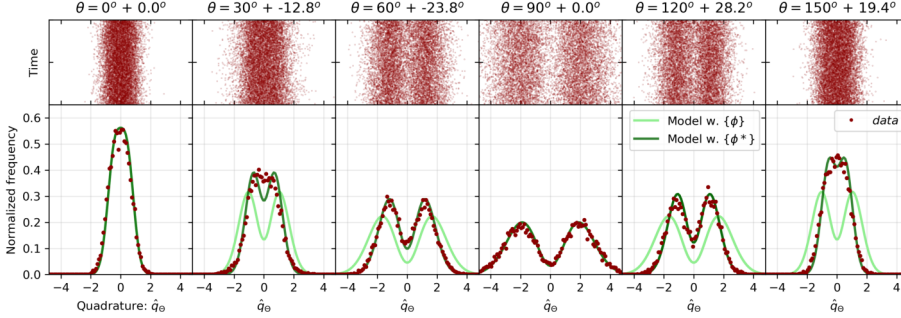
Figure 4.7: D3 hist

It is for this reason that we initially excluded this measurement from the reconstruction, in order to obtain even higher Wigner negativities as seen in tab. 4.2. But is the use of the corrected phase angles for the reconstruction even a valid approach? Surely if these "bad" measurements are truly how the state looks, due to degradation from loss or other sources, it would not be scientifically proper to simply alter (or even exclude!) them from the analysis in order to obtain better results. We are therefore interested in seeing how different experimental imperfections affect the 1-PSSqV state, to determine if the cause of the discrepancy really is an offset in the locking angles. To this end we investigate how three different mechanisms; locking phase noise $\tilde{\theta}$, locking phase offset $\delta\theta$ and loss η_s effects the shape of the expected marginal distributions. From the marginal distributions the effect of locking phase offset and loss can be observed directly and to see the effect of locking phase noise we generate samples from a normal distribution of locking angles centred at the set angles and with variance $\tilde{\theta}$. From the samples we then calculate the corresponding marginal distribution[1]. The result is shown in fig. 4.8.

From the analysis we learn several important features; the shape at $\{90°\}$ is dominantly affected by loss and so its dip gives a good indication of the signal channel efficiency. The closer the measurement angle is to the squeezing angle the more the height of the volcano shape is dependent on the locking phase offset. That a locking phase noise of $\tilde{\theta}$ for $\{0°, 90°\}$ gives a volcano height equivalent to a phase offset of $2\tilde{\theta}$, but with a reduced dip. In that sense phase noise appears like a combination of locking phase offset and loss.

From these observations it is then clear that for the D_3 dataset, the histograms we obtain for $\{30°, 60°, 120°, 150°\}$ only can be explained by a locking phase

---

[1]This approach is similar to what was done in sec. 2.5.2 to generate the simulated quadrature histograms for MaxLik reconstruction.
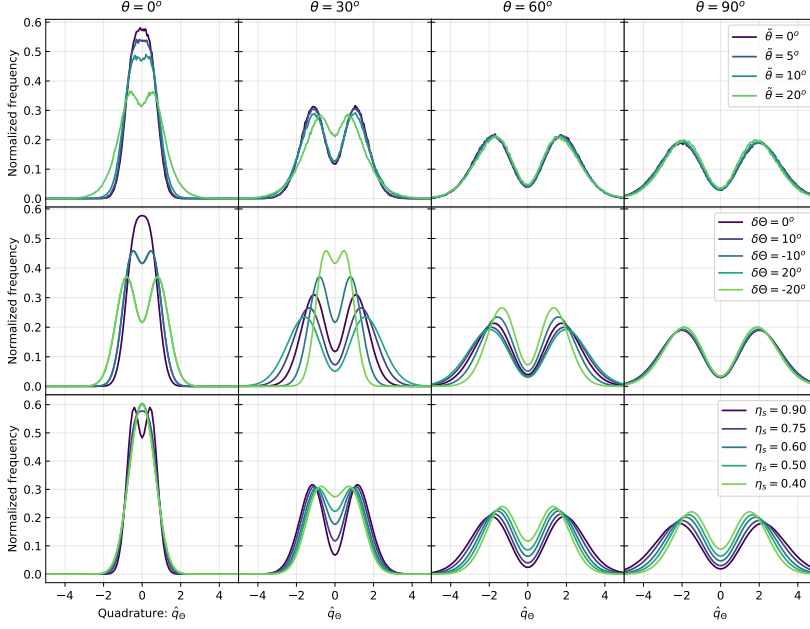
Figure 4.8: Plots of how locking phase noise $\tilde{\theta}$, locking phase offset $\delta\theta$ and loss η_s affects the shape of the marginal distributions of a 1-PSSqV state, calculated from our model with $\gamma = 8$ 2πMHz, $\epsilon = 0.5\gamma$, $T = 0.97$, $\kappa = 30$ 2πMHz, $f_s = 7.5$ 2πMHz, $\eta_s = 0.75$, $\eta_t = 0.2$ and $\Xi = 0.995$

offset, since neither loss or phase noise could have resulted in the large discrepancy we see between the expected and measured distributions for set set locking angles. Another thing to note is that from the power spectrum fits we expect that our measurements should suffer from phase noise of the AC lock and while a phase noise of $\theta \approx 10°$ could explain the discrepancy between the expected and measured distributions for the $\{30° \ 150^circ\}$ measurements it should also reduce the $\{0°\}$ measurement, which should be the most sensitive to phase noise. But we don't see this and so the missing dip for $\{30° \ 150^circ\}$ could be from erroneous low efficiency or large phase noise for those particular measurements, though a sudden drop in efficiency seems unlikely while an increase in locking phase noise is entirely possible as the locking parameters of the AC/DC lock are set and optimized only once before a full measurement run. The optimization consists of adjusting the P and I parameters of the PID module driving the feedback, by looking at the lock for $\theta = 0°$ and $\theta = 90°$. While the AC and DC error signals should in practice be made identical so that the final error signal fed to PID does not change between the measurements, drifts in the experiment can cause them to change. This can both explain how such a locking phase offset can

occur and how, for some measurement angles, the locking parameters could be suboptimal leading to a large locking phase noise. This was especially true for configuration (2), where the modulation for the AC locking signal was provided by a second fiber modulator driven at a resonance of only 14 MHz compared to the 50 KHz of configuration (1). For this reason we also decided to perform the MaxLik reconstruction on the D_3 dataset without including the $\{30° \ 150°\}$ measurements and the result, together with the other reconstructions of the D_3 dataset is shown in fig. 4.9 The Wigner negativity of of the model is -1.403, while the reconstructed states have $-0.045\pm0.001\pi$ and $-0.105\pm0.001\pi$ respectively. The difference can here be explained by either additional loss or phase noise as discussed.
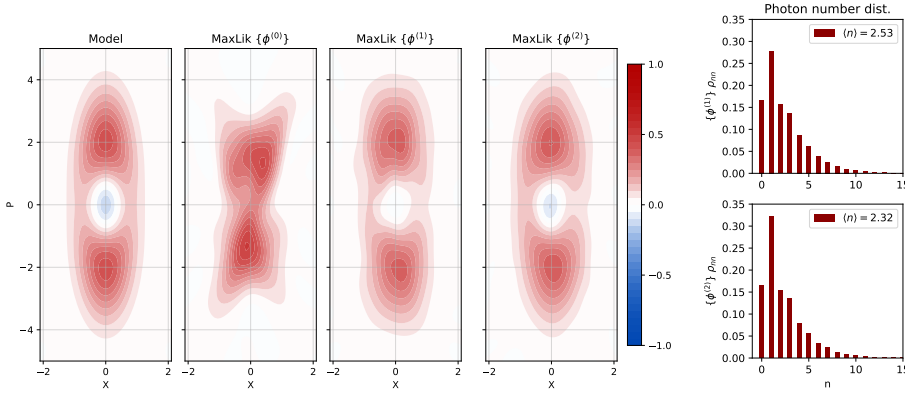

Figure 4.9: (**Left**) Comparison of the Wigner function from the three different reconstructions of the D_3 dataset to the Wigner function expected by the model. $\{\phi^{(0)}\} = \{0°, 30°, 60°, 90°, 120°, 150°\}$ is the set locking angles, $\{\phi^{(1)}\} = \{0°, 17°, 36°, 90°, 148°, 169°\}$ is the corrected angles and $\{\phi^{(2)}\} = \{0°, 36°, 90°, 148°\}$ is with the possibly erroneous measurements excluded. All histograms were created using the $f_{s,1}(t)$ mod function with $\gamma_1 = 2\pi 7.5$ MHz, $2\pi 7.1$ MHz and $2\pi 8.42$ MHz for $\{\phi^{(0)}\}$, $\{\phi^{(1)}\}$ and $\{\phi^{(2)}\}$ respectively.

4.3.3 Configuration (3)

For configuration (3), the true objective of this project, we sadly did not succeed in measuring any Wigner negativity. This was mostly a result of the configuration only being avaible within the final month of the deadline of this thesis, due to the lockdown of the DTU campus caused by the ongoing COVID-19 virus outbreak. Within the available time it was not possible to figure out and solve all the experimental imperfections, but we will still here present the collected

measurement data here. As previously we start by looking at the covariance of
the squeezing and antisqueezing measurements (fig. 4.10). For this measure-
ment (D_4) we used a pump rate of ~ 0.35 is compared to the ~ 0.48 used for the
previous measurements. The reason being that we expected the locking phase
noise to be worse for the measurement configuration due to the longer fiber
network, and so a smaller anti-squeezed level reduces the effect of phase noise.
From fig. 4.10 we see a clear sign of the photon subtraction event. We then pro-
ceed with the curve fitting of the background squeezed vacuum power spectrum,
but already from the observed variance levels we expect the squeezed to be re-
duced from either additional loss or increased phase noise. The fitting results
are as well less clear. Including the AC phase noise term we get $\gamma = 7.0 \pm 0.5$,
$x = 0.28 \pm 0.08$, $\eta_s = 0.66 \pm 0.26$ and $\phi_{ac} = 17 \pm 5°$, which immediately seems
wrong due to the incorrectly fitted pump parameter and high efficiency with
high AC phase noise. Fixing $\phi_{ac} = 0$ we get $\gamma = 8.0 \pm 0.3$, $x = 0.37 \pm 0.015$ and
$\eta_s = 0.37 \pm 0.016$, which both fit the used experimental parameters much better
and has lower fitting uncertainties. For both fits the locking angle corrections
are with $\pm 4°$ from the set angles.
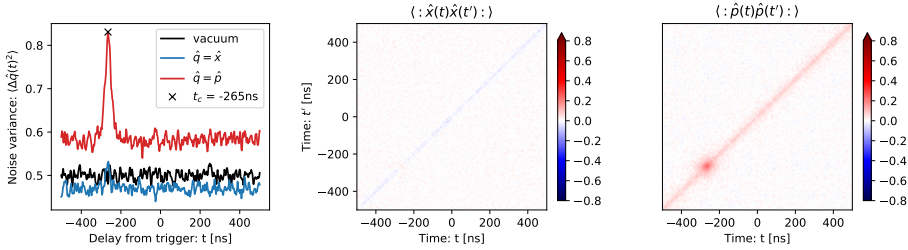
Figure 4.10: Measurement result from configuration (3). A clear sign of the
photon subtraction event can be seen, but the low squeezing level indicate that
Wigner negativity is most likely not preserved.

We then plot the quadrature distributions and histograms and compare them
to the marginal distributions we would expect our model using the two set of
fitted parameters and optimized signal TMF. This is shown in fig. 4.11 and we
clearly see, as we expected, that the darkgreen curve of the fitted parameters
without the AC phase noise term matches the measured data better. From our
previous analysis (fig. 4.8) we also know that the low dip of the {90°} volcano
is mainly caused by loss and so this also suggests that configuration (3) had
a significantly reduced efficiency compared to configuration (1) and (2). This
could be a attributed to the many connections of the fiber network, but from
an independent measurement it was estimated to $\sim 0.90 \pm 0.01\%$.

Even though we could obtain a better match to the measured quadrature dis-

tributions using the fitted parameters excluding the phase noise term, we will conclude our analysis by investigating the actual phase noise that our D_4 measurement suffered from. We do this by keeping all locks and beams constantly on in lab A, while only running the sample-hold scheme on the AC/DC lockbox. This means that we can continuously track the probe intensity from the DC output of the homodyne detector during sample-hold periods, when locked to different LO phases corresponding to a tomographic measurement. An overlay of 200 such traces across two sample-hold periods is shown in fig. 4.12.
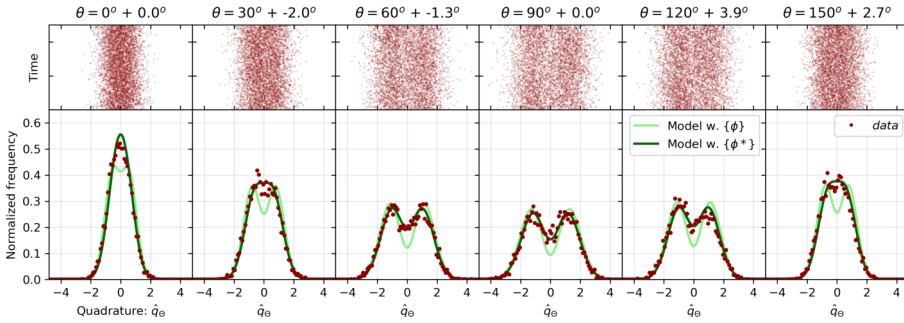

Figure 4.11: Quadrature distributions and histograms of the D_4 dataset, together with the expected marginal distributions using the two different sets of fitted results.

For the traces shown here we used a frequency of 200 Hz with a sample-hold duty-cycle of 60:40. We see that from the moment the hold period starts ($t = 0$), and the feedback is held constant, the phase of the probe relative to the LO starts to drift and that already after ~ 1 ms the phase has drifted more then 180°. For a measurement this would correspond to the measured phase being randomized after 1 ms, and so it seems surprising that our measured quadrature distributions are not worse than they are. To further investigate we also plot a zoom of the first 0.5 ms of the hold period and for the $\{60°, 90°, 120°\}$ measurements calculate the phase noise in degrees as the standard deviation of the phase angle of the sinusoidal interference. This can not straightforwardly be done for the other phases as they close to the interference edge and so the unwrapping of the phase from the noisy traces leads to large uncertainties. The calculation shows that even the strong phase drift caused by the fiber network connection our AC/DC lock is able to maintain a lock with $\sim 4°$ of phase noise and that the phase fluctuations increases to more than $\sim 10°$ after only 0.5 ms of hold time.

One explanation for why such large phase fluctuations does not appear to hurt our measurements more, is that we used a sample-hold frequency of 100 Hz and

that the measurement time for a single set of 5000 sequences, corresponding to 5000 SSPD trigger clicks, was roughly 1.5 mins corresponding to 1 click per sample-hold period. It might be so that the internal speed of the DSO is exactly so slow that it would trigger on the first click of a hold period and then not be ready to trigger again before a new period would start. In that way only data from the first (and best) trigger clicks of each hold-period would be recorded during a measurement sequence. Unfortunately our DSO does not provide timing information on individual traces within a sequences data file to confirm this suspicion.
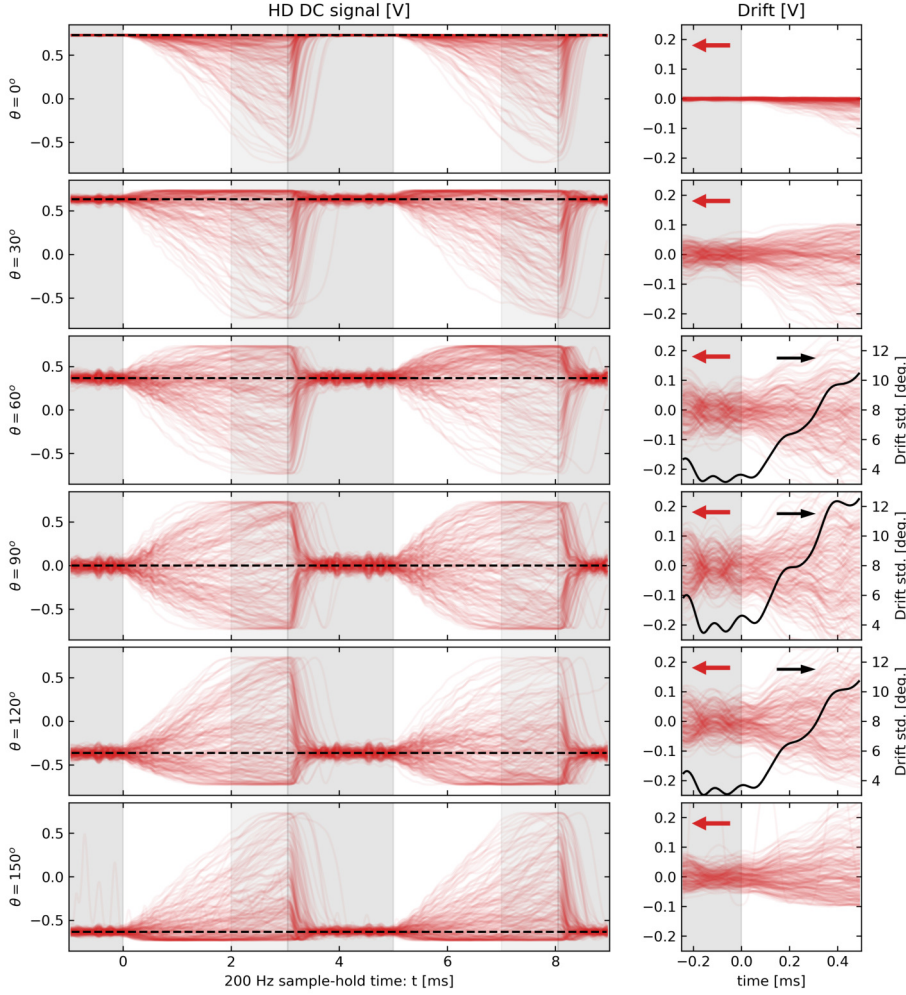
Figure 4.12: Drift of the relative phase between the LO and signal for configuration (3). Visualized as the overlay of 200 time traces across 2 sample-hold periods with a constant probe signal. (**right**) Zoom of the first 0.5 ms of hold time and corresponding phase noise calculated as the standard deviation of the phase fluctuations. The darker shaded area indicate the time duration when the lock is on.

CHAPTER 5

Distributed Quantum Sensing

In 2018 Zhuang *et al.* proposed the first protocol for utilizing CV multipartite entanglement to improve the precision of phase or displacement sensing tasks in a network [14]. Late the following year we then demonstrated the first experimental realization a distributed sensing protocol improved by multipartite entanglement. In our published work we show that for fixed probe resources we obtain an improvement of the root-mean-square (rms) estimation error of sensing the average phase shift across 4 nodes, by using a multipartite entangled probe state as compared to using non-entangled probes. Generally the rms estimation error for protocols utilizing entanglement can scale as the Heisenberg scaling in the number of nodes M, that is $1/M$, while protocols without entanglement only scale as the standard quantum limit $1/\sqrt{M}$. But due to experimental imperfections in our implementation, mainly optical loss, we only show a 20% improvement for $M = 4$ nodes. Due to the scaling advantage of CV multipartite entanglement being highly sensitive to loss, recent advancement have been made in protocols utilizing nonlinear amplifiers [84] or CV error correction codes [85] to improve their robustness against loss. Besides phase sensing distributed quantum sensing have also recently been demonstrated in the context of sensing RF signals [86]. For a more general introduction to using squeezing vacuum for sensing see the review by Lawrie *et al.* [87].

5.1   Experimental setup

The experimental setup used to implement our distributed sensing protocol uses an almost identical setup for generating the squeezed probe as for the non-Gaussian state project. The main difference is the addition of a second EOM in the probe beam path, which is used to create a 3 MHz sideband acting as the probe state for the sensing protocol. The sideband probe state is then squeezed by the OPO, allowing us to adjust the coherent and squeezed part of the probe state by tuning the OPO pump power and EOM modulation strength. The squeezed probe state is then passed through a beamsplitter network (BN) creating the multipartite entanglement between the four exit arms.

In [14] the phases to be sensed is then imagined as a small phase shift in one arm of a Mach-Zehnder interferometer just before homodyne detection in each arm. For four nodes this would requires four phase locked interferometers followed by four LO phase locks and so to reduce the experimental complexity we choose to overlap the LO with the probe before the BN and use QWPs after to transform their polarizations to opposite circular polarizations. We then use the fact that a HWP will shift the relative phase between the two circular polarizations modes and detect them with homodyne detection using a polarization beamsplitter (PBS) to interfere the probe and LO. In this way the QWP+HWP+PBS effectively realises a copropagating Mach-Zehdner interferometer with the phase shift split between the two arms and we only need to lock the probe and LO phase before the BS network. A sketch of the setup is shown in fig. 5.1 and more details are given in the supplement material.
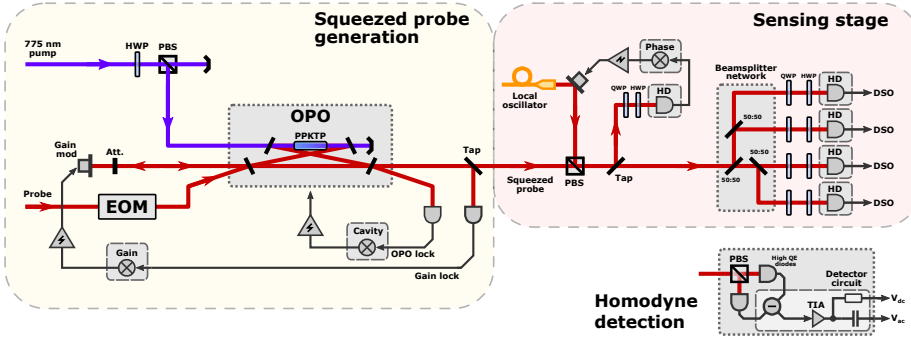
Figure 5.1: Schematic of the setup used for the distributed sensing project. The missing part of the squeezed probe generation stage is identical to the setup used in fig. 3.2. DSO is a 4 channel digital sampling oscilloscope.

Distributed quantum sensing in a continuous-variable entangled network

Xueshi Guo [1]*, **Casper R. Breum** [1], **Johannes Borregaard**[2], **Shuro Izumi**[1], **Mikkel V. Larsen** [1], **Tobias Gehring** [1], **Matthias Christandl**[2], **Jonas S. Neergaard-Nielsen** [1]* and **Ulrik L. Andersen** [1]*

Networking is integral to quantum communications[1] and has significant potential for upscaling quantum computer technologies[2]. Recently, it was realized that the sensing performances of multiple spatially distributed parameters may also be enhanced through the use of an entangled quantum network[3–10]. Here, we experimentally demonstrate how sensing of an averaged phase shift among four distributed nodes benefits from an entangled quantum network. Using a four-mode entangled continuous-variable state, we demonstrate deterministic quantum phase sensing with a precision beyond what is attainable with separable probes. The techniques behind this result can have direct applications in a number of areas ranging from molecular tracking to quantum networks of atomic clocks.

Quantum noise associated with quantum states of light and matter ultimately limits the precision with which measurements can be carried out[11–13]. However, by carefully designing the coherence of this quantum noise to exhibit properties such as entanglement and squeezing, it is possible to measure various physical parameters with significantly improved sensitivity compared to classical sensing schemes[14]. Numerous realizations of quantum sensing utilizing non-classical states of light[15–17] and matter[18] have been reported, but only a few applications have been explored. Examples of these include quantum-enhanced gravitational wave detection[19], the detection of magnetic fields[20–22] and sensing of the viscous-elasticity parameter of yeast cells[23]. All these implementations are, however, restricted to the sensing of a single parameter at a single location.

Spatially distributed sensing of parameters at multiple locations in a network is relevant for applications from local beam tracking[24] to global-scale clock synchronization[3]. The development of quantum networks enables new strategies for achieving enhanced performance in such scenarios. Theoretical works[4–8,25–27] have shown that entanglement can improve sensing capabilities in a network using either twin photons or Greenberger–Horne–Zeilinger (GHZ) states combined with photon number-resolving detectors[5,6] or using continuous-variable (CV) entanglement for the detection of distributed phase space displacements[7]. In this Letter, we experimentally demonstrate an entangled CV network for sensing the average of multiple phase shifts inspired by the theoretical proposal of ref. [7]. We focus on the task of estimating small variations around a known phase in contrast to ab initio phase estimation. We successfully demonstrate deterministic distributed sensing in a network of four nodes with a sensitivity beyond that achievable with a separable approach using similar quantum states.

We start by introducing a theoretical analysis of the networked sensing scheme assuming the existence of an external phase reference. Consider a network of M nodes with optical inputs that undergo individual phase shifts, $\phi_j(j=1, \ldots, M)$. The goal is to estimate the averaged phase shift, $\phi_{\mathrm{avg}} = \sum_{j=1}^{M} \phi_j / M$, among all nodes with as high precision as possible. Two different sensing set-ups are considered: a separable system where the nodes are interrogated with independent quantum states (Fig. 1a) and an entangled system where they are interrogated with a joint quantum state (Fig. 1b). We assume the squeezers give out pure single-mode Gaussian quantum states described by the state vectors $\hat{D}(\alpha)\hat{S}(r)|0\rangle$, where $\hat{D}$ and $\hat{S}$ are the displacement and squeezing operators, respectively, α is the displacement amplitude and r is the squeezing factor. We assume that each probe state undergoes loss in a channel with transmission η. We furthermore restrict the estimator to be the joint phase quadrature, $\hat{P}_{\mathrm{avg}} = \sum_{j=1}^{M} \hat{P}_j / M$ (where $\hat{P}_j$ are the phase quadratures of the individual modes), practically corresponding to the averaged outcome of M individual homodyne detectors. These states and detectors are of particular interest due to their experimental feasibility, inherent deterministic nature, high efficiency and robustness to noise.

Using the separable approach, M identical Gaussian probe states are prepared and individually detected, while in the entangled approach, a single squeezed Gaussian state is distributed evenly to the M nodes via a beamsplitter array and similarly measured individually with homodyne detectors at the nodes. If one wanted to estimate different linear combinations of the phase shifts than simple average, other beamsplitter divisions would be required[4,5]. The sensitivity of the measurement can be defined as the standard deviation (s.d.) of the measurement which, by error propagation, is[13]

$$\sigma = \frac{\sqrt{\left\langle \Delta \hat{P}_{\mathrm{avg}}^2 \right\rangle}}{|\partial \langle \hat{P}_{\mathrm{avg}} \rangle / \partial \phi_{\mathrm{avg}}|} \tag{1}$$

where $\left\langle \Delta \hat{P}_{\mathrm{avg}}^2 \right\rangle = \left\langle \hat{P}_{\mathrm{avg}}^2 \right\rangle - \left\langle \hat{P}_{\mathrm{avg}} \right\rangle^2$ is the variance of the estimator. We are only interested in the sensitivity for small phase shifts, because one can always use an initial rough phase estimation to adjust the homodyne detector (the local oscillator phase) to the maximum sensitivity setting[16]. For small phase shifts, we obtain the sensitivities for the separable (σ_{s}) and entangled (σ_{e}) approaches (Supplementary Section I):

$$\sigma_{\mathrm{s}} = \frac{\sqrt{e^{-2r_{\mathrm{s}}} + 1/\eta - 1}}{2\alpha_{\mathrm{s}}\sqrt{M}} \tag{2}$$

[1]Center for Macroscopic Quantum States (bigQ), Department of Physics, Technical University of Denmark, Lyngby, Denmark. [2]QMATH, Department of Mathematical Sciences, University of Copenhagen, Copenhagen, Denmark. *e-mail: xguo@fysik.dtu.dk; jsne@fysik.dtu.dk; ulrik.andersen@fysik.dtu.dk
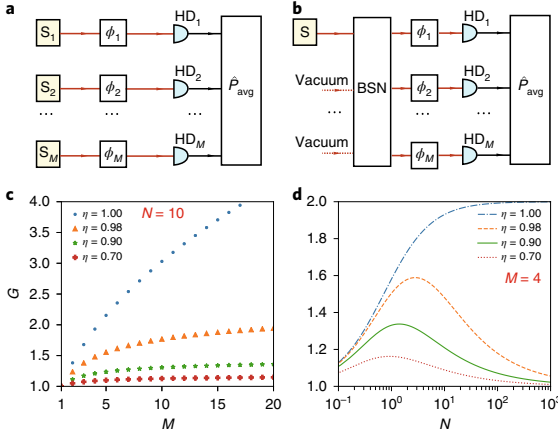
Fig. 1 | Distributed phase sensing scheme. The task is to estimate the average value of M spatially distributed small phase shifts $\phi_1, ..., \phi_M$. **a**, Without a network, the average phase shift must be estimated by probing each sample individually. This can be done with homodyne detection of the phase quadrature ($HD_1, ..., HD_M$), and the sensitivity can be increased by using squeezed probes generated by M independent squeezers $S_1, ..., S_M$. **b**, If the M sites are connected by an optical beamsplitter network (BSN), a single squeezed probe can be distributed among the sites. This enables entanglement-enhanced sensing of the average phase shift. **c**,**d**, The entangled approach of **b** shows a gain in sensitivity compared to the separable approach in **a** for the same number of photons, N, hitting each sample and with optimized probe states. This gain, $G = \sigma_s^{opt}/\sigma_e^{opt}$, is plotted as a function of the number of samples M with N fixed at 10 (**c**) and as a function of the average number of photons with M fixed at 4 (**d**) for different values of η, the efficiency of the channel between pure resource state and phase sample.

$$\sigma_e = \frac{\sqrt{e^{-2r_e} + 1/\eta - 1}}{2\alpha_e} \qquad (3)$$

We now constrain the average number of photons, N, hitting each sample. The photons can be separated into those originating from coherent displacement and those originating from squeezing: $N = N_{s,coh} + N_{s,sqz} = \eta(\alpha_s^2 + \sinh^2 r_s)$ for the separable case and $N = N_{e,coh} + N_{e,sqz} = \eta(\alpha_e^2 + \sinh^2 r_e)/M$ for the entangled case. The ratio between photon numbers, parametrized as $\mu_{s(e)} = N_{s(e),sqz}/N$ can be tuned to give the optimal sensitivities

$$\sigma_s^{opt} = \frac{1}{2\sqrt{M}\,N} \sqrt{\frac{N(1-\eta) + \frac{\eta}{2}(1 + \sqrt{1 + 4N(1-\eta)})}{1 + \eta/N}} \qquad (4)$$

$$\sigma_e^{opt} = \frac{1}{2MN} \sqrt{\frac{MN(1-\eta) + \frac{\eta}{2}(1 + \sqrt{1 + 4MN(1-\eta)})}{1 + \eta/(MN)}} \qquad (5)$$

For perfect efficiency ($\eta = 1$), it is clear that the sensitivity of the entangled system yields Heisenberg scaling both in the number of nodes ($1/M$) and the number of photons per mode ($1/N$), whereas the separable system only achieves the latter and a classical $1/\sqrt{M}$-scaling with the number of modes. The gain in sensitivity of the entangled network relative to the separable network (denoted $G = \sigma_s^{opt}/\sigma_e^{opt}$) is thus $G = \sqrt{M}$.

For non-ideal efficiency, the Heisenberg scaling ceases to exist, in accordance with previous work on single parameter estimation[28]. In fact, for $\eta \to 0$, both sensitivities approach $1/2\sqrt{MN}$. Still, it is important to note that the entangled network exhibits superior behaviour for any value of η, M and N for optimized μ_s, μ_e. Some examples for the sensitivity gain are illustrated in Fig. 1c,d. From Fig. 1d where a network of $M = 4$ nodes is considered, it is clear that the highest gain in sensitivity is attained at a finite photon number. We also note that, for large photon numbers, the gain tends to unity for non-zero loss, meaning no enhanced sensitivity when using the entangled approach. However, there is still a practical advantage for the entangled approach: only one squeezed state is needed compared to the M squeezed states with similar squeezing levels for the separable approach (Supplementary Section I).

Next, we demonstrate experimentally the superiority of using an entangled network for distributed sensing. A schematic outline for the experimental set-up is shown in Fig. 2a (for more details see Extended Data Fig. 1, Methods and Supplementary Section II). The entangled network is realized by dividing equally a displaced single-mode squeezed state into four spatial modes by means of three balanced beamsplitters. These entangled probe states are then sent to the four nodes of the network, where they each undergo a phase shift ϕ_j and are finally measured with high-efficiency balanced homodyne detectors that are set to measure the phase quadrature, $\hat{p}_j$. The external phase reference is set by the local oscillator, which co-propagates with the probes through the set-up but in a different polarization mode. This ensures that the relative phases between the probes and the local oscillator can be controlled. The resulting photocurrents from the four detectors are further processed and subsequently combined to produce the averaged phase shift. For demonstration purpose, we set all ϕ_j to the same value $\phi_j = \phi_{avg}$, but in principle they could be different.

An experimental run is shown in Fig. 2b. In this particular run, a displaced squeezed state is prepared with an average photon number of $N = 2.48 \pm 0.12$ in each mode, of which $N_{e,sqz} = 0.30 \pm 0.01$ photons are from the squeezing operation and $N_{e,coh} = 2.19 \pm 0.11$ are from the phase modulation, as this distribution is near-optimal for the entangled case. We then impose 12 different ϕ_{avg} values by phase shifts at each node while recording the Fourier transformed homodyne detector outputs; the spectra around the 3 MHz sideband for six of the ϕ_{avg} values are shown in Fig. 2b. These outputs yield poor estimates of the individual phase shifts (because the squeezing in each mode is only ~0.8 dB), but the averaged phase shift, obtained by summing the photocurrents, produces an entanglement-enhanced estimate with significantly lower noise, ~5 dB squeezing. The spectra for the averaged photocurrents are shown in Fig. 2c. For comparison, we also simulate the separable approach by directing the entire displaced squeezed state (with properly optimized parameters) to a single node. We then perform the phase estimation at that node and scale the obtained sensitivity by $\sqrt{4}$ to obtain the projected performance for an average over four identical sites.

We quantify the performance of the sensing network by estimating the sensitivities of the two approaches based on the averaged homodyne measurement outcomes, P_{avg}. By extracting the rate of change with respect to a phase rotation, $|\partial\langle\hat{P}_{avg}\rangle/\partial\phi_{avg}|$, as well as the variance, $\langle\Delta\hat{P}_{avg}^2\rangle$, of P_{avg}, we deduce the sensitivity using equation (1). See Supplementary Section IV for more details on the data analysis. For the experimental runs described above, we obtain sensitivities of $\sigma_e = 0.099 \pm 0.003$ and $\sigma_s = 0.118 \pm 0.002$ for the entangled and separable approach, respectively. These correspond to single-shot resolvable distributed phase shifts (that is, phase shifts for which the signal-to-noise ratio is unity) of $5.66° \pm 0.18°$ for the entangled case and $6.76° \pm 0.11°$ for the separable case with ~2.5 photons. Using a coherent state instead of the squeezed state, the minimal resolvable phase for 2.5 photons is $9.06° \pm 0.07°$,
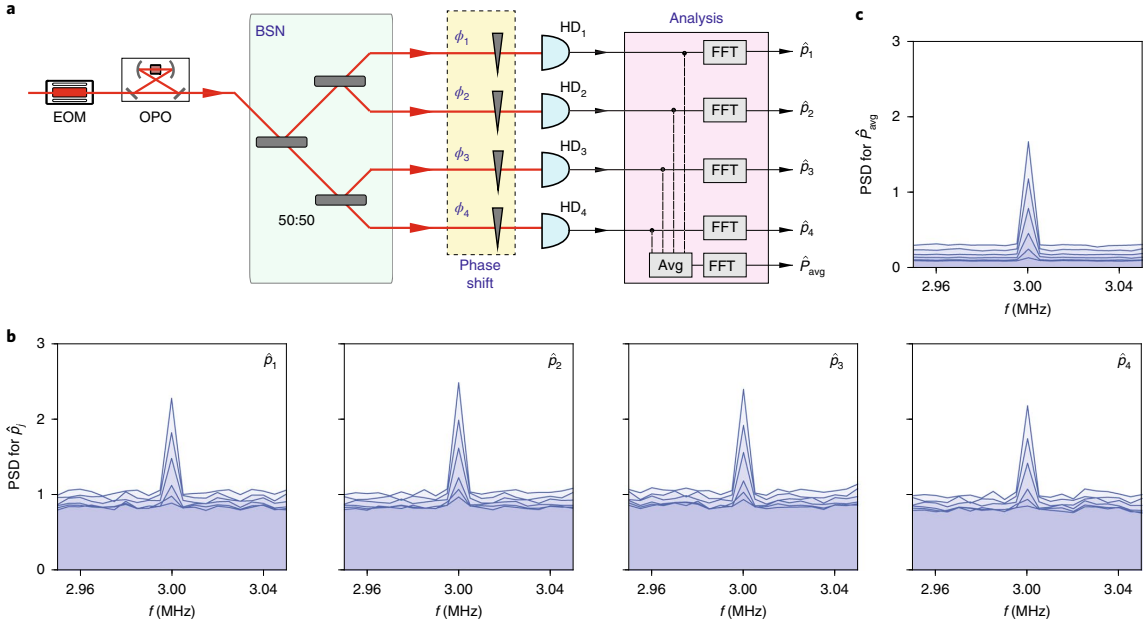
Fig. 2 | Experimental scheme. a, A simplified outline of the experimental set-up for the entangled approach with $M = 4$ (see Supplementary Section II for details). A 1,550 nm laser beam is phase-modulated at 3 MHz by an electro-optic modulator (EOM) and injected into an optical parametric oscillator (OPO). This prepares a displaced squeezed state at the 3 MHz sideband. A BSN splits the state into four identical and entangled probes, which are used to sense the average phase shift of ϕ_1 to ϕ_4. After phase shifting, the probes' phase quadratures $\hat{p}_j$ are measured with homodyne detection set-ups (HD$_1$ to HD$_4$), whose outputs are recorded by an oscilloscope. The power spectral densities (PSDs) of the individual modes as well as their average, $\hat{P}_{\mathrm{avg}}$, are obtained from fast Fourier transforms (FFTs) of the oscilloscope traces. This set-up can be reduced to the separable approach ($M = 1$) by removing the BSN and sending the state to one phase shift and HD. **b,c**, Example PSD results for $\hat{p}_j$ (**b**) and $\hat{P}_{\mathrm{avg}}$ (**c**) from one experimental run for the entangled approach, $M = 4$. Each trace is an average of 2,000 FFTs. We record the spectra for varying settings of the phase shifts. Here, the values of ϕ_{avg} are 0.3°, 4.2°, 8.2°, 12.1°, 16.1° and 20.0° from the bottom curve to the top curve in the plots (see Supplementary Section III for details of phase calibration). Due to the quantum correlations of the entangled probes, the noise of $\hat{P}_{\mathrm{avg}}$ reduces significantly compared to $\hat{p}_j$. From these spectra, $\left\langle \hat{P}_{\mathrm{avg}} \right\rangle$ and $\left\langle \Delta \hat{P}_{\mathrm{avg}}^2 \right\rangle$, which constitute the sensitivity σ, are extracted: the peak and the noise level of the spectrum for $\hat{P}_{\mathrm{avg}}$ are respectively given by $\left\langle \hat{P}_{\mathrm{avg}}^2 \right\rangle$ and $\left\langle \Delta \hat{P}_{\mathrm{avg}}^2 \right\rangle = \left\langle \hat{P}_{\mathrm{avg}}^2 \right\rangle - \left\langle \hat{P}_{\mathrm{avg}} \right\rangle^2$.

corresponding to the standard quantum limit. Note that these angles are larger than our small phase shift approximation (which requires ϕ_{avg} to be much smaller than ~7° for the conditions in this experimental run; Supplementary Section I). In practice, this means that it is necessary to probe the sample more than once to resolve the small phases implemented in the experiment. Sampling the phases K times will result in $\sqrt{K}$ times smaller resolvable phase shift angles. The entangled strategy will still benefit from the enhanced sensitivity per probe.

We find the sensitivities for different total average photon numbers both for the entangled and separable network, and plot the results in Fig. 3a. For every selection of the total photon number, we adjust μ to a near-optimal value for optimized sensitivity (Fig. 3b,c). It is clear in Fig. 3a that both realizations beat the standard quantum limit (reachable by coherent states of light) and, most importantly, we see that the entangled network outperforms the separable network. The ultimate sensitivity of our entangled approach is not reached in our implementation (see Methods and Extended Data Fig. 2). However, homodyne detection will not, even in principle, saturate this bound, and non-Gaussian measurements are in general needed.

Our results demonstrate experimentally how mode entanglement, here in the form of squeezing of a collective quadrature of a multimode light field, can enhance the sensitivity in a distributed

sensing scenario. The main limitation of the scheme when applied to realistic scenarios will be the channel efficiency, which will eventually limit the achievable gain. Other technical challenges will be to supply phase-locked local oscillators to each site that are separate from the probe beams and to suppress the spectral parts of the squeezed light that does not contribute to the sensing. On the other hand, because the probes are generated from a simple beamsplitter network, it will be straightforward to scale to more modes where the sensitivity gain may be even larger (Fig. 1c). Consequently, we believe that techniques demonstrated in this proof-of-principle experiment have direct applications in a number of areas. Specifically, beam tracking, relevant for molecular tracking[24], could benefit from these techniques. Such applications impose limits on the allowed probe power to prevent photon damage and heating of the systems. Mode entanglement can thus be used to increase sensitivity without increasing the probe power. Using squeezed coherent light for quantum non-demolition (QND) measurements has also been exploited for the generation of spin squeezing in atomic ensembles[29] and optical magnetometry[20]. Although this is usually considered for single ensembles, the generalization to multiple ensembles can provide enhanced sensitivity and new primitives for quantum information processing. Combining several ensembles for magnetometry and utilizing mode entanglement would further reduce the shot noise and increase the sensitivity of a collective
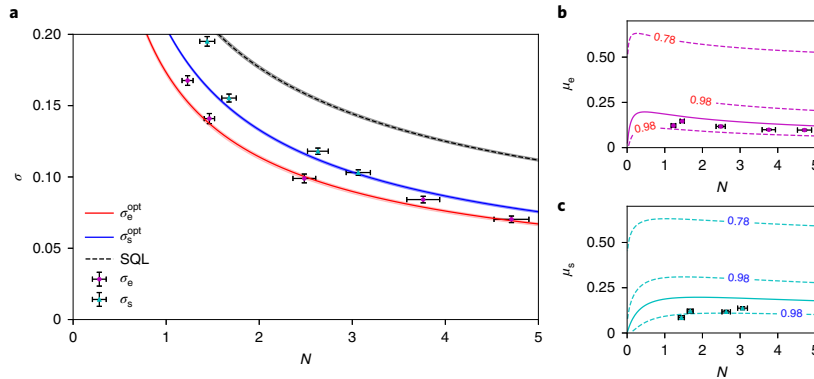
Fig. 3 | Phase sensitivity results. a, Sensitivity to ϕ_{avg} for different average numbers of photons per sample N for the entangled scheme (σ_e) and the separable scheme (σ_s). The sensitivities predicted in theory, $\sigma_e^{opt}/\sigma_s^{opt}$, are plotted with shaded lines, where the shadows show the upper/lower bound within the overall efficiency $\eta = 73.5 \pm 1.5\%$ of our experimental set-up. SQL indicates the standard quantum limit, for which no squeezer but only coherent states are used. The result shows that both schemes perform better than the SQL and that the entangled network outperforms the separable network. **b**, Data points are the values of μ_e (the proportion of N originating from the squeezing process) obtained in the experiment. The solid curves are the optimal μ_e that minimize σ at a given N. The contours indicate the values of σ_e^{opt}/σ_e. **c**, As **b**, but for the separable approach. All error bars are $\pm$s.d. assuming a normal distribution.

optical measurement. Performing a collective optical QND measurement of several atomic ensembles can prepare a distributed spin-squeezed state for quantum network applications. In particular, squeezing of multiple optical lattice clocks could be used for collective enhancement of clock stability[3,30]. In ref. [30], this was obtained by letting a single probe interact with all ensembles in a sequential manner. However, by utilizing mode entanglement, this can be performed in a parallel fashion with no quantum signal being transmitted between the ensembles.

Online content

Any methods, additional references, Nature Research reporting summaries, source data, extended data, supplementary information, acknowledgements, peer review information; details of author contributions and competing interests; and statements of data and code availability are available at https://doi.org/10.1038/s41567-019-0743-x.

References

1. Wehner, S., Elkouss, D. & Hanson, R. Quantum internet: a vision for the road ahead. *Science* **362**, 9288 (2018).
2. Nickerson, N. H., Li, Y. & Benjamin, S. C. Topological quantum computing with a very noisy network and local error rates approaching one percent. *Nat. Commun.* **4**, 1756 (2013).
3. Kómár, P. et al. A quantum network of clocks. *Nat. Phys.* **10**, 582–587 (2014).
4. Eldredge, Z., Foss-Feig, M., Gross, J. A., Rolston, S. L. & Gorshkov, A. V. Optimal and secure measurement protocols for quantum sensor networks. *Phys. Rev. A* **97**, 042337 (2018).
5. Proctor, T. J., Knott, P. A. & Dunningham, J. A. Multiparameter estimation in networked quantum sensors. *Phys. Rev. Lett.* **120**, 080501 (2018).
6. Ge, W., Jacobs, K., Eldredge, Z., Gorshkov, A. V. & Foss-Feig, M. Distributed quantum metrology with linear networks and separable inputs. *Phys. Rev. Lett.* **121**, 43604 (2018).
7. Zhuang, Q., Zhang, Z. & Shapiro, J. H. Distributed quantum sensing using continuous-variable multipartite entanglement. *Phys. Rev. A* **97**, 032329 (2018).
8. Humphreys, P. C., Barbieri, M., Datta, A. & Walmsley, I. A. Quantum enhanced multiple phase estimation. *Phys. Rev. Lett.* **111**, 070403 (2013).
9. Gagatsos, C. N., Branford, D. & Datta, A. Gaussian systems for quantum-enhanced multiple phase estimation. *Phys. Rev. A* **94**, 042342 (2016).
10. Polino, E. et al. Experimental multiphase estimation on a chip. *Optica* **6**, 288–295 (2019).
11. Giovannetti, V., Lloyd, S. & Maccone, L. Quantum metrology. *Phys. Rev. Lett.* **96**, 010401 (2006).
12. Escher, B. M., De Matos Filho, R. L. & Davidovich, L. General framework for estimating the ultimate precision limit in noisy quantum-enhanced metrology. *Nat. Phys.* **7**, 406–411 (2011).
13. Giovannetti, V., Lloyd, S. & Maccone, L. Advances in quantum metrology. *Nat. Photon.* **5**, 222–229 (2011).
14. Caves, C. M. Quantum-mechanical noise in an interferometer. *Phys. Rev. D* **23**, 1693–1708 (1981).
15. Yonezawa, H. et al. Quantum-enhanced optical-phase tracking. *Science* **337**, 1514–1517 (2012).
16. Berni, A. A. et al. Ab initio quantum-enhanced optical phase estimation using real-time feedback control. *Nat. Photon.* **9**, 577–581 (2015).
17. Slussarenko, S. et al. Unconditional violation of the shot-noise limit in photonic quantum metrology. *Nat. Photon.* **11**, 700–703 (2017).
18. Muessel, W., Strobel, H., Linnemann, D., Hume, D. B. & Oberthaler, M. K. Scalable spin squeezing for quantum-enhanced magnetometry with Bose–Einstein condensates. *Phys. Rev. Lett.* **113**, 103004 (2014).
19. The LIGO Scientific Collaboration. A gravitational wave observatory operating beyond the quantum shot-noise limit. *Nat. Phys.* **7**, 962–965 (2011).
20. Wolfgramm, F. et al. Squeezed-light optical magnetometry. *Phys. Rev. Lett.* **105**, 053601 (2010).
21. Li, B.-B. et al. Quantum enhanced optomechanical magnetometry. *Optica* **5**, 850–856 (2018).
22. Jones, J. A. et al. Magnetic field sensing beyond the standard quantum limit using 10-spin noon states. *Science* **324**, 1166–1168 (2009).
23. Taylor, M. A. et al. Biological measurement beyond the quantum limit. *Nat. Photon.* **7**, 229–233 (2013).
24. Qi, H., Brádler, K., Weedbrook, C. & Guha, S. Ultimate limit of quantum beam tracking. Preprint at https://arxiv.org/abs/1808.01302 (2018).
25. Knott, P. A. et al. Local versus global strategies in multiparameter estimation. *Phys. Rev. A* **94**, 062312 (2016).
26. Baumgratz, T. & Datta, A. Quantum enhanced estimation of a multidimensional field. *Phys. Rev. Lett.* **116**, 030801 (2016).
27. Pezzè, L. et al. Optimal measurements for simultaneous quantum estimation of multiple phases. *Phys. Rev. Lett.* **119**, 130504 (2017).
28. Knysh, S., Smelyanskiy, V. N. & Durkin, G. A. Scaling laws for precision in quantum interferometry and the bifurcation landscape of the optimal state. *Phys. Rev. A* **83**, 021804 (2011).
29. Hammerer, K., Sørensen, A. S. & Polzik, E. S. Quantum interface between light and atomic ensembles. *Rev. Mod. Phys.* **82**, 1041–1093 (2010).
30. Polzik, E. S. & Ye, J. Entanglement and spin squeezing in a network of distant optical lattice clocks. *Phys. Rev. A* **93**, 021404 (2016).

Methods

Outline of the experimental methods. Full details of the experimental set-up and data analysis are provided in Supplementary Sections II–IV. A brief outline is given here.

With this set-up, squeezed vacuum at 1,550 nm wavelength is generated in a bowtie-shaped OPO containing a periodically poled KTiOPO$_4$ crystal (Extended Data Fig. 1a). The OPO cavity has a half-width at half-maximum bandwidth of 8.0 MHz, an oscillation threshold of 850 mW and 95% escape efficiency. It is pumped by 775 nm light generated by second harmonic generation in an identical cavity. Two 1,550 nm beams are injected into the cavity through a high reflector: one beam propagates against the direction of the squeezed light and is used for locking the cavity length and the other beam co-propagates and serves multiple purposes. First, this latter beam exits the cavity in the same spatial mode as the squeezing and is therefore used for alignment with the local oscillator. Second, it is used for locking the phase of the squeezing through the classical parametric gain, observed after tapping off 1% of the light. Third, and most important, it serves as the coherent displacement part of our probes. For this purpose, it is modulated at 3 MHz by an EOM. The modulation depth determines the amplitude of the displacement. Finally, it is used as the phase reference for locking the probe state and the local oscillator (LO) phase for homodyne detection.

The LO used in all four homodyne detectors is combined with the squeezed probe on a polarizing beamsplitter (PBS) in orthogonal polarizations prior to the distribution of the combined beams in the beamsplitter network (Extended Data Fig. 1b). Because the LO is co-propagating with the signals in the same spatial modes, balanced homodyne detection—which is inherently insensitive to noise in the LO—is achieved by changing the fields to orthogonal circular polarizations with $\lambda/4$ wave plates and subsequently mixing and splitting the fields on PBSs. The PBS outputs are then detected on a balanced photodetector (Extended Data Fig. 1c). To lock the local oscillator to either the phase or amplitude quadrature of the probe, 1% is tapped off and detected with a homodyne detection set-up identical to those at the four sensing sites. All locks in the set-up are controlled by the PyRPL software package[31] running on a PC and multiple RedPitaya FPGA boards. At each of the sensing sites, as well as at the LO phase lock, the relative phase of the LO and probe is manually controlled by a $\lambda/2$ wave plate. Before the measurements, the wave plates are carefully calibrated in order to be able to apply a well-defined phase shift to the probe states. Turning the $\lambda/2$ wave plate by 1° induces a 4° phase shift.

The data for the sensitivity measurements are obtained by simultaneously recording 200 μs-long oscilloscope traces of the high-pass filtered homodyne detector signals. The power spectral density is then calculated via the FFT of these traces and, from each, the single point at 3.000 MHz is extracted for further processing. Finally, the phase estimation sensitivities are obtained from fitting to simple sinusoidal models the amplitudes of the sideband peaks and the background noise floors as a function of the induced phase shift.

Mode definition of the optical field for sensing. The choice of modulation for generation of the coherent displacement defines the spectral mode of the probing scheme: a narrow 5 kHz band around the 3 MHz optical sideband of the 1,550 nm carrier. This sideband is chosen as it is in the spectral region of our source with maximum squeezing. At higher frequencies, the squeezing reduces due to the limited bandwidth of the OPO, while at lower frequencies, it is degraded by technical noise. Equivalently, the temporal mode is given by the 200 μs oscilloscope trace length. The spatial mode of the beams (~1.8 mm diameter) and their polarization also add to the definition of the optical mode that probes the sample, and it is the average photon number within this mode that counts as the resource of the phase sensing. Note that there are no fundamental restrictions in the scheme on the optical modes employed. In any practical setting, they would be chosen based on the nature of both the squeezing source and the samples being probed. In this work, the classical, separable and entangled schemes are compared using the same mode definitions. One could of course consider choosing different modes for a classical or separable scheme, but the relevant comparison of the schemes is still in terms of sensitivity versus average photon number within the mode. Whichever mode is chosen for each of the three schemes, as long as there is multimode squeezing (entanglement), the entangled scheme will outperform the other schemes.

In this proof-of-principle experiment, many photons outside the sensing mode still hit the sample, even though they do not count in the resource calculations. For applications where the power on the sample is restricted, these 'inactive' photons should be avoided. Photons from the local oscillator can be avoided by using individual local oscillators locally at the sites, combined with the probes after phase sampling. Photons in the carrier of the coherent modulation can be filtered away optically. The same is true for squeezed photons outside the employed spectral mode. Conversely, the spectral mode could be extended to contain most of the bandwidth of the squeezed OPO output.

Quantum Cramér–Rao bound for ϕ_{avg} sensing. Throughout the experiment, we did not try to pursue the ultimate sensitivity by using optimal probe states and optimal measurements. This means that the sensitivity for ϕ_{avg} sensing, with both the separable approach and the entangled approach, can be further optimized. Here, we confine the discussion to Gaussian states, and analyse the ultimate sensitivity limit for ϕ_{avg} sensing for a given probe with the help of the quantum

Cramér–Rao bound (QCRB). We also compare the QCRB for ϕ_{avg} sensing to the counterpart of single parameter phase sensing by using a single-mode Gaussian state as the probe, as discussed in detail in ref. [32]. We assume the sensing channel has a constant efficiency $\eta < 1$.

For a general sensing problem, the QCRB sets a lower bound, minimized over all possible measurements, on the uncertainty with which a parameter ϕ can be estimated through an unbiased estimator $\tilde{\phi}$, given a probe in a certain quantum state: $\left\langle \Delta \tilde{\phi}^2 \right\rangle \geq F_\phi^{-1}$, where F_ϕ is the quantum Fisher information. The ultimate sensitivity limit for sensing of a single phase shift is thus $\sigma_\phi^{CR} = 1/\sqrt{F_\phi}$. The quantum Fisher information for single-mode phase sensing using a Gaussian probe with initial displacement α and squeezing r is given by[32]

$$F_{sm} = \frac{e^{2r'}}{2N_{th}+1}\alpha^2 + \frac{(2N_{th}+1)^2(e^{4r'}+e^{-4r'}-2)}{(4N_{th}+2)^2+4} \qquad (6)$$

with an effective thermalization photon number, due to loss, of

$$N_{th} = \frac{1}{2}[(\eta e^{-2r}+1-\eta)(\eta e^{2r}+1-\eta)-1]$$

and an effective squeezing parameter

$$r' = \frac{1}{4}\log\left[\frac{\eta e^{2r}+1-\eta}{\eta e^{-2r}+1-\eta}\right]$$

The QCRB for sensing of an average ϕ_{avg} of multiple phase shifts with coherent probes, σ_{coh}^{CR}, and with our separable approach, σ_{sep}^{CR}, can also be found from equation (6), divided by $\sqrt{M}$ to account for the M independent phase estimations.

For non-trivial estimation involving multiple parameters, the quantum Fisher information matrix (QFIM) is needed. The variance of an unbiased estimator $\tilde{q}$ of an arbitrary linear combination of M parameters, $q = \sum_{i=1}^M w_i \phi_i$, is $\left\langle \Delta \tilde{q}^2 \right\rangle = \mathbf{w}^T K \mathbf{w}$ with the weight coefficients $\mathbf{w}^T = (w_1, \ldots, w_M)$ and parameter covariance matrix K with $K_{ij} = \left\langle (\tilde{\phi}_i - \phi_i)(\tilde{\phi}_j - \phi_j) \right\rangle$. Given a quantum Fisher information matrix F, the QCRB is expressed as

$$\left\langle \Delta \tilde{q}^2 \right\rangle = \mathbf{w}^T K \mathbf{w} \geq \mathbf{w}^T F^{-1} \mathbf{w} = \sigma_q^{CR} \qquad (7)$$

The QCRB for ϕ_{avg} with the entangled scheme where the weights are $\mathbf{w}_{avg}^T = (1/4, 1/4, 1/4, 1/4)$ is then

$$\sigma_{ent}^{CR} = \mathbf{w}_{avg}^T F_{ent}^{-1} \mathbf{w}_{avg} = \frac{1}{16}\sum_{i,j=1}^4 (F_{ent}^{-1})_{ij} \qquad (8)$$

How to calculate the QFIM for arbitrary multimode Gaussian states, as well as the existence (or not) of a measurement that reaches the bound, is discussed in refs. [33,34]. We use equations (16)–(21) in ref. [34] to numerically calculate F_{ent}. As discussed in ref. [33], when any of the symplectic eigenvalues of the quadrature covariance matrix of the Gaussian state has unity value, the process in ref. [34] gives a singular result. This applies to our entangled scheme, because it has three vacuum input modes. We solve this numerical problem pragmatically by replacing the three vacuum input states with very weak thermal states (10^{-6} mean photon number in each).

The optimal QCRBs for different scenarios, together with the optimal sensitivity of our measurement schemes σ_s^{opt} and σ_e^{opt}, are shown in Extended Data Fig. 2. The QCRBs are optimized over α and r for a fixed mean photon number. For the $\eta = 0.735$ detection efficiency, the states optimizing the QCRBs are all squeezed vacuum states. It is interesting to compare this with ref. [35], where it is shown that for pure states ($\eta = 1$), the optimal Gaussian probes to sense a parameter encoded in a BSN (ϕ_{avg} is a special case of such a parameter) can be prepared by sending a single-mode squeezed vacuum state into one port of the BSN and vacuum states to all the other ports. This is equivalent to what we do in our entangled scheme. At our detection efficiency, we find

$$\sigma_{coh}^{CR} > \sigma_s^{opt} > \sigma_e^{opt} > \sigma_{sep}^{CR} > \sigma_{ent}^{CR} \qquad (9)$$

The sensitivities obtained do not reach the corresponding ultimate limits. Furthermore, these relations show that, in principle, it should be possible to reach a better sensitivity with a separable scheme than what is obtained with the entangled scheme. However, the difference between them is small and—to the best of our knowledge—no efficient way of experimentally implementing a measurement to reach the ultimate limit σ_{sep}^{CR} is known. In ref. [36], it is discussed that an $\hat{X}\hat{P} + \hat{P}\hat{X}$ type of measurement is needed to reach the QCRB when $\eta < 1$. This is non-Gaussian and cannot be realized by only Gaussian operations such as squeezing, beamsplitters, phase shifts and homodyne/heterodyne detection. For sensing involving multiple parameters, a joint, non-Gaussian measurement may be optimal, but the experimental approaches to reach the optimal bound σ_{ent}^{CR} remain unclear.

Finally, note that the QCRB of the entangled scheme overlaps with that of the single parameter estimation. This makes sense intuitively: splitting a resource state equally into four and using these to probe the average of four phase shifts should result in the same sensitivity as that of a single phase shift probed by the same unsplit resource.

Data availability
The data represented in Figs. 2 and 3 and Supplementary Fig. 6b are available as Source Data or Supplementary Data. Raw oscilloscope data and data analysis scripts are available at https://doi.org/10.11583/DTU.9988805. All other data that support the plots within this paper and other findings of this study are available from the corresponding author upon reasonable request.

References
31. Neuhaus, L. et al. PyRPL (Python Red Pitaya Lockbox)—an open-source software package for FPGA-controlled quantum optics experiments. In *Proc. 2017 Conference on Lasers and Electro-Optics Europe & European Quantum Electronics Conference* 8087380, (IEEE, 2017).
32. Pinel, O., Jian, P., Treps, N., Fabre, C. & Braun, D. Quantum parameter estimation using general single-mode Gaussian states. *Phys. Rev. A* **88**, 040102 (2013).
33. Šafránek, D. Estimation of Gaussian quantum states. *J. Phys. A* **52**, 035304 (2018).
34. Nichols, R., Liuzzo-Scorpo, P., Knott, P. A. & Adesso, G. Multiparameter Gaussian quantum metrology. *Phys. Rev. A* **98**, 012114 (2018).
35. Matsubara, T., Facchi, P., Giovannetti, V. & Yuasa, K. Optimal Gaussian metrology for generic multimode interferometric circuit. *N. J. Phys.* **21**, 033014 (2019).
36. Oh, C. et al. Optimal Gaussian measurements for phase estimation in single-mode Gaussian metrology. *npj Quantum Inf.* **5**, 10 (2019).

Author contributions
J.B., U.L.A., J.S.N.-N., T.G., X.G. and C.R.B. conceived the experiment. X.G., C.R.B. and M.V.L. performed the experiment and analysed the data. J.B., X.G., S.I., M.C. and J.S.N.-N. worked on the theoretical analysis. X.G. wrote the paper with contributions from J.B., C.R.B., S.I., J.S.N.-N. and U.L.A. J.S.N.-N. and U.L.A. supervised the project.

## Competing interests
The authors declare no competing interests.

Additional information
**Extended data** is available for this paper at https://doi.org/10.1038/s41567-019-0743-x.

Supplementary information is available for this paper at https://doi.org/10.1038/s41567-019-0743-x.

Correspondence and requests for materials should be addressed to X.G., J.S.N.-N. or U.L.A.

Reprints and permissions information is available at www.nature.com/reprints.
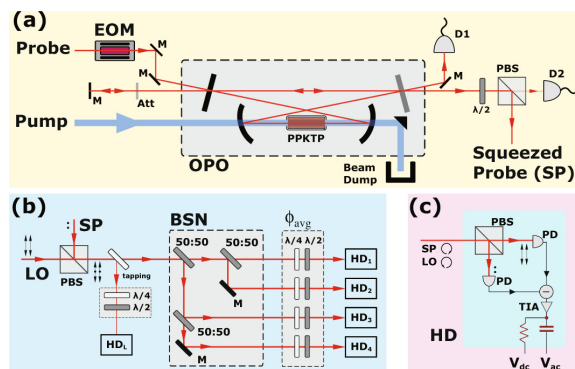
Extended Data Fig. 1 | Experimental Setup. See Supplementary Sec. II for details. (**a**) Single mode displaced squeezed state generation at the 3 MHz side band; (**b**) A proof-of-principle experimental setup for distributed phase sensing with entangled probes. The local oscillator (LO) is used as external phase reference, and the phase shift is introduced by wave plates; (**c**) The balanced homodyne detection setup corresponding to HD_1 to HD_4 in (**b**).
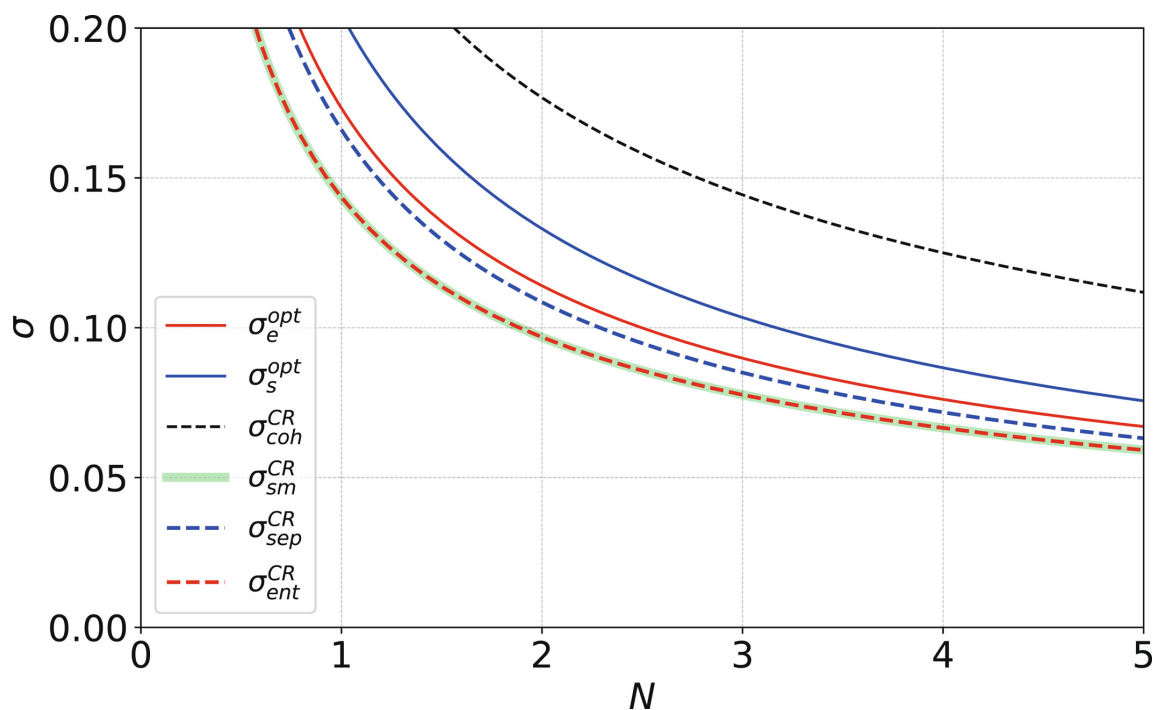
Extended Data Fig. 2 | Optimal sensitivities and quantum Cramér–Rao bounds (QCRB) for different scenarios. All calculated with a total efficiency of $\eta = 0.735$ as in our experiment. The optimal sensitivity of our separable scheme σ_s^{opt} and entangled scheme σ_e^{opt} are plotted in solid blue and red, respectively. These are derived in the Supplementary Material Section I. The remaining four curves show the QCRBs derived in the Methods section: The optimal QCRB for ϕ_{avg} sensing with coherent probes (σ_{coh}^{CR}, dashed black), the separable scheme with squeezed probes (σ_s^{CR}, dashed blue), and the entangled scheme (σ_e^{CR}, dashed red), as well as the QCRB for single parameter phase sensing with a squeezed probe (σ_{sm}^{CR}, solid green).

CHAPTER 6

Outlook

In this thesis two projects related to quantum information processing in networks, namely the *non-Gauusian state transmission* project (1) and the *distributed quantum sensing* project (2), were discussed. The goal of project (1) was to transmit a continuous variable non-Gaussian state across a short distance network channel and to measure its Wigner negativity at the receiver side as a sign of the non-Gaussianity of the received state. For project (2) the goal was to use a multi-partite entangled probe state to show a sensitivity advantage over a non-entangled probe states for the sensing of distributed phase shifts in a network. First, before presenting the results of either project, the theory of continuous variable quantum optics were introduced together with a realistic model of the experimental procedure for generating a one photon subtracted squeezed vacuum state (1-PSSqV). An implementation of the maximum likelihood algorithm for tomographic reconstruction of states measured by homodyne detection was also discussed. Next, the experimental setup constructed to perform the measurements for both projects was described. Finally the result of project (1) was presented as a detailed analysis of the data collected for the different measurement configurations, while the results of project (2) was presented in the form of the published work.

Non-Gauusian state transmission

For the *non-Gauusian state transmission* project we build a setup consisting of
a SHG cavity in order to generate continuous wave squeezed vacuum at 1550 nm
via parametric down conversion in an OPO cavity. To subtract single photons
from the squeezed vacuum field, we employed the conventional scheme of using
a weakly reflecting beamsplitter to tap a small portion of the squeezed field into
a trigger channel where the detection of a single photon heralds the subtracted
state in a signal channel. In the trigger channel we constructed a frequency
filter system consisting of a narrow linear filter cavity and a DWDM bandpass
filter. For the filter cavity we developed a locking scheme to efficiently lock the
cavity using an FPGA based lockbox controlled by the PyRPL software suite.
The single photons were detected by a single photon detector based on super-
conducting niobium titanium nitride nanowires. We characterized the trigger
channel to have a total detection efficiency of 20% and with careful shielding
of the optical setup dark count rates of $10 - 50$ Hz were achieved. To measure
the heralded state we designed and assembled a portable measurement station
based on a fiber coupled homodyne detector setup and characterized it to have a
total detection efficiency of 90%. By coupling the generated non-Gaussian state
into single mode fiber, transmitting it through three different network channel
configurations and measuring using the portable measurement station, the re-
ceived states were characterized by quantum tomography.

For configuration (1), in which the channel was a 1 m fiber and the measurement
station was placed on the same optical table, we measured a maximal Wigner
negativity of -0.206π with a mean photon number of 2.54. For configuration
(2), in which the channel was a single 60 m fiber terminating at an adjacent
lab, we measured a maximal Wigner negativity of -0.105 with a mean photon
number of 2.345. Here we also showed how carefully analysing the tomographic
process allowed us to compensate for incorrect measurement settings. For con-
figuration (3), in which the channel was a ~ 300 m connection through the
DTU campus fiber network terminating in a separate building, we could sadly
not measure any Wigner negativity before concluding the project. In the end
we found, for yet unknown reasons, that the efficiency of the signal channel had
severely decreased between the measurements of configuration (2) and (3).

For configuration (3) we performed measurements of the phase fluctuations of
the fiber channel and found that, while severe, our locking scheme could com-
pensate for them and determined that a holding time of no longer than a few
100 μs will be required. The most obvious point of improvement is the optical
transmission efficiency of the signal channel. Improving this efficiency can be
done in three places; locally in lab A by checking the transmission efficiency of
all optical components in the signal channel, by cleaning all fiber connections of

the campus network and by rebuilding the measurement station using a higher quality beamsplitter and resplicing the fiber connections. Besides the optical efficiency the expected Wigner negativity can also be improved by using an even lower pump rate and by reducing the length of the filter cavity to increase its bandwidth. We therefore strongly believe that given the improvements listed measuring Wigner negativity of a CV non-Gaussian state transmitted troiugh the DTU campus network is entirely possible with our setup.

Besides measuring the Wigner negativity by improving the optical loss of the signal channel other interesting paths to pursue could be to use a true local-local oscillator setup to perform the homodyne measurements, thereby reducing the channel requirements to a single quantum channel for network transmission. This could be implemented in our setup by either adding a pilot tone during the sample period or by placing it a high sideband frequency outside of the bandwidth of the 1-PSSqV state [88]. Another interesting experiment could be split the cat state on a 50:50 beamsplitter and direct either half to different buildings and measure them using identical measurement stations. Since our SSPD has 6 channels, we could also easily split the trigger channel after frequency filtering onto several SSPDs in order to generate up to six photon subtracted squeezing vacuum states. Though using this approach the measurement time would scale exponentially due to the decreased success probability of a trigger events and so the long term stability of our setup and especially the fake count rate becomes increasingly important. Beside the fundamentally interesting aspects of creating large non-Gaussian state, other protocols more relevent for quantum communication tasks could be pursued, such as CV entanglement distribution and distillation across the network [89]

Regarding the measurement station there are also possible points of improvement. From our data analysis we found that locking to the angles between 0° and 90° could be problematic for our implementation of the AC/DC lock. This issue could be circumvented adding a second homodyne detector and changing the measurement setup to hetorodyne detection, in which the signal is split on a 50:50 beamsplitter and one half is measured in x-quadrature and the other in the p-quadrature. In this way the entire phase space of the Q-function is sampled at once and only a pure AC and pure DC lock is required [81]. The usual difficulty of getting two interference visibilities close to unity is further reduces by using a fiber setup, where we found that a > 0.99 visibility routinely could be achieved. For the measurement presented in chap. 4 a "slow" sample-hold scheme was used. Here slow means that the sampling frequency was well below the locking bandwidth and we therefore had to hold all locks during data collection. This of course allows for long measurement traces to be collected, but as we saw from the measurement of the phase noise of the full fiber network (fig. 4.12) this is of no use as the phase drifts too quickly. We should therefore opt to use the "fast" sample-hold scheme, in which the sampling frequency is much higher than the

locking bandwidth and so the locks can be kept continuously on, as they won't see the on/off switching of the locking signals. One thing to solve would then be the synchronization of the sample-hold signal generated in lab A and lab C. If solved, using this method our measurement should then only suffer from the locking phase noise, which we found to be $\sim 4°$ for configuration (3).

Distributed quantum sensing

For the distributed sensing project, which was carried out before the non-Gaussian state transmission project in the old lab, we also build a setup to generate squeezing vacuum from using parametric down-conversion in an OPO cavity as well as the four node free-space network consisting of three 50:50 beamsplitters and eight QWPs and HWPs. For the project we developed the technique of using overlapped probe and LO signals in opposite circular polarizations to realise a phase shift between the two modes using only a HWP. This allowed us to to scale the network size to four nodes without having to deal with the otherwise eight phase locks. With the entangled probe state we showed a roughly 20% improvement in root-mean-square estimation error compared to a non-entangled probe, for the sensing task of measured the average phase shift of the four nodes. The main obstacle preventing us from showing a better scaling was the 75% total optical efficiency of the network channels. To obtain the maximal sensitivity with our experimental setup we had to carefully optimize the distribution of coherent and squeezed photons within the entangled probe state. As this project was a proof-of-principle experiment and since we had to disassemble the experimental setup completely, we have no current plans for developing the experiment further.

Though an interesting idea could be to use the same scheme of overlapped LO and probe state to implement a multipass sensing protocol. In **??** Higgins *et al.* show how passing a probe state through a phaseshift multiple times can linearly increase the accumulated phase and thereby leading to a Heisenberg limited measurement sensitivity. In experimental setup they used polarization NOON states created by passing a heralded single photon trough a PBS. But due to the heralding their scheme was only probabilistic. Using a setup similar to what we build for this project, but with a multipass stage as in **??** (HWP in between two mirrors and QWPs) instead of the beamsplitter network we could show, assuming low enough loss, a deterministic Heisenberg limited scaling in the number of probe passes of the multipass stage.
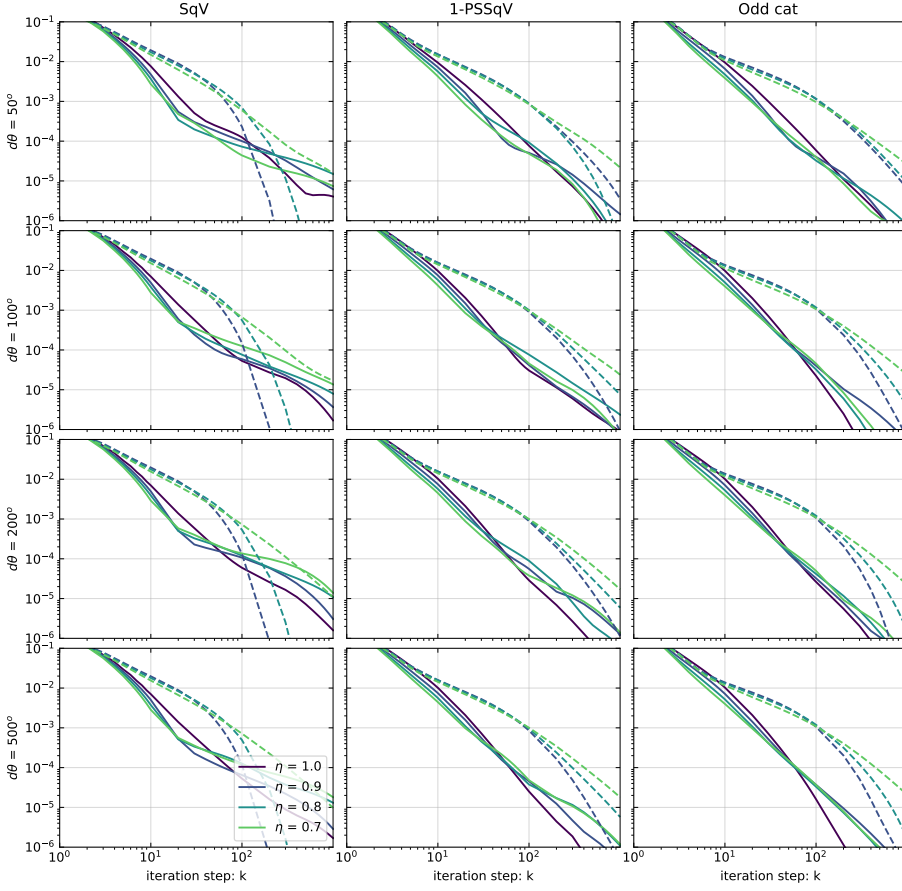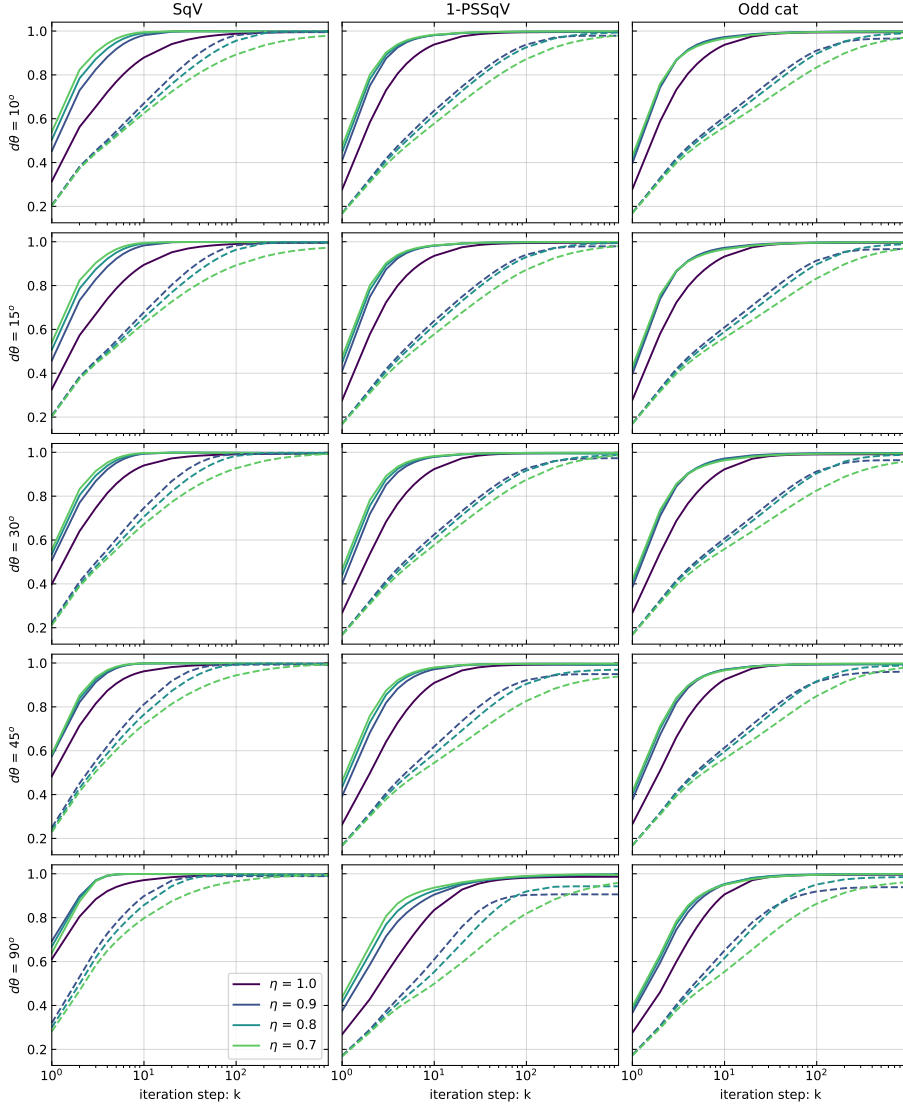
APPENDIX A
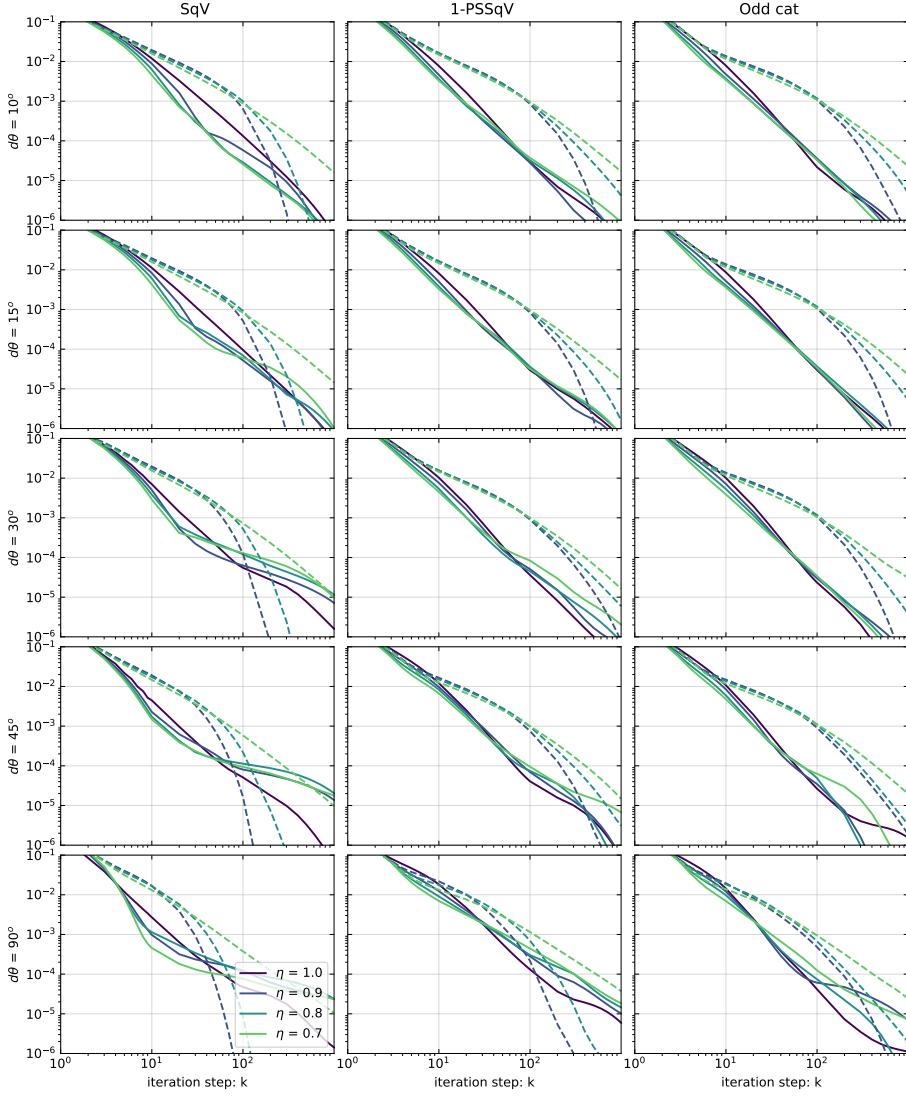
An Appendix

A.1   Homodyne tomography plots
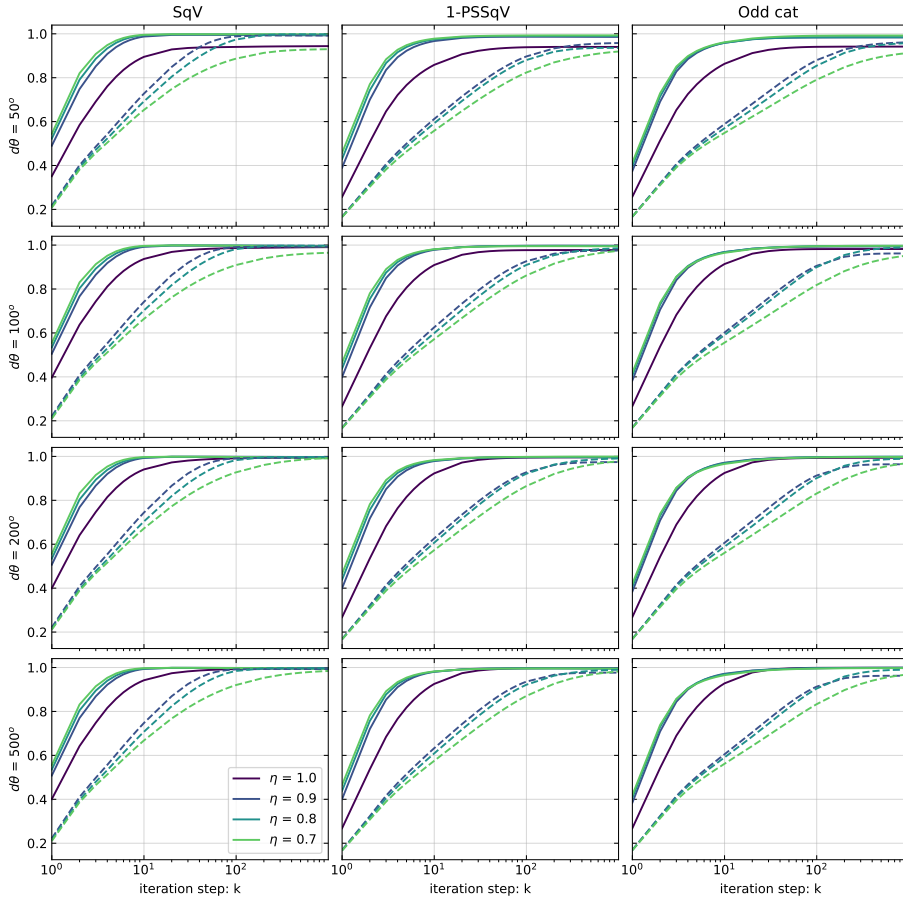
Figure A.1: Homodyne tomography using MaxLik algorithm. Fidelities for various bin ranges. States have average photon number 2 and an azimuthal resolution of 30° is used.

Figure A.2: Homodyne tomography using MaxLik algorithm. Trace distances for various bin ranges. States have average photon number 2 and an azimuthal resolution of 30° is used.

Figure A.3: Homodyne tomography using MaxLik algorithm. Fidelities for various azimuthal resolution $d\theta$. States have average photon number 2 and 200 bins are used.

Figure A.4: Homodyne tomography using MaxLik algorithm. Trace distances for various azimuthal resolution $d\theta$. States have average photon number 2 and 200 bins are used.

Waist size	ω_0	$\sqrt{\lambda z_R / \pi}$
Rayleigh length	z_R	$\pi n \omega_0^2 / \lambda$
Divergence angle	ϕ_R	$\lambda / \pi \omega_0$
Wavenumber	k	$2\pi n / \lambda$
Angular frequency	ν	$2\pi c / \lambda$
Beam width	$\omega(z)$	$\omega_0 \sqrt{1 + (z/z_R)^2}$
Beamfront curvature	$R(z)$	$z \left(1 + (z_R/z)^2\right)$
Gouy phase	$G_{lm}(z)$	$(1 + l + m) \arctan(z/z_R)$
Modematch $1 \leftrightarrow 2$	$\eta_{ol,0}$	$2/(\omega_{0,2}/\omega_{0,1} + \omega_{0,1}/\omega_{0,2})$

Table A.1: Typical parameters of a focused Gaussian beam [54].

A.2   Cavity design guide

A.2.1   Ray transfer matrix analysis

The beam parameter $q(z)$ fully describes a Gaussian beam by its Rayleigh length or waist size

$$q(z) = z + iz_R \;\Leftrightarrow\; \tfrac{1}{q(z)} = \tfrac{1}{R(z)} - \tfrac{i\lambda}{n\pi\omega(z)^2} \tag{A.1}$$
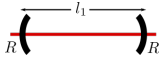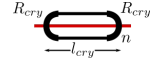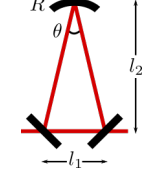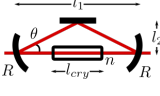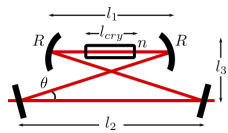
The transformation of a Gaussian beam by a combination linear optical elements is described by the ABCD law

$$q_2 = \frac{Aq_1 + B}{Cq_1 + D} \tag{A.2}$$

where q_1 is the initial Gaussian beam parameter, q_2 is the resulting beam parameter and A,B,C and D are the matrix elements of the ray transfer matrix $M = M_3 M_2 M_1$ describing the sequential transformation of optical elements $1 \rightarrow 2 \rightarrow 3$.

Propagation	d = distance	$M_p = \begin{bmatrix} 1 & d \\ 0 & 1 \end{bmatrix}$
Thin lens	f = focal length	$M_{tl} = \begin{bmatrix} 1 & 0 \\ \frac{-1}{f} & 1 \end{bmatrix}$
Curved mirror	R = mirror curvature $R_e = R\cos\theta$ (tangential plane) $R_e = R/\cos\theta$ (sagittal plane)	$M_m = \begin{bmatrix} 1 & 0 \\ \frac{-2}{R_e} & 1 \end{bmatrix}$
Curved boundary $1 \to 2$	n = refractive index R = boundary curvature	$M_b = \begin{bmatrix} 1 & 0 \\ \frac{n_1-n_2}{Rn_2} & \frac{n_1}{n_1} \end{bmatrix}$

Table A.2: Common ray transfer matrices [54].

Fabry-Perot (FP)		$M = M_p(\frac{l_1}{2})M_m(R)M_p(\frac{l_1}{2})$
Monolithic FP		$M = M_p(\frac{l_{cry}}{2})M_m(R_{cry})M_p(\frac{l_{cry}}{2})$
Triangle		$M = M_p(\frac{l_1}{2} + l_3)M_m(R,\theta)$ $\qquad \times M_p(\frac{l_1}{2} + l_3)$ $l_3 = \sqrt{(\frac{l_1}{2})^2 + l_2^2}, \ \theta = \arctan\frac{2l_2}{l_1}$
Flat triangle w. crystal		$M = M_p(l_3)M_m(R,\theta)$ $\qquad \times M_p(\frac{l_1-l_{cry}}{2})M_b(n,1)M_p(\frac{l_{cry}}{2})$ $l_3 = \sqrt{(\frac{l_1}{2})^2 + l_2^2}, \ \theta = \arctan\frac{2l_2}{l_1}$
Bowtie w. crystal		$M = M_p(l_4 + \frac{l_2}{2})M_m(R,\theta)$ $\qquad \times M_p(\frac{l_1-l_{cry}}{2})M_b(n,1)M_p(\frac{l_{cry}}{2})$ $l_4 = \sqrt{(\frac{l_1+l_2}{2})^2 + l_3^2}, \ \theta = \arctan\frac{2l_3}{l_1+l_2}$

Table A.3: Common optical free-space cavity geometries and the associated ray transfer matrix M used to calculate the resonant mode waist size. Generally M describes the waist to waist transfer, so that if the cavity has has two waists or is symmetric M only describes half a round trip.

Waist-to-waist transfer equations

If we say that both $q_1 = iz_{R,1}$ and $q_2 = iz_{R,2}$ are waists, we can then use the ABCD law to write

$$iz_{R,2} = \frac{iAz_{R,1} + B}{iCz_{R,1} + D} = \frac{i(AD - BC)z_{R,1} + ACz_{R,1}^2 + BD}{(Cz_{R,1})^2 + D^2}$$

which is solved by separating the real and complex part

$$\text{Re}(q_2): \quad 0 = \frac{ACz_{R,1}^2 + BD}{(Cz_{R,1})^2 + D^2} \Leftrightarrow z_{R,1} = \sqrt{\frac{-BD}{AC}} \tag{A.3}$$

$$\text{Im}(q_2): \quad z_{R,2} = \frac{(AD - BC)z_{R,1}}{(Cz_{R,1})^2 + D^2} = \frac{(AD - BC)\sqrt{\frac{-BD}{AC}}}{-C^2\frac{BD}{AC} + D^2}$$

$$= \frac{(AD - BC)\frac{A}{D}\sqrt{\frac{-BD}{AC}}}{-BC + AD} = \sqrt{\frac{-AB}{CD}} \tag{A.4}$$

Here we use that z_R must be real so the terms $-BD/AC$ and $-AB/CD$ are assumed positive. The two equations can then be used directly to obtain the Rayleigh lengths and thereby waist size of any resonant cavity geometry. Since the equations only hold for resonant modes, a geometry resulting in complex Rayleigh lengths corresponds to no resonant mode being supported.

A.2.2 Mechanical designs
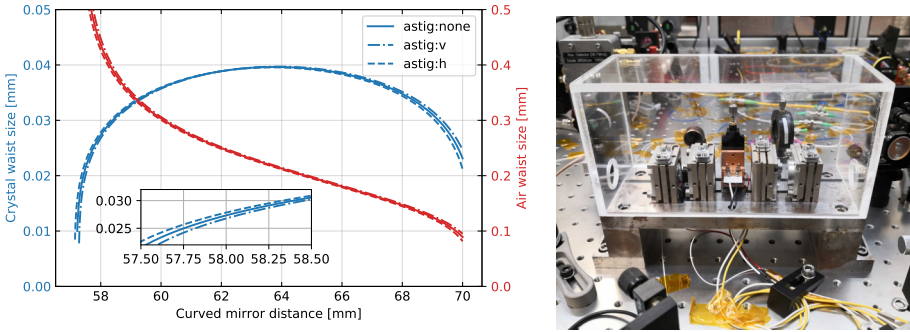
**Figure A.5:** Design consideration of the SHG and OPO cavities.
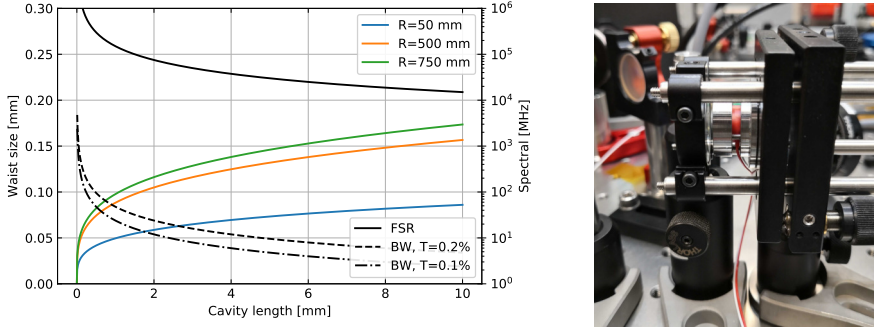
Figure A.6: Design considerations of the FC. resonant mode waist size, bandwidth (BW) and free spectral range (FSR) as function of the cavity length ($l_{cav}/2$) and mirror specifications. Using a cage system, we can easily change the cavity length, but initially choose a cavity length of 2.2 mm with identical 99.8% reflective, 500 mm curved mirrors. This results in a waist size of $\omega_0 = 0.12$ mm and, assuming no additional losses, a finesse of ~ 1600, BW of $\gamma_{FC} \sim 24$ MHz and $\Delta\omega_{FC} \sim 75$ GHz FSR.

A.2.3   Boyd-Kleinmann parameteres

Phase mismatch parameter	σ	$\Delta k z_R$
Focusing strength paramter	χ	$L_{cry}/2z_R$
Focusing position parameter	μ	$(l_{cry} - 2f)/l_{cry}$
Double refraction parameter	β	ρ/δ_0
Absorption parameter	κ	$\alpha_+ z_R$
Phase mismatch	Δk	
Focus position	f	
Double refraction angle	ρ	
Diffraction half-angle	δ_0	
Crystal length	l_{cry}	
Effective nonlinear coefficient	d_{eff}	
Linear absorption coefficient	α_n	
Effective absorption coefficient	$\alpha_\pm$	$\alpha_\omega \pm \alpha_{2\omega}$

**Table A.4:** Overview of parameters used in Boyd-Kleinman theory [57].

A.3   Measurement configurations
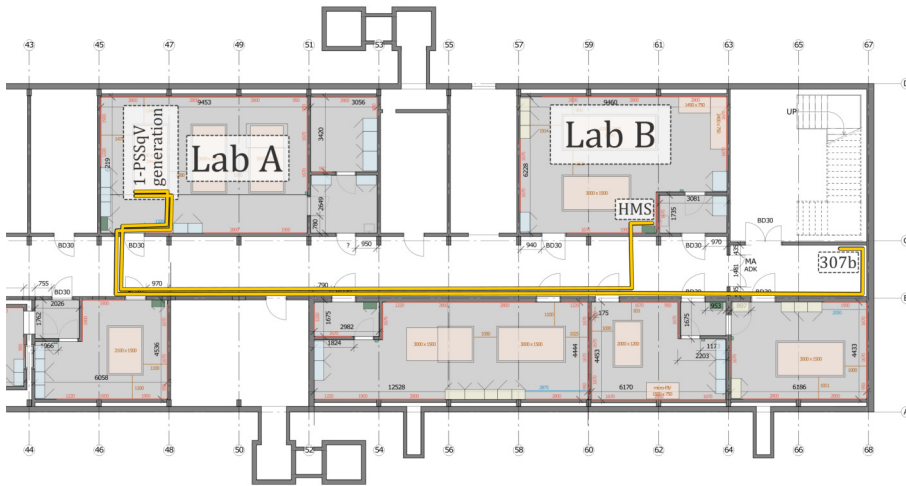
Figure A.7: Map of the laboratory rooms in the basement of building 307 at the DTU campus. The 1-PSSqV state is generated in lab A and is connected to lab B via two 60 m SMF fibers (configuration 2) and to the 307b node of the campus fiber network (G in fig. A.8) via two 70 m SMF fibers (configuration 3).
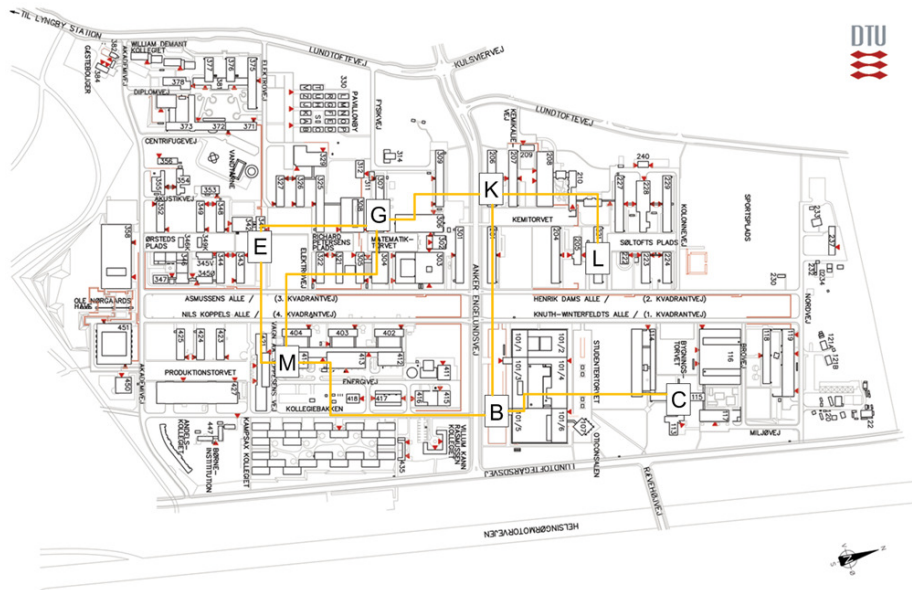
Figure A.8: Map of the DTU fiber network with central nodes shown. For measurement configuration (3) a connection between node G and E was patched up, so that the channel connecting lab A in bld. 307 to lab C in bld. 340 passes through a total of three node cabinets. The total channel length is estimated to be ~ 400 m.
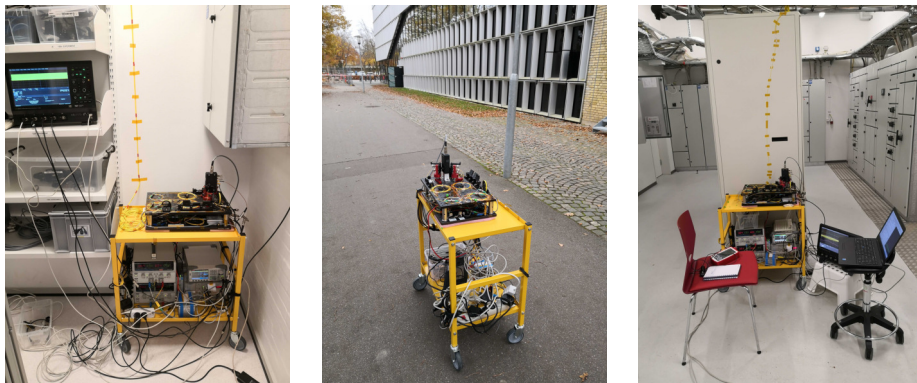
Figure A.9: HMS in lab B (right), on the way to bld. 340 (middle) and inside lab C (left).

A.4 Lab infrastructure

A.4.1 Red Pitaya

In our setup we typically use one RP per lockbox and have modified them in the following way:

- change the output voltage from ± 1 V to $0 - 2$ V and improve the output noise performance by removing resistor R1, R2, R3 and R4 of the output ports [90].

- synchronized the clock of several RP by jumping R23 and R24 (master) and removing R25 and R26 (slave). The clock from the master RP is carried to the slave RP through the GND, CLK+ and CLK- pins of the E2 extension connector. Using this method we have successfully synchronized up to five RP using short unshielded cables as well as synchronizing to RP using a 4 m 2-poled shielded cable.
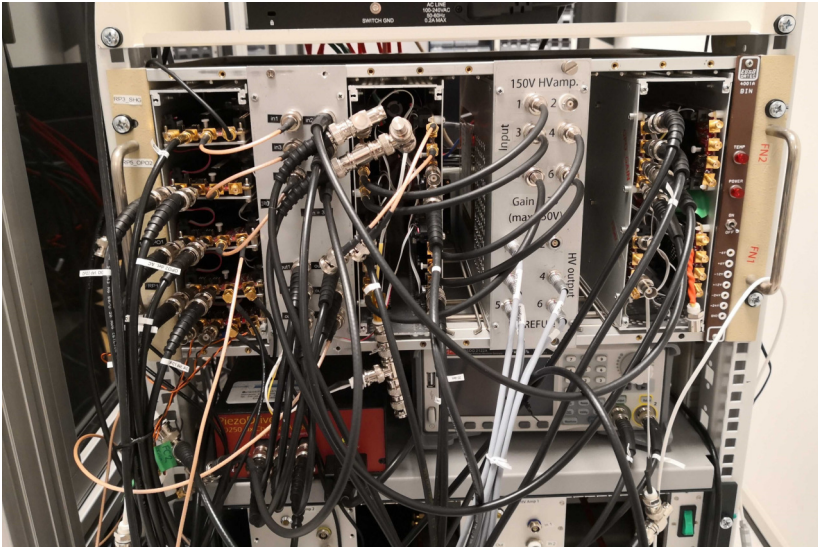
Figure A.10: Red Pitaya rack

A.4.2 Homebuild feedback components
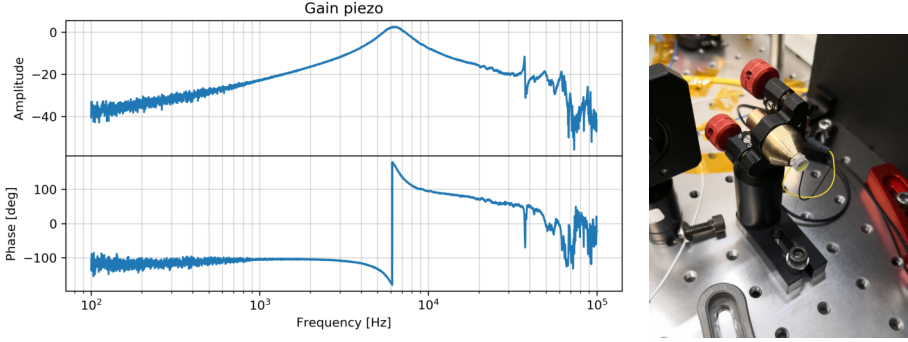
Figure A.11: Network analysis of the small piezo mounted mirror used for probe phase modulation and gain locking.
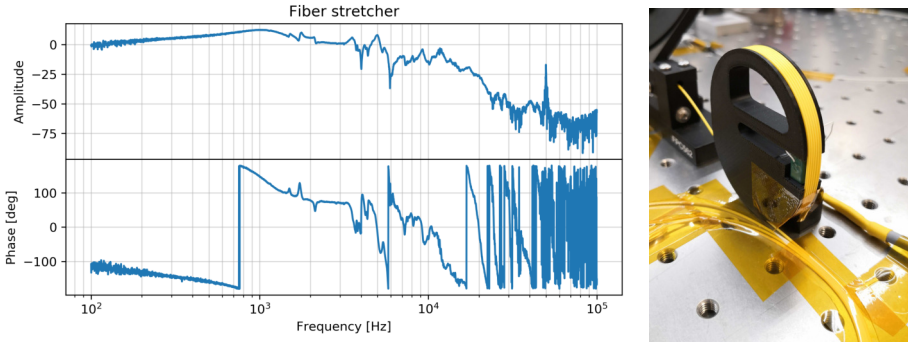
Figure A.12: Network analysis of the 3D printed fiber stretcher used for AC/DC locking of homodyne detection.
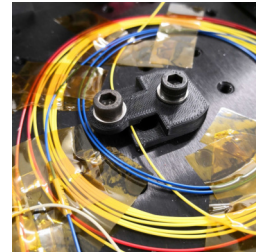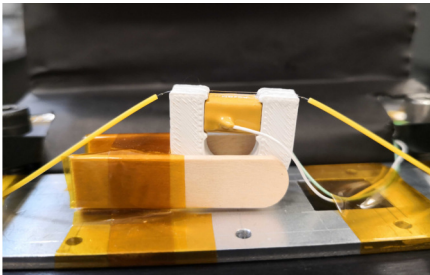
Figure A.13: (**right**) 3D printed fiber modulator. Good LO locking was achieved using 20 kHz modulation with low ringing, but after a few hours of continuous use the piezo broke. (**right**) 3D printed fiber attenuator.

A.5 Supplementary material to Chap. 4

Distributed quantum sensing in a continuous-variable entangled network

Xueshi Guo [1]*, **Casper R. Breum** [1], **Johannes Borregaard**[2], **Shuro Izumi**[1], **Mikkel V. Larsen** [1], **Tobias Gehring** [1], **Matthias Christandl**[2], **Jonas S. Neergaard-Nielsen** [1]* and **Ulrik L. Andersen** [1]*

[1]Center for Macroscopic Quantum States (bigQ), Department of Physics, Technical University of Denmark, Lyngby, Denmark. [2]QMATH, Department of Mathematical Sciences, University of Copenhagen, Copenhagen, Denmark. *e-mail: xguo@fysik.dtu.dk; jsne@fysik.dtu.dk; ulrik.andersen@fysik.dtu.dk

Supplementary material for distributed quantum sensing in a continuous variable entangled network

Xueshi Guo,[1] Casper R. Breum,[1] Johannes Borregaard,[2] Shuro Izumi,[1] Mikkel V. Larsen,[1]
Tobias Gehring,[1] Matthias Christandl,[2] Jonas S. Neergaard-Nielsen,[1] Ulrik L. Andersen[1]

[1] *Center for Macroscopic Quantum States (bigQ), Department of Physics,
Technical University of Denmark, Fysikvej, 2800 Kgs. Lyngby, Denmark*
[2] *QMATH, Department of Mathematical Sciences, University of Copenhagen, Universitetsparken 5, 2100 Copenhagen, Denmark*

(Dated: October 24, 2019)

I. AVERAGED PHASE SHIFT SENSING WITH $\hat{P}_{\mathrm{avg}}$ ESTIMATOR

Our distributed phase sensing scenario is as follows. At each of M spatially separated locations, an optical phase shift ϕ_j occurs. We are interested in estimating the average phase shift $\phi_{\mathrm{avg}} = \frac{1}{M} \sum_{j=1}^{M} \phi_j$. It is straight-forward to generalize to other linear combinations of the phase shifts, but for the sake of demonstrating the power of the entangled approach it suffices to consider the simple average, where the gain is maximum [1]. We consider two different approaches: The *separable* scheme where each phase shift is probed individually by squeezed coherent states, and the *entangled* scheme where the M locations are part of an optical network endowed with a single squeezed coherent state that is distributed among the nodes to serve as an entangled probe. In either case, the phase shifted probes are measured by homodyne detection of their phase quadratures and the results are communicated classically to establish the average.

We furthermore make the following assumptions to simplify the analysis:

1. All the phase shifts are small, giving the small-angle approximation $\sin\phi \approx \phi$.

2. All probes in the separable approach are identical, having real-valued displacement amplitude α_s and squeezing in the phase quadrature with squeezing parameter r_s. That is, the M probes are each in the state $|\psi^{(s)}\rangle = \hat{D}(\alpha_s)\hat{S}(r_s)|0\rangle$, where $\hat{D}(\alpha) = \exp(\alpha\hat{a}^\dagger - \alpha^*\hat{a})$ is the displacement operator and $\hat{S}(r) = \exp(\frac{r}{2}(\hat{a}^{\dagger 2} - \hat{a}^2))$ is the squeezing operator.

3. In the entangled approach, the single initial resource state has real-valued displacement amplitude α_e and phase squeezing with squeezing parameter r_e, that is, it is in the state $|\psi^{(e)}\rangle = \hat{D}(\alpha_e)\hat{S}(r_e)|0\rangle$. This resource is divided evenly through the network to the M nodes.

4. The channel losses, quantified by the efficiency parameter η, are identical for the M channels and they occur entirely prior to the probes reaching the phase samples. In other words, we assume the phase samples themselves and the detection to be lossless. While this assumption is not quite realistic, even in our experiment, it mostly has consequences when keeping track of the number of photons hitting the sample but does not influence the sensitivity as such. In a truly distributed setting, most losses would also happen in the distribution of the resources.

For high-sensitivity estimation of larger phase shifts, these assumptions can still be fulfilled, as long as the local oscillator in the homodyne detector is pre-adjusted to be roughly $90°$ out of phase with the shifted probe. This rough estimation can be done with just a few initial probings [2].

A. General sensitivity for small phase shift

1. Separable scheme

With probe states given as described above, we use the notation defined in Figure 1 to analyse the separable scheme. The phase quadrature of a single mode after channel loss and the phase shift ϕ_j is

$$\hat{p}_j = \left(\sqrt{\eta}\,\hat{x}_{s,j} + \sqrt{1-\eta}\,\hat{x}_{\mathrm{vac},j}\right)\sin\phi_j + \left(\sqrt{\eta}\,\hat{p}_{s,j} + \sqrt{1-\eta}\,\hat{p}_{\mathrm{vac},j}\right)\cos\phi_j, \tag{1}$$
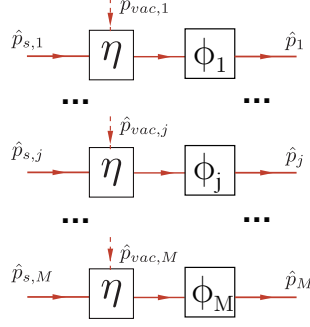
FIG. 1. Phase quadrature notations for analyzing the separable scheme. The amplitude quadrature is defined accordingly. $\hat{p}_{s,1} \ldots \hat{p}_{s,M}$: operator for the initial squeezed states; $\hat{p}_{\text{vac},1} \ldots \hat{p}_{\text{vac},M}$: the vacuum operators induced by loss. η: the overall detection efficiency; $\phi_1 \ldots \phi_M$: the local phase shifts; $\hat{p}_1 \ldots \hat{p}_M$: phase quadrature of a single mode after channel loss and the phase shift.

where $\hat{x}_{s,j}, \hat{p}_{s,j}$ are the quadrature operators of the initial squeezed states with mean values $\langle \hat{x}_{s,j} \rangle = \sqrt{2}\alpha_s$, $\langle \hat{p}_{s,j} \rangle = 0$ and variances $\langle \Delta \hat{x}_{s,j}^2 \rangle = \frac{1}{2}e^{2r_s}$, $\langle \Delta \hat{p}_{s,j}^2 \rangle = \frac{1}{2}e^{-2r_s}$, while $\hat{x}_{\text{vac},j}$, $\hat{p}_{\text{vac},j}$ are vacuum mode operators admixed through the losses. The expectation value of the rotated phase quadrature is

$$\langle \hat{p}_j \rangle = \sqrt{\eta} \, \langle \hat{x}_{s,j} \rangle \sin \phi_j = \sqrt{2\eta}\alpha_s \sin \phi_j \approx \sqrt{2\eta}\alpha_s \phi_j. \tag{2}$$

The phase shift can thus be directly estimated from the measured $\hat{p}_j$ values. The average phase shift of M modes, $\phi_{\text{avg}} = \frac{1}{M} \sum_{j=1}^{M} \phi_j$, can then be estimated with the estimator $\hat{P}_{\text{avg}} = \frac{1}{M} \sum_{j=1}^{M} \hat{p}_j$:

$$\langle \hat{P}_{\text{avg}} \rangle \approx \sqrt{2\eta}\alpha_s \phi_{\text{avg}}. \tag{3}$$

The sensitivity of the estimation is defined as the standard deviation which, from standard error propagation analysis, is given by

$$\sigma_s = \frac{\sqrt{\langle \Delta \hat{P}_{\text{avg}}^2 \rangle}}{\left| \partial \langle \hat{P}_{\text{avg}} \rangle / \partial \phi_{\text{avg}} \right|}. \tag{4}$$

The slope of $\hat{P}_{\text{avg}}$ versus ϕ_{avg} is

$$\partial \langle \hat{P}_{\text{avg}} \rangle / \partial \phi_{\text{avg}} \approx \sqrt{2\eta}\alpha_s, \tag{5}$$

and its variance is

$$\langle \Delta \hat{P}_{\text{avg}}^2 \rangle = \frac{1}{M^2} \left\langle \Delta \left(\sum_{j=1}^{M} \hat{p}_j \right)^2 \right\rangle = \frac{1}{M^2} \sum_{j=1}^{M} \langle \Delta \hat{p}_j^2 \rangle \tag{6}$$

$$= \frac{1}{M^2} \sum_{j=1}^{M} \left(\sin^2 \phi_j (\eta \langle \Delta \hat{x}_{s,j}^2 \rangle + (1-\eta) \langle \Delta \hat{x}_{\text{vac},j}^2 \rangle) + \cos^2 \phi_j (\eta \langle \Delta \hat{p}_{s,j}^2 \rangle + (1-\eta) \langle \Delta \hat{p}_{\text{vac},j}^2 \rangle) \right) \tag{7}$$

$$= \frac{1}{M^2} \sum_{j=1}^{M} \left(\frac{\eta e^{2r_s}}{2} \sin^2 \phi_j + \frac{\eta e^{-2r_s}}{2} \cos^2 \phi_j + \frac{1-\eta}{2} \right). \tag{8}$$

The second equality comes from the fact that in the separable approach there are no correlations between the modes. Under a stronger bound on the magnitude of the phase shifts, $\phi_j \ll \sqrt{\langle \Delta \hat{p}_{s,j}^2 \rangle / \langle \Delta \hat{x}_{s,j}^2 \rangle}$, this expression reduces to

$$\langle \Delta \hat{P}_{\text{avg}}^2 \rangle \approx \frac{1}{M} \left(\eta \langle \Delta \hat{p}_{s,j}^2 \rangle + \frac{1-\eta}{2} \right) = \frac{\eta e^{-2r_s} + 1 - \eta}{2M}. \tag{9}$$

Hence, the sensitivity is

$$\sigma_s = \frac{\sqrt{e^{-2r_s} + 1/\eta - 1}}{2\alpha_s \sqrt{M}}. \tag{10}$$

The average number of photons hitting each sample is

$$N_s = N_{s,\text{coh}} + N_{s,\text{sqz}} = \eta(\alpha_s^2 + \sinh^2 r_s). \tag{11}$$
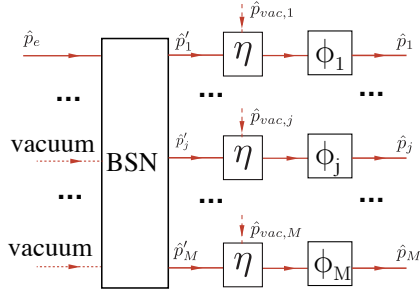
FIG. 2. Phase quadrature notations for analyzing the entangled scheme. The amplitude quadrature is defined accordingly. BSN: beam-splitter network with M inputs and outputs; $\hat{p}_e$: the only non-vacuum input of the BSN; $\hat{p}_1' \ldots \hat{p}_M'$: the evenly split M output of the BSN. All the other notations are the same as Figure 1.

2. Entangled scheme

With entangled probes (the notation used in our analysis is summarized in Figure 2), we use the same estimator, $\hat{P}_{\text{avg}}$. The individual modes that combine to form the average are, however, now related through the distributed single initial resource $\hat{p}_e$:

$$\hat{p}_j = \left(\sqrt{\eta} \, \hat{x}_j' + \sqrt{1-\eta} \, \hat{x}_{\text{vac},j} \right) \sin \phi_j + \left(\sqrt{\eta} \, \hat{p}_j' + \sqrt{1-\eta} \, \hat{p}_{\text{vac},j} \right) \cos \phi_j, \tag{12}$$

where the primed mode operators are obtained after symmetric distribution in the beam-splitter network, that is,

$$\hat{x}_e = \frac{1}{\sqrt{M}} \sum_{j=1}^{M} \hat{x}_j' \,, \quad \hat{p}_e = \frac{1}{\sqrt{M}} \sum_{j=1}^{M} \hat{p}_j'. \tag{13}$$

The mean value of the estimator is

$$\langle \hat{P}_{\text{avg}} \rangle = \frac{1}{M} \sum_{j=1}^{M} \langle \hat{p}_j \rangle \approx \frac{\sqrt{\eta}}{M} \sum_{j=1}^{M} \langle \hat{x}_j' \rangle \phi_j = \sqrt{\frac{2\eta}{M}} \alpha_e \phi_{\text{avg}}. \tag{14}$$

The variance is

$$
\begin{aligned}
\langle \Delta \hat{P}_{\text{avg}}^2 \rangle &= \frac{1}{M^2} \left\langle \Delta \left(\sum_{j=1}^{M} \hat{p}_j \right)^2 \right\rangle \\
&\approx \frac{\eta}{M^2} \left\langle \Delta \left(\sum_{j=1}^{M} \hat{x}'_j \phi_j \right)^2 \right\rangle + \frac{\eta}{M^2} \left\langle \Delta \left(\sum_{j=1}^{M} \hat{p}'_j \right)^2 \right\rangle + \frac{1-\eta}{M^2} \left\langle \Delta \left(\sum_{j=1}^{M} \hat{p}_{\text{vac},j} \right)^2 \right\rangle \\
&\approx \frac{\eta}{M^2} \left\langle \Delta \left(\sum_{j=1}^{M} \hat{p}'_j \right)^2 \right\rangle + \frac{1-\eta}{M^2} \sum_{j=1}^{M} \langle \hat{p}_{\text{vac},j}^2 \rangle \\
&= \frac{\eta}{M^2} M \langle \Delta \hat{p}_e^2 \rangle + \frac{1-\eta}{M^2} \sum_{j=1}^{M} \langle \hat{p}_{\text{vac},j}^2 \rangle \\
&= \frac{\eta e^{-2r_e} + 1 - \eta}{2M}.
\end{aligned} \tag{15}
$$

In the second line, we made use of the fact that there are no correlations between $\hat{x}$ and $\hat{p}$ quadratures for the given probe state in our entangled scheme as well as the small angle approximation $\cos(\phi_j) \approx 1$, $\sin(\phi_j) \approx \phi_j$. In the third line, we further tightened the small angle approximation by taking a $\tilde{\phi}$ such that for all j, $|\phi_j| < \tilde{\phi}$ and assuming

$$
\begin{aligned}
\tilde{\phi}^2 \left\langle \Delta \left(\sum_{j=1}^{M} \hat{x}'_j \right)^2 \right\rangle &\ll \left\langle \Delta \left(\sum_{j=1}^{M} \hat{p}'_j \right)^2 \right\rangle \\
\Rightarrow \quad \tilde{\phi}^2 &\ll \frac{\langle \Delta \hat{p}_e^2 \rangle}{\langle \Delta \hat{x}_e^2 \rangle} \\
\Rightarrow \quad \tilde{\phi} &\ll e^{-2r_e}.
\end{aligned} \tag{16}
$$

This approximation gives a sensitivity for the entangled approach of

$$
\sigma_e = \frac{\sqrt{\langle \Delta \hat{P}_{\text{avg}}^2 \rangle}}{\left| \partial \langle \hat{P}_{\text{avg}} \rangle / \partial \phi_{\text{avg}} \right|} = \frac{\sqrt{e^{-2r_e} + 1/\eta - 1}}{2\alpha_e}. \tag{17}
$$

Note that this, in contrast with the separable approach, does not depend on the number of modes M. The sensitivity is therefore the same as the sensitivity for a single mode with the same resource state - but in the single mode case the sample would of course be exposed to M times as many photons. The average number of photons hitting each sample in the distributed, entangled scheme is

$$
N_e = N_{e,\text{coh}} + N_{e,\text{sqz}} = \frac{\eta}{M}(\alpha_e^2 + \sinh^2 r_e). \tag{18}
$$

B. Optimized parameters and sensitivities

1. Entangled scheme

With the sensitivities given by eqs. (10) and (17), we wish to find the values for the displacement amplitudes and squeezing parameters that optimize the sensitivity for a fixed photon number on the sample. This problem can be solved with Lagrangian multipliers, using the constraint $N_{s,e} - N = 0$, where N is the photon number to be held fixed during optimization. The total photon number of the resource state(s) before loss is then $N_{\text{tot}} = MN/\eta$.

The Lagrange function for the entangled scheme is

$$\mathcal{L}_e(\alpha_e, r_e, \lambda) = \sigma_e + \lambda(N_e - N) \tag{19}$$

$$= \frac{\sqrt{e^{-2r_e} + 1/\eta - 1}}{2\alpha_e} + \lambda \frac{\eta}{M}(\alpha_e^2 + \sinh^2 r_e) - \lambda N, \tag{20}$$

and the equations for the stationary point of the Lagrangian become

$$0 = \nabla_{\alpha_e} \mathcal{L}_e = -\frac{\sqrt{e^{-2r} + 1/\eta - 1}}{2\alpha_e^2} + \frac{2\lambda\eta\alpha_e}{M}, \tag{21}$$

$$0 = \nabla_{r_e} \mathcal{L}_e = -\frac{e^{-2r_e}}{2\alpha_e\sqrt{e^{-2r_e} + 1/\eta - 1}} + \frac{2\lambda\eta\cosh r \sinh r_e}{M}, \tag{22}$$

$$0 = \nabla_\lambda \mathcal{L}_e = \frac{\eta}{M}(\alpha_e^2 + \sinh^2 r_e) - N. \tag{23}$$

After some manipulation, the solutions can be expressed as

$$e^{2r_e} = \frac{\Lambda_M - \eta}{1 - \eta}, \tag{24}$$

$$\alpha_e^2 = N_{\text{tot}} - \sinh^2 r_e = N_{\text{tot}} - \frac{e^{2r_e} + e^{-2r_e} - 2}{4} = \frac{MN}{\eta} - \frac{(\Lambda_M - 1)^2}{4(1 - \eta)(\Lambda_M - \eta)}, \tag{25}$$

with $\Lambda_M = \sqrt{1 + 4MN(1 - \eta)}$. The optimal photon number ratio is

$$\mu_e = \frac{N_{e,\text{sqz}}}{N} = \frac{\sinh^2 r_e}{N_{\text{tot}}} = \frac{\eta(\Lambda_M - 1)^2}{4MN(1 - \eta)(\Lambda_M - \eta)}, \tag{26}$$

and the optimal sensitivity obtained with these parameters becomes

$$\sigma_e^{\text{opt}} = \frac{1}{2MN}\sqrt{\frac{MN(1 - \eta) + \eta(\Lambda_M + 1)/2}{1 + \eta/(MN)}}, \tag{27}$$

which for $\eta = 1$ reduces to $\sigma_e^{\text{opt}}(\eta = 1) = \frac{1}{2MN}\sqrt{\frac{MN}{MN+1}}$. This sensitivity exhibits Heisenberg scaling in both photon number (due to the squeezing) and mode number (due to the entanglement).

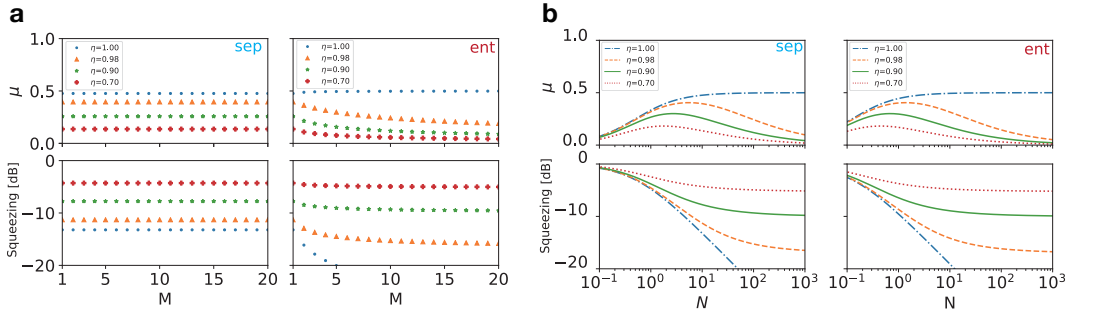

FIG. 3. **a** and **b**: Optimized squeezed photon number ratio μ and squeezing degrees $\eta e^{-2r} + (1 - \eta)$ for the Fig. 1**c** and 1**d** in the main text, respectively. Sep, the separable approach; Ent, the entangled approach.

2. Separable scheme

Doing the same derivation for the separable scheme, that is, starting from the Lagrange function $\mathcal{L}_s(\alpha_s, r_s, \tilde{\lambda}) = \sigma_s + \tilde{\lambda}(N_s - N)$, results in the following optimal parameters for squeezing and displacement:

$$e^{2r_s} = \frac{\Lambda_1 - \eta}{1 - \eta}, \tag{28}$$

$$\alpha_s^2 = \frac{N_{\text{tot}}}{M} - \sinh^2 r_s = \frac{N}{\eta} - \frac{(\Lambda_1 - 1)^2}{4(1 - \eta)(\Lambda_1 - \eta)}, \tag{29}$$

with $\Lambda_1 = \sqrt{1 + 4N(1 - \eta)}$, and a corresponding photon number ratio

$$\mu_s = \frac{N_{s,\text{sqz}}}{N} = \frac{M \sinh^2 r_s}{N_{\text{tot}}} = \frac{\eta(\Lambda_1 - 1)^2}{4N(1 - \eta)(\Lambda_1 - \eta)}. \tag{30}$$

Finally, the optimal sensitivity becomes

$$\sigma_s^{\text{opt}} = \frac{1}{2\sqrt{MN}} \sqrt{\frac{N(1 - \eta) + \eta(\Lambda_1 + 1)/2}{1 + \eta/N}}, \tag{31}$$

which for $\eta = 1$ reduces to $\sigma_s^{\text{opt}}(\eta = 1) = \frac{1}{2\sqrt{MN}} \sqrt{\frac{N}{N+1}}$, thus no longer showing Heisenberg scaling in the mode number. The result enable us to obtain the simulation result in Fig 1c and 1d in the main text, and the optimal μ and corresponding squeezing rated need to get the optimal μ is shown in Fig. 3.

II. PREPARATION OF ENTANGLED PROBES

The entangled probes are prepared in two steps. First, we generate a squeezed coherent state, denoted as the squeezed probe (SP), by an optical parametric oscillator (OPO). Second, we send the SP through a beam-splitter network (BSN) to generate 4 entangled probes. We define the mode of the SP to be a narrow sideband at 3 MHz, since this is region where we have high squeezing quality.

A. Generation of squeezed probes with OPO

The laser source for the experiment is an amplified NKT Photonics X-15 fibre laser operating at 1550 nm. Most of the light is used for pumping a second harmonic generation (SHG) cavity (same design as the OPO described below) to produce 775 nm light to act as the OPO pump. The rest is used for the local oscillator and the probe and lock beams. As shown in Fig. 4, we use a bow-tie shaped OPO with a periodically poled potassium titanyl phosphate (PPKTP) crystal to generate the SP by type-0 parametric down conversion. The bandwidth of the cavity is 8.0 MHz half width half maximum (HWHM) and the OPO pump power threshold is 850 mW. The 775 nm pump, which for the measurements presented here varied between 150 mW and 350 mW, is coupled through the dichroic curved cavity mirrors and dumped after passing the crystal. A 3.6 mW coherent beam at 1550 nm, weakly phase-modulated by an electro-optic modulator (EOM) at 3 MHz and 28.7 MHz, is coupled into the OPO in the counter-propagating direction through a high reflectivity mirror (HR) with a transmittance of about 100 ppm. This beam is used to lock the cavity by the Pound–Drever–Hall technique with the 28.7 MHz side band and the resonant detector D1. All cavity and phase locks in the experiment are handled by Red Pitaya FPGA boards running the PyRPL lockbox software [3].

The reflection from the HR mirror is re-coupled into the forward-propagating mode of the OPO with a 0° mirror to serve as the carrier of the sideband mode that defines our probe state. A variable attenuator (Att.) is inserted to control the optical power. In the OPO, the forward-propagating beam is squeezed by the parametric process and coupled out through a 10% transmittive out coupling mirror (light gray in Fig. 4). A half-wave plate ($\lambda/2$) and a polarization beam-splitter (PBS) is used to tap around 1% of the OPO output towards detector D2 to lock the phase between the carrier and the pump for de-amplification. As a result, the carrier is squeezed in the amplitude quadrature, leading to squeezing of the phase quadrature of the probe in the 3 MHz modulated sideband frequency mode since the sideband is encoded by phase modulation.
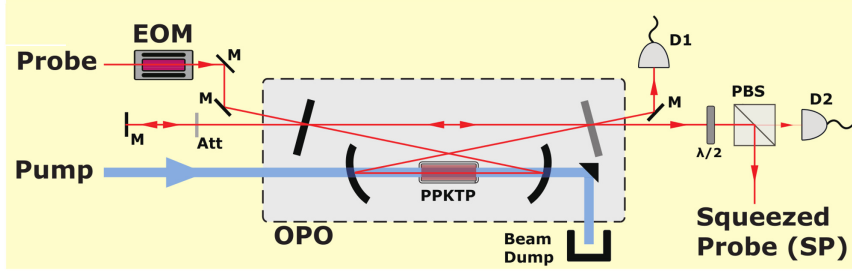
FIG. 4. Squeezed probe (SP) preparation with OPO. M, high reflectively mirror; EOM, electro-optic modulator; Att, attenuator; D1, resonant detector for cavity lock; D2, high gain detector for OPO gain lock.

B. Generation and detection of entangled probes

The detailed experimental setup is shown in Fig. 5. It is essentially a multi-port version of a squeezed-light-enhanced polarization interferometer [4]. We create four entangled probes by sending the squeezed probe, SP, through a BSN consisting of three 50:50 beam-splitters. Prior to this, the SP is spatially combined on a PBS with a strong beam (LO) which will act as the local oscillator for all four modes. The LO phase is locked to either the $\hat{p}$ or $\hat{x}$ quadrature of the SP by tapping $\sim 1\%$ towards a polarization-based homodyne detection setup, the output of which is used to control a piezo-mounted mirror in the LO path. In each of the four modes, the phase between LO and SP can be further controlled by a $\lambda/4$ and a $\lambda/2$ wave plate. The $\lambda/4$ plates change the LO and SP into left-hand and right-hand circular polarization, respectively. The $\lambda/2$ plates introduce phase shifts between SP and LO and play two roles: First, they are used to synchronize the phases for the entangled probes by compensating the phase difference induced by 50:50 beam splitters. Second, they are used to simulate the phase samples, that is, the imposed phases $\phi_1, \ldots, \phi_4$. For details, see section III A. Finally, the four outputs are measured on homodyne detectors.
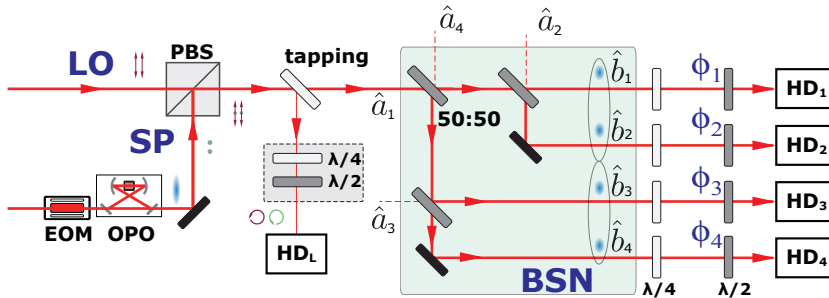
FIG. 5. Detailed experimental setup and the input-output relationship of the beam splitter network (BSN). The input modes $\hat{a}_1$ to $\hat{a}_4$ with s-polarization are transferred into the output modes $\hat{b}_1$ to $\hat{b}_4$. Here, only $\hat{a}_1$ is a squeezed coherent state operator. $\hat{a}_2$ to $\hat{a}_4$ are vacuum operators. By tuning the wave plates at each output of the BSN, $\hat{b}_1$ to $\hat{b}_4$ are set to circular polarization.

1. Homodyne detection and data acquisition

All five homodyne detection setups use the same scheme, illustrated in Fig. 6a. The circularly polarized SP and LO interfere after the PBS. The optical power of the LO is about 3 mW on each HD and it detects a SP of about 10 nW. The output of the detector is electronically split into AC and DC parts with a bias-tee of about 100 kHz. The AC signal, V_{ac}, is used for phase sensing. It includes the 3 MHz side-band, but filters out the carrier at DC and the side-band for cavity locking at 28.7 MHz with a low pass filter at around 14 MHz. The DC signal, V_{dc}, detects the carrier. It is used for phase locking and phase calibration (see section III B).

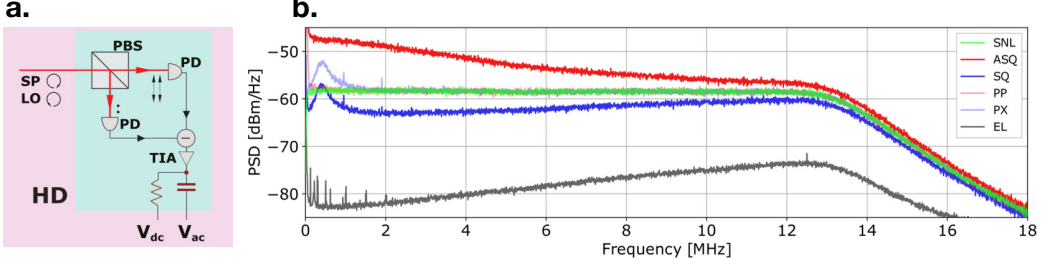FIG. 6. **a.** The circular polarized SP and local oscillator (LO) are projected into p- or s-polarization by a PBS, and detected with a balanced photo-detector. The output voltage of the detector photo diodes is separated into DC–100 kHz output V_{dc} and 100 kHz–14 MHz output V_{ac}. PD, photo diode; TIA, trans-impedance amplifier. **b.** Power spectral densities (PSDs). SNL, shot-noise limit; ASQ, anti-squeezing; SQ, squeezing; PX and PP, probe noise in X and P quadrature respectively, measured by blocking pump; EL, electronic noise of the data acquisition system, measured by blocking both SP and the LO.

The V_{ac} outputs of HD1 to HD4 are sent to a 4-channel oscilloscope (LeCroy HDO6034), which acquires time-voltage traces of 200 μs with a 50 MHz sampling rate. The power spectral densities (PSDs) of the individual HD outputs and the averaged output is obtained by Fast Fourier Transform (FFT) on a computer. Fig. 6b shows PSDs for the averaged voltage of the 4 HDs in different experimental conditions with no modulation from the EOM. All the PSDs in Fig. 6b are the averaged result of 400 oscilloscope measurements. To show the signal-to-noise ratio of the data acquisition system, we measure the PSDs of the shot noise level (SNL, measured when SP is blocked) and electronic noise (EL, measured when both SP and LO are blocked). The result is shown in green and dark grey traces in Fig. 6b. We see that the electronic noise clearance is about 23 dB at the 3 MHz side band, which corresponds to about 0.5% effective loss in detection efficiency. We will discuss the other PSDs shown in Fig. 6b in the following subsection.

2. Input-output relations of the BSN

The BSN we use in the experiment is shown in Figure 5. The only non-vacuum input mode $\hat{a}_1$ is the SP, whose mode operator is $\hat{a}_1 = \hat{S}^\dagger(r)\hat{a}\hat{S}(r) + \alpha$ in the Heisenberg picture, with $\hat{a}$ being the annihilation operator of the OPO input at 3 MHz and the real-valued α being the effective coherent excitation of the mode after modulation by the EOM and de-amplification in the OPO. All the other input modes $\hat{a}_2$, $\hat{a}_3$ and $\hat{a}_4$ are vacuum modes. The output modes of the BSN, $\hat{b}_j$ can be explicitly written as:

$$
\begin{aligned}
\hat{b}_1 &= \frac{1}{2}\sqrt{\eta}(\hat{a}_1 - i\hat{a}_4 + \sqrt{2}i\hat{a}_2) + \sqrt{1-\eta}\hat{a}_{vac,1} \\
\hat{b}_2 &= \frac{1}{2}\sqrt{\eta}(\hat{a}_1 - i\hat{a}_4 - \sqrt{2}i\hat{a}_2) + \sqrt{1-\eta}\hat{a}_{vac,2} \\
\hat{b}_3 &= \frac{1}{2}\sqrt{\eta}(\hat{a}_1 + i\hat{a}_4 + \sqrt{2}i\hat{a}_3) + \sqrt{1-\eta}\hat{a}_{vac,3} \\
\hat{b}_4 &= \frac{1}{2}\sqrt{\eta}(\hat{a}_1 + i\hat{a}_4 - \sqrt{2}i\hat{a}_3) + \sqrt{1-\eta}\hat{a}_{vac,4}.
\end{aligned}
\tag{32}
$$

Here we have introduced an identical overall efficiency η and vacuum mode operator $\hat{a}_{vac,j}$ for $j = 1 \dots 4$. Although the various inefficiencies occur at different points in the experiment, for simplicity we have assumed (as in section I) that they all occur after the distribution of the probes in the BSN and that they are identical for the four channels. Experimentally, we use eight variable irises before the PDs of all four HDs to equalize the overall detection efficiency.

3. Overall detection efficiency estimation

The loss budget of our experiment setup is as follows: the escape efficiency of the OPO $\sim 95\%$; the quantum efficiency of the photo diodes in HD $\sim 98\%$; the imperfection of the mode matching between SP and LO $\sim 90\%$; the

electronic noise of the homodyne detection $\sim 99\%$; the efficiency introduced by tapping for phase locking $\sim 97\%$ and the efficiency of all optics between OPO output and the PD of the HD $\sim 92\%$. The loss budget of the experiment system gives an estimation of the overall detection efficiency of $\eta \sim 74\%$.

We also estimate the overall detection efficiency by measuring the squeezing/anti-squeezing degrees (notated with v_{sq}^2 and v_{asq}^2) for the entangled approach at 3 MHz. Since

$$
\begin{aligned}
v_{sq}^2 &= \eta e^{-2r_e} + (1 - \eta) \\
v_{asq}^2 &= \eta e^{2r_e} + (1 - \eta),
\end{aligned}
\tag{33}
$$

we can calculate η and r_e with measured v_{sq}^2 and v_{asq}^2. The overall efficiency estimated with 5 different pump powers to the OPO is $\eta = 73.5\% \pm 1.5\%$. This result coincide with the loss budget estimation, and we use this result to theoretically calculate the sensitivity.

For the separable approach, where the BSN is removed, the overall efficiency is $\sim 1.5\%$ higher. However, we compensate this by tapping more to the lock detector D2 in Figure 4 so the separable approach has similar efficiency to that of the entangled approach.

4. Entanglement characterization of the probes

The squeezing degree for each individual output mode will not be better than 3/4 shot noise due to the splitting of the SP in the BSN. However, the squeezing of SP is converted into entanglement between all the probes. By joint measurement of the 4 probes (simply averaging the voltage from the four HDs), we can recover the squeezing degree of the SP: From Eq. (32), the joint measurement recovering the squeezing of SP is simply the sum of the four HD_{1-4} outputs. The recovered squeezed and anti-squeezed quadratures are shown as SQ (blue) and ASQ (red) in Fig. 6b. We see the joint measurement gives about 4.8 dB of squeezing at the 3 MHz side band frequency. The additional noise seen below 2 MHz is due to technical noise from our laser. As a calibration of the noise of the probe before the parametric process, we measure the PSDs of $\hat{X}$ and $\hat{P}$ quadrature by blocking the pump of our OPO, and the result is shown with PX (light blue) and PP (light red) in Fig. 6b (noting that here we refer to the amplitude/phase quadrature of the carrier of the SP since there is no side-band). We see the technical noise of both $\hat{X}$ and $\hat{P}$ quadrature decreases as the frequency increases and overlap with the SNL when the frequency is above 1.8 MHz. Therefore, in our estimation of the overall detection efficiency at the side band frequency (3 MHz), we ignore contributions from technical noise of the laser.
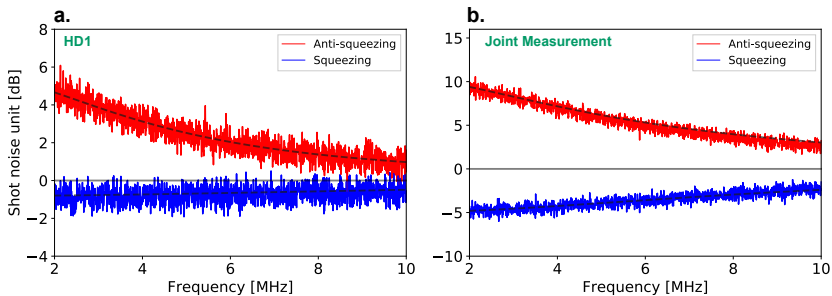
FIG. 7. **a.** Squeezing and anti-squeezing spectra for a single distributed spatial mode obtained from HD_1. **b.** Squeezing and anti-squeezing spectra from joint measurement. Dashed lines: spectra predicted by theory.

With the measurement described in Fig. 6b, we can get the squeezing/anti-squeezing degree in SNL units. Fig. 7a and b shows the squeezing and anti-squeezing of an individual channel (HD1) and that from the joint measurement, respectively. The dashed lines show the squeezing and anti-squeezing predicted by [5]

$$
S^{\pm}(f) = 1 \pm \frac{4\eta \sqrt{P/P_{th}}}{(1 \mp \sqrt{P/P_{th}})^2 + (f/f_{cav})^2},
\tag{34}
$$

where $S^-(f)$ and $S^+(f)$ denotes the squeezing and anti-squeezing spectrum, $\eta = 0.735$ is the estimated overall detection efficiency, $f_{cav} = 8.0$ MHz is the HWHM of the OPO cavity and $P_{th} = 850$ mW is the threshold of the

OPO. In this measurement, $P = 300$ mW pump power is used. Here both f_{cav} and P_{th} are obtained from independent measurements.

We quantitatively verify the entanglement of the probes by reconstructing the covariance matrix of the 4 modes. As we do not expect correlations between $\hat{x}$ and $\hat{p}$ quadratures, we only experimentally reconstruct $M_x = \text{Cov}(\hat{x}_j, \hat{x}_k)$ and $M_p = \text{Cov}(\hat{p}_j, \hat{p}_k)$ for $j, k = 1$ to 4 at around 3 MHz. After balancing the length of cables from HD_{1-4} to the oscilloscope, we digitally filter the recorded traces by a 50 kHz band pass filter centered around 3 MHz, and measure M_x and M_p, respectively. The covariance matrices in shot noise units from the average of 400 oscilloscope measurements are:

$$M_x = \begin{pmatrix} 0.83 & -0.18 & -0.17 & -0.19 \\ - & 0.84 & -0.16 & -0.18 \\ - & - & 0.83 & -0.18 \\ - & - & - & 0.82 \end{pmatrix} \quad M_p = \begin{pmatrix} 3.0 & 1.9 & 1.9 & 2.0 \\ - & 2.8 & 1.8 & 1.9 \\ - & - & 2.8 & 1.9 \\ - & - & - & 3.0 \end{pmatrix}, \tag{35}$$

where symmetric elements are not shown. We show the entanglement property of the probes by calculating the logarithmic negativity $\mathcal{N}(\hat{\rho})$ between them, where $\mathcal{N}(\hat{\rho}) > 0$ is a sufficient condition for entanglement [6]. For a Gaussian state this can be obtained through the symplectic eigenvalues of the partially transposed covariance matrix, so that $\mathcal{N}(\rho) = \sum_k f(\tilde{v}_k)$, where $\tilde{v}_k$ are the symplectic eigenvalues and $f(x) = -\log_2(x)$ for $x < 1$ and 0 otherwise. By constructing the full $M_{x,p}$ covariance matrix from M_x and M_p, we find that for any two, three or four modes the value of $\mathcal{N}(\hat{\rho})$ is within the range of 0.20 ± 0.02, 0.33 ± 0.02 and 0.51 ± 0.02 respectively, confirming the presence of quadrature entanglement across all mode combinations.

III.   PHASE CONTROL AND CALIBRATION

In this section we first calculate the interference at the two photo diodes of the HD in Fig. 6. The result shows that the phase between SP and LO can be controlled by rotating the $\lambda/2$ wave plates. After that, we describe the phase calibration procedure and result in our experiment. With the phase calibration result, we can control the phase ϕ_j for $j = 1 \ldots 4$ (and therefore ϕ_{avg}) by rotating the $\lambda/2$ wave plates to a specific position.

A.   Phase control with $\lambda/2$ wave plates

The LO with p polarization and OPO output with s polarization are combined by the PBS in Fig. 5, and the Jones vector after the PBS is

$$J_{in} = \begin{bmatrix} E_{LO} \cdot e^{-i\phi_{LO}} \\ E_{SP} \cdot e^{-i\phi_{SP}} \end{bmatrix}, \tag{36}$$

where $E_{LO} \cdot e^{-i\phi_{LO}}$ is the LO and $E_{SP} \cdot e^{-i\phi_{SP}}$ is the OPO output (squeezed probe). The Jones Matrix for a wave plate is [7]

$$M_{wp} = \begin{bmatrix} \cos(\phi/2) + i\sin(\phi/2)\cos(2\theta) & i\sin(\phi/2)\sin(2\theta) \\ i\sin(\phi/2)\sin(2\theta) & \cos(\phi/2) - i\sin(\phi/2)\cos(2\theta) \end{bmatrix}, \tag{37}$$

where θ is the angle between the fast axis of the wave plate and p polarization (the direction of LO), and ϕ is the retardance of the wave-plate ($\phi = \pi$ or $\phi = \pi/2$ for an ideal $\lambda/2$ or $\lambda/4$ wave-plate, respectively). We fix the $\lambda/4$ wave plate at $\theta = 45°$ and put the $\lambda/2$ wave plate at a variable angle θ_v, resulting in the output Jones vector

$$J_{out} = M_{\lambda/2}(\theta_v) M_{\lambda/4}(45°) J_{in} = \begin{bmatrix} J_1 \\ J_2 \end{bmatrix} \tag{38}$$

with

$$J_1 = \frac{1}{\sqrt{2}} \left[iE_{LO}e^{i(2\theta_v - \phi_{LO})} - E_{SP}e^{-i(2\theta_v + \phi_{SP})} \right]$$

$$J_2 = \frac{1}{\sqrt{2}} \left[E_{LO}e^{i(2\theta_v - \phi_{LO})} - iE_{SP}e^{-i(2\theta_v + \phi_{SP})} \right]. \tag{39}$$

Therefore, the interference between the two polarization modes observed at the two diodes of the HD after the second PBS is:

$$I_{HD} = |J_1|^2 - |J_2|^2 = 2E_{SP}E_{LO}\sin(4\theta_v - \phi_d), \tag{40}$$

where $\phi_d = \phi_{SP} - \phi_{LO}$ is the initial phase difference between OPO output and LO mode before being overlapped at the first PBS. The result show that if we rotate the $\lambda/2$ wave plate by an angle of $1°$, the phase between LO and OPO output will change $4°$. The form of Eq. (40) also shows the visibility of the HD is not affected by the polarization transformation since it doesn't have any constant term. However, if the wave plates or PBS are not perfect, which means that the wave plates have either more or less retardance or that the PBS has a finite extinction ratio between s and p polarization, a similar calculation shows the rotation of $\lambda/2$ wave plate by $1°$ will result in a phase shift slightly deviating from $4°$, and that the visibility of the interference at HD can be reduced. We experimentally measure these imperfections as shown in the following subsection.

B. Phase calibration

During the experiment we lock ϕ_d to be either $0°$ or $90°$ with HD_L, and use the rotation of the $\lambda/2$ wave plate before each HD to control the phase of each mode. In order to account for potential imperfections in our experiment, we first measured the visibility reduction from imperfect polarization components. We find a worst-case reduction of the HD visibility from 98.5% to 95.2%. We also perform a phase calibration by scanning the phase between LO and SP carrier with a ramp at 27 Hz while the interference fringe measured from V_{dc} of HD_L and $\text{HD}_{1,2,3,4}$ is recorded. The phase between LO and signal in each path is inferred from sine curve fitting. We calibrate the phase with 40 repeated measurements at each $\lambda/2$ wave plate position, and the result is shown in Fig. 8. The SQ (blue dots) shows the result when we lock $\phi_i = 0°$ and the HDs measure the squeezed quadrature, and the ASQ (red dots) shows the result when we lock $\phi_i = 90°$. For both SQ and ASQ, we rotate the $\lambda/2$ wave-plate position in each channel by an actuator in the wave-plate mount, allowing us to faithfully use the calibration result in the experiment.
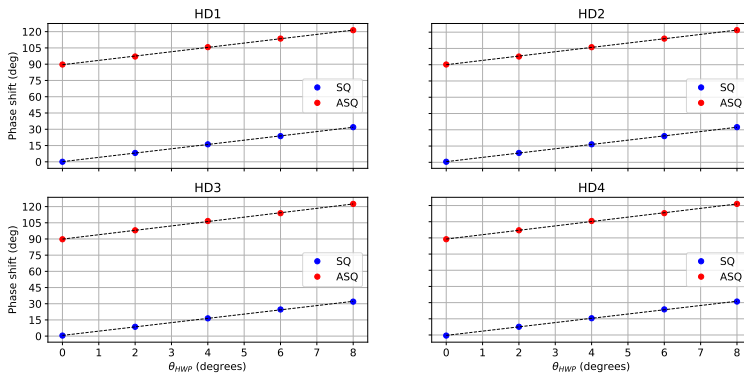
FIG. 8. Phase calibration result for each HD. The black dashed line is the linear fitting of the calibration.

TABLE I. The phase calibration result

Squeezing							
k1	-3.96	k2	-3.97	k3	-3.95	k4	-3.96
b1	-0.13	b2	-0.59	b3	-0.64	b4	0.37
Anti-squeezing							
k1	-3.99	k2	-3.99	k3	-4.06	k4	-4.06
b1	-89.50	b2	-89.97	b3	-89.87	b4	-88.90

From the calibration results, we see that the phase is linear within the whole range of the actuator ($8°$) on the wave plate mounts. The result of the linear fitting to HD channel $j = 1$ to 4 with the equation

$$\phi_j = k_j\theta_v + b_j \tag{41}$$

is summarized in Table I. With these fitted parameters, we can control both the phase in each channel ϕ_j or the averaged phase ϕ_{avg} accurately. Particularly, if we lock ϕ_i to $0°$, we can change the ϕ_{avg} by a slope of $3.96° \pm 0.02°$; if we lock ϕ_i to $90°$, can change the ϕ_{avg} by a slope of $4.02° \pm 0.02°$.

IV.   DATA ANALYSIS

In this section we introduce the details of our data analysis procedure, which includes measuring the sensitivity by fitting and counting how many photons in average is used in the SP.

As the estimator of ϕ_{avg}, $\hat{P}_{\mathrm{avg}}$ is experimentally estimated from the PSD of the averaged output of the four HDs in each mode. Fig. 9 shows the PSD results measured for different ϕ_{avg}. Each PSD is obtained from the FFT of an average of 2000 oscilloscope traces. The spectrum peak at 3 MHz S_{pk} gives the value of

$$S_{pk} = 2V_{sn}^2 \cdot \langle \hat{P}_{\mathrm{avg}}^2 \rangle = 2V_{sn}^2 \cdot (\langle \Delta \hat{P}_{\mathrm{avg}}^2 \rangle + \langle \hat{P}_{\mathrm{avg}} \rangle^2), \tag{42}$$

where V_{sn} is the 4-mode shot noise limit (SNL) voltage from HDs decided by LO power, electronic gain and the digital filtering. The constant 2 in Eq. (42) comes from the commutation relationship we choose $[\hat{X}, \hat{P}] = i$. We start our data analysis by separating the peak into two voltage parts

$$S_{pk} = V_s^2 + V_n^2, \tag{43}$$

where $V_s = \sqrt{2}V_{sn}|\langle \hat{P}_{\mathrm{avg}} \rangle|$ is the signal part induced by the coherent photons of the side band, and $V_n = \sqrt{2}V_{sn}\sqrt{\langle \Delta \hat{P}_{\mathrm{avg}}^2 \rangle}$ is the part induced by the fluctuation of the light. Except at the 3 MHz peak, the spectra in Fig. 9 vary slowly with frequency. This enables us to extract V_n from the adjacent frequencies of the 3 MHz peak. The procedure of V_n estimation is illustrated with the anti-squeezing quadrature (ASQ, ϕ_{avg} = -89.5 ±0.8°) PSD in Fig. 9 as an example. We first do a linear fit with the frequency range indicated by the red dots, which is slightly away from 3 MHz. This fitting gives the black dashed line labeled as "Fitting for ASQ". V_n is then inferred by the square root value of the fitted line at 3 MHz. Since our side band line width is obviously smaller than the 5 kHz resolution of the FFT, only one peak point is observed in the PSDs in Fig. 9. Therefore, V_s can simply be calculated by the difference between the blue dot at 3 MHz and the fitting result.

In our experiment we always introduce equal positive phase shift in all channels. In this case we know that $\langle \hat{P}_{\mathrm{avg}} \rangle > 0$, and V_s and V_n relate to the averaged phase ϕ_{avg} by

$$V_s(\phi_{\mathrm{avg}}) = \sqrt{2}V_{sn}\langle \hat{P}_{\mathrm{avg}} \rangle = \frac{2}{\sqrt{M}}V_{sn} \cdot \alpha_e |\sin(\phi_{\mathrm{avg}} + \theta_1)|$$

$$V_n(\phi_{\mathrm{avg}}) = \sqrt{2}V_{sn}\sqrt{\Delta \hat{P}_{\mathrm{avg}}^2} = V_{sn} \cdot \sqrt{v_{sq}^2 \cos^2(\phi_{\mathrm{avg}} + \theta_2) + v_{asq}^2 \sin^2(\phi_{\mathrm{avg}} + \theta_2)}. \tag{44}$$

Here α is the real coherent amplitude from modulation, M is the mode number, θ_1 and θ_2 are parameters indicating the imperfections of the experimental setup (ideally they should be 0), where θ_1 parametrizes the residual amplitude modulation of the phase modulating EOM and θ_2 parametrizes the phase locking offset of the squeezing measurement. $v_{sq}^2 = \eta e^{-2r_e} + (1 - \eta)$ and $v_{asq}^2 = \eta e^{2r_e} + (1 - \eta)$ are squeezing and anti-squeezing degrees in SNL units. Note that the form of Eq. (44) rely on two assumptions: First, we assume that the modulation signal on the EOM is perfectly coherent so $V_s(\phi_{\mathrm{avg}})$ doesn't have an offset term. This assumption is consolidated by the fact that we drive the EOM with a sine wave generated from a function generator with phase noise less than -65 dBc. Second, we ignore the phase fluctuations of the phase locking. This assumption is consolidated by the high (~32 dB) signal-to-noise ratio of the locking detector HD_L, though this signal-to-noise ratio is not a direct measurement of the phase fluctuation.

A.   Sensitivity fitting

With V_s and V_n extracted for a range of ϕ_{avg} settings, we can estimate the sensitivity. By comparing the definition of σ in Eq. (4) with Eq. (44), the sensitivity to a small phase shift at a given ϕ_{avg} offset is

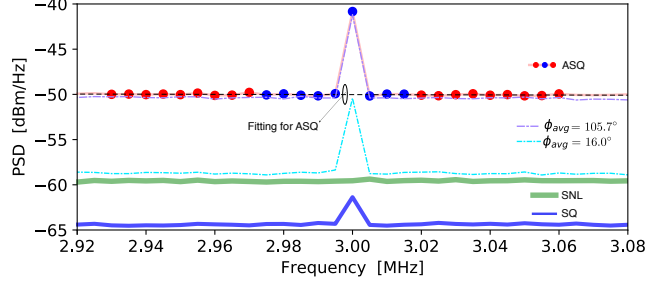$$\sigma = V_n(\phi_{\mathrm{avg}})/V_s'(\phi_{\mathrm{avg}}), \tag{45}$$

FIG. 9. PSDs of averaged HD output voltage with 3 MHz phase modulation on at different ϕ_{avg}. SNL: shot-noise limit; SQ, $\phi_{\text{avg}}=0.2 \pm 0.8°$; ASQ, $\phi_{\text{avg}} = 89.5 \pm 0.8°$. We estimate V_s and V_n from these PSDs.
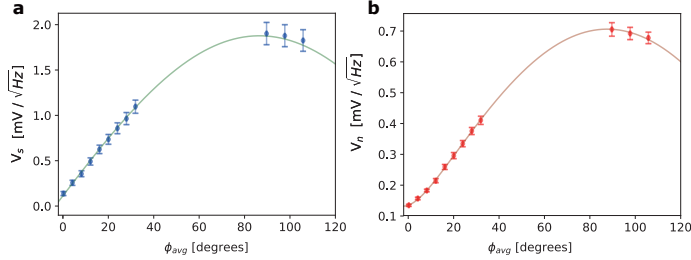

FIG. 10. **(a)** and **(b)**: Fitting from measured V_s and V_n in different ϕ_{avg}. With the fiting result, σ is estimated by using Eq. (46). All the error bars are standard deviation of the data.

where $V_s' = \partial V_s / \partial \phi_{\text{avg}}$ is the partial derivative of V_s with respect to ϕ_{avg} and the σ estimation is independent of SNL measurement since dividing V_n with V_s' can cancel V_{sn} out.

In the experiment we give an identical local phase shift to all 4 modes so that $\phi_j = \phi_{\text{avg}}$ for all $j = 1$ to 4, and change the value of ϕ_{avg} around both the squeezing $\phi_{\text{avg}} = 0$ and the anti-squeezing $|\phi_{\text{avg}}| = 90°$. The ϕ_{avg} we choose to induce as well as the fitting to Eq. (44) with measured V_s and V_n from Figure 9 is shown in Figure 10. In the $V_s(\phi_{\text{avg}})$ fitting, the parameters to fit are the slope $k = \sqrt{\frac{2}{M}} V_{sn} \alpha_e$ and θ_1. In the V_n fitting, the squeezing noise voltage scaled by SNL, $k_{sq} = V_{sn} \cdot v_{sq}$, the anti-squeezing noise voltage scaled by SNL, $k_{asq} = V_{sn} \cdot v_{asq}$, and θ_2 are fitting parameters. With the fitting result, we estimate the small angle sensitivity of our system σ_{min} by

$$\sigma_{min} = \frac{V_n(\phi_{\text{avg}} = 0)}{V_s'(\phi_{\text{avg}} = 0)}. \qquad (46)$$

We do fitting for 5 different pump power of OPO and find the fitted values of θ_1 and θ_2 are $3.4° \pm 0.2°$ and $1.6° \pm 0.6°$, respectively. These values are reasonably small, and in principle could be further reduced by better locking and phase modulation techniques. For the most sensitive case (maximum squeezing rate) in our result, the fitted θ_1 and θ_2 indicate σ_{min} could have been further improved by $\sim 0.2\%$ and $\sim 0.9\%$, respectively. The σ_{min} extracted in Eq. (46) is shown in our experiment results for the entangled approach in main text Fig 3 as σ_e. The uncertainty of V_s' is obtained from the fitting, and the uncertainty of V_n is obtained from the standard deviation of 2000 measurements. The error bars for σ in Fig. 3 are calculated by error propagation of Eq. (46).

A similar analysis method is used for the separable approach, but the PSDs used in the separable approach are from only one HD instead of averaged HD outputs. By removing the BSN, our setup gives the separable approach of $M = 1$. To compare with the entangled approach of $M = 4$, we rescale our result with $1/\sqrt{M}$ as a result of classical averaging. The scaled sensitivity is quoted as our experiment result for the separable approach in main text Fig. 3 as σ_s.

B. Resource counting

In this section, we show how to experimentally measure the average photon number per mode that we use in the phase sensing.

For the entangled approach, we estimate $MN_e = MN_{e,coh} + MN_{e,sqz}$ by comparing the joint measurement PSDs for squeezing and anti-squeezing quadrature to that for SNL, where $M = 4$ is the mode number. With the notation defined above, the average number of squeezed photons for all modes in the entangled approach are obtained by comparing V_n to V_{sn} with

$$M \cdot N_{e,sqz} = \frac{1}{2} \left(\langle \Delta \hat{P}^2_{avg} \rangle + \langle \Delta \hat{X}^2_{avg} \rangle - 1 \right) = \frac{1}{4} \left[\frac{V_n^2(\phi_{\text{avg}} = 0°)}{V_{sn}^2} + \frac{V_n^2(\phi_{\text{avg}} = 90°)}{V_{sn}^2} - 2 \right], \tag{47}$$

Similarly, the average number of coherent photons are obtained by comparing V_s to V_{sn} with

$$M \cdot N_{e,coh} = \eta \alpha_e^2 = \frac{V_s^2(\phi_{\text{avg}} = 90°)}{4V_{sn}^2}. \tag{48}$$

With Eq. (47) and (48), $N_e = N_{e,coh} + N_{e,sqz}$ gives the N values in main text Fig. 3 for the entangled approach σ_e. The error bars for N in Fig. 3, entangled approach are calculated by error propagation of Eqs. (47-48).

For the separable approach, we use a very similar technique. However, the PSD is from a single HD instead of joint measurement. Explicitly, the photon number per mode for the separable approach is $N_s = N_{s,coh} + N_{s,sqz}$, with

$$N_{s,sqz} = \frac{1}{2} \left(\langle \Delta \hat{p}_j^2 \rangle + \langle \Delta \hat{x}_j^2 \rangle - 1 \right) = \frac{1}{4} \left[\frac{V_n^2(\phi = 0°)}{V_{sn'}^2} + \frac{V_n^2(\phi = 90°)}{V_{sn'}^2} - 2 \right] \tag{49}$$

and

$$N_{s,coh} = \frac{V_s^2(\phi = 90°)}{4V_{sn'}^2}, \tag{50}$$

where ϕ is the phase shift of the single mode, and we use $V_{sn'}$ to denote the 1-mode SNL, which is about $1/4$ of the 4-mode SNL V_{sn} used in the entangled approach. The photon number per mode $N_s = N_{s,coh} + N_{s,sqz}$ gives the N values in main text Fig. 3 for the separable approach σ_s. The error bars for N in Fig. 3, separable approach are calculated by error propagation of Eqs. (60-61).

[1] Proctor, T. J., Knott, P. A. & Dunningham, J. A. Multiparameter estimation in networked quantum sensors. *Phys. Rev. Lett.* **120**, 080501 (2018).

[2] Berni, A. A. *et al.* Ab initio quantum-enhanced optical phase estimation using real-time feedback control. *Nature Photonics* **9**, 577–581 (2015).

[3] Neuhaus, L. *et al.* Pyrpl (python red pitaya lockbox) - an open-source software package for fpga-controlled quantum optics experiments. In *2017 Conference on Lasers and Electro-Optics Europe & European Quantum Electronics Conference (CLEO/Europe-EQEC)* (Optical Society of America, 2017).

[4] Grangier, P., Slusher, R. E., Yurke, B. & LaPorta, A. Squeezed-light-enhanced polarization interferometer. *Phys. Rev. Lett.* **59**, 2153–2156 (1987).

[5] Polzik, E., Carri, J. & Kimble, H. Atomic spectroscopy with squeezed light for sensitivity beyond the vacuum-state limit. *Applied Physics B* **55**, 279–290 (1992).

[6] Vidal, G. & Werner, R. F. Computable measure of entanglement. *Phys. Rev. A* **65**, 032314 (2002).

[7] Collett, E. Field guide to polarization. *SPIE Press, Bellingham, WA* (2005).

Bibliography

[1] Flagship, Q. Q. The future is quantum (2020). URL https://qt.eu/.

[2] P., D. J. & J., M. G. Quantum technology: the second quantum revolution. *Phil. Trans. R. Soc. A.* **361**, 1655–1674 (2003).

[3] Arute, F. *et al.* Quantum supremacy using a programmable superconducting processor. *Nature* **574**, 505–510 (2019). URL http://www.nature.com/articles/s41586-019-1666-5.

[4] Pednault, E., Gunnels, J., Maslov, D. & Gambetta, J. On "quantum supremacy" (2019). URL https://www.ibm.com/blogs/research/2019/10/on-quantum-supremacy/.

[5] Kumar, N., Kerenidis, I. & Diamanti, E. Experimental demonstration of quantum advantage for one-way communication complexity surpassing best-known classical protocol. *Nat Commun* **10** (2019).

[6] Arvidsson-Shukur, D. R. M. *et al.* Quantum advantage in postselected metrology. *Nat Commun* **11** (2020).

[7] Kimble, H. J. The quantum internet. *Nature* **453** (2008). 0806.4195.

[8] Wehner, S., Elkouss, D. & Hanson, R. Quantum internet: A vision for the road ahead. *Science* **362** (2018). URL https://science.sciencemag.org/content/362/6412/eaam9288. https://science.sciencemag.org/content/362/6412/eaam9288.full.pdf.

[9] Briegel, H.-J., Dür, W., Cirac, J. I. & Zoller, P. Quantum repeaters: The role of imperfect local operations in quantum communication. *Phys. Rev. Lett.* **81**, 5932–5935 (1998). URL https://link.aps.org/doi/10.1103/PhysRevLett.81.5932.

[10] Muralidharan, S. *et al.* Optimal architectures for long distance quantum communication. *Sci. Rep* **6** (2016).

[11] Borregaard, J. *et al.* One-way quantum repeater based on near-deterministic photon-emitter interfaces. *Phys. Rev. X* **10**, 021071 (2020). URL https://link.aps.org/doi/10.1103/PhysRevX.10.021071.

[12] Proctor, T. J., Knott, P. A. & Dunningham, J. A. Multiparameter estimation in networked quantum sensors. *Phys. Rev. Lett.* **120**, 080501 (2018). URL https://link.aps.org/doi/10.1103/PhysRevLett.120.080501.

[13] Ge, W., Jacobs, K., Eldredge, Z., Gorshkov, A. V. & Foss-Feig, M. Distributed quantum metrology with linear networks and separable inputs. *Phys. Rev. Lett.* **121**, 043604 (2018). URL https://link.aps.org/doi/10.1103/PhysRevLett.121.043604.

[14] Zhuang, Q., Zhang, Z. & Shapiro, J. H. Distributed quantum sensing using continuous-variable multipartite entanglement. *Phys. Rev. A* **97**, 032329 (2018). URL https://link.aps.org/doi/10.1103/PhysRevA.97.032329.

[15] Gerry, C. & Knight, P. *Introductory Quantum Optics* (Cambridge University Press, 2004).

[16] Agarwal, G. S. *Quantum Optics* (Cambridge University Press, 2012).

[17] Wigner, E. On the quantum correction for thermodynamic equilibrium. *Phys. Rev.* **40**, 749–759 (1932). URL https://link.aps.org/doi/10.1103/PhysRev.40.749.

[18] Jozsa, R. Fidelity for mixed quantum states. *Journal of Modern Optics* **41**, 2315–2323 (1994).

[19] Uhlmann, A. The "transition probability" in the state space of a *-algebra. *Reports on Mathematics* **9**, 273–279 (1976).

[20] Nielsen, M. A. & Chuang, I. L. *Quantum Computation and Quantum Information (2nd ed.)* (Cambridge University Press, England, 2010).

[21] Fuchs, C. A. & van de Graaf, J. Cryptographic distinguishability measures for quantum mechanical states. *IEEE Transactions on Information Theory* **45** (1999).

[22] Leonhardt, U. *Measuring the Quantum State of Light* (Cambridge University Press, England, 1997).

[23] Andersen, U. L., Gehring, T., Marquardt, C. & Leuchs, G. 30 years of squeezed light generation. *Physica Scripta* **91**, 053001 (2016). URL `http://arxiv.org/abs/1511.03250v1http://stacks.iop.org/1402-4896/91/i=5/a=053001?key=crossref.55d40e34c2e428c19fc293296c741aa3.1511.03250`.

[24] Neergaard-Nielsen, J. S. *Generation of single photons and Schrödinger kitten states of light*. Ph.D. thesis, University of Copenhagen, Denmark (2008).

[25] Collett, M. J. & Gardiner, C. W. Squeezing of intracavity and traveling-wave light fields produced in parametric amplification. *Phys. Rev. A* **30**, 1386–1391 (1984). URL `https://link.aps.org/doi/10.1103/PhysRevA.30.1386`.

[26] Dakna, M., Anhut, T., Opatrný, T., Knöll, L. & Welsch, D.-G. Generating schrödinger-cat-like states by means of conditional measurements on a beam splitter. *Phys. Rev. A* **55**, 3184–3194 (1997). URL `https://link.aps.org/doi/10.1103/PhysRevA.55.3184`.

[27] Wenger, J., Tualle-Brouri, R. & Grangier, P. Non-gaussian statistics from individual pulses of squeezed light. *Phys. Rev. Lett.* **92**, 153601 (2004). URL `https://link.aps.org/doi/10.1103/PhysRevLett.92.153601`.

[28] Ourjoumtsev, A., Tualle-Brouri, R., Laurat, J. & Grangier, P. Generating optical schrödinger kittens for quantum information processing. *Science* **312**, 83–86 (2006). URL `https://science.sciencemag.org/content/312/5770/83`.

[29] Neergaard-Nielsen, J. S., Nielsen, B. M., Hettich, C., Mølmer, K. & Polzik, E. S. Generation of a superposition of odd photon number states for quantum information networks. *Phys. Rev. Lett.* **97**, 083604 (2006). URL `https://link.aps.org/doi/10.1103/PhysRevLett.97.083604`.

[30] Wakui, K., Takahashi, H., Furusawa, A. & Sasaki, M. Photon subtracted squeezed states generated with periodically poled ktiopo4. *Opt. Express* **15**, 3568–3574 (2007). URL `http://www.opticsexpress.org/abstract.cfm?URI=oe-15-6-3568`.

[31] Takahashi, H. *et al.* Generation of large-amplitude coherent-state superposition via ancilla-assisted photon subtraction. *Phys. Rev. Lett.* **101**, 233605 (2008). URL `https://link.aps.org/doi/10.1103/PhysRevLett.101.233605`.

[32] Gerrits, T. *et al.* Generation of optical coherent-state superpositions by number-resolved photon subtraction from the squeezed vacuum. *Phys. Rev. A* **82**, 031802 (2010). URL `https://link.aps.org/doi/10.1103/PhysRevA.82.031802`.

[33] Lund, A. P., Jeong, H., Ralph, T. C. & Kim, M. S. Conditional production of superpositions of coherent states with inefficient photon detection. *Phys. Rev. A* **70**, 020101 (2004). URL https://link.aps.org/doi/10.1103/PhysRevA.70.020101.

[34] Oh, C. & Jeong, H. Efficient amplification of superpositions of coherent states using input states with different parities. *J. Opt. Soc. Am. B* **35**, 2933–2939 (2018). URL http://josab.osa.org/abstract.cfm?URI=josab-35-11-2933.

[35] Huang, K. *et al.* Optical synthesis of large-amplitude squeezed coherent-state superpositions with minimal resources. *Phys. Rev. Lett.* **115**, 023602 (2015). URL https://link.aps.org/doi/10.1103/PhysRevLett.115.023602.

[36] Etesse, M., Jean bestpapersand Bouillard, Kanseri, B. & Tualle-Brouri, R. Experimental generation of squeezed cat states with an operation allowing iterative growth. *Phys. Rev. Lett.* **114**, 193602 (2015). URL https://link.aps.org/doi/10.1103/PhysRevLett.114.193602.

[37] Sychev, D. V., Ulanov, A. E., Richards, M. W., Fedorov, I. A. & Lvovsky, A. I. Enlargement of optical schrödinger's cat states. *Nature Photonics* **11**, 379–382 (2017). URL https://doi.org/10.1038/nphoton.2017.57.

[38] Harder, G. *et al.* Local sampling of the wigner function at telecom wavelength with loss-tolerant detection of photon statistics. *Phys. Rev. Lett.* **116**, 133601 (2016). URL https://link.aps.org/doi/10.1103/PhysRevLett.116.133601.

[39] Baune, C., Fiurášek, J. & Schnabel, R. Negative wigner function at telecommunication wavelength from homodyne detection. *Phys. Rev. A* **95**, 061802 (2017). URL https://link.aps.org/doi/10.1103/PhysRevA.95.061802.

[40] Asavanant, W., Nakashima, K., Shiozawa, Y., Yoshikawa, J.-I. & Furusawa, A. Generation of highly pure schrödinger’s cat states and real-time quadrature measurements via optical filtering. *Opt. Express* **25**, 32227–32242 (2017). URL http://www.opticsexpress.org/abstract.cfm?URI=oe-25-26-32227.

[41] Takase, K., ichi Yoshikawa, J., Asavanant, W., Endo, M. & Furusawa, A. Generation of optical schrödinger's cat states by generalized photon subtraction (2020). 2009.08580.

[42] Mølmer, K. Non-gaussian states from continuous-wave gaussian light sources. *Phys. Rev. A* **73**, 063804 (2006). URL https://link.aps.org/doi/10.1103/PhysRevA.73.063804.

[43] Neergaard-Nielsen, J. S., Nielsen, B. M., Hettich, C., Mølmer, K. & Polzik, E. S. Generation of a superposition of odd photon number states for quantum information networks. *Phys. Rev. Lett.* **97**, 083604 (2006). URL https://link.aps.org/doi/10.1103/PhysRevLett.97.083604.

[44] Lund, A. P. & Ralph, T. C. Coherent-state linear optical quantum computing gates using simplified diagonal superposition resource states. *Phys. Rev. A* **71**, 032305 (2005). URL https://link.aps.org/doi/10.1103/PhysRevA.71.032305.

[45] Nielsen, A. E. B. & Mølmer, K. Single-photon-state generation from a continuous-wave nondegenerate optical parametric oscillator. *Phys. Rev. A* **75**, 023806 (2007). URL https://link.aps.org/doi/10.1103/PhysRevA.75.023806.

[46] Vogel, K. & Risken, H. Determination of quasiprobability distributions in terms of probability distributions for the rotated quadrature phase. *Phys. Rev. A* **40**, 2847–2849 (1989).

[47] Smithey, D. T., Beck, M., Raymer, M. G. & Faridani, A. Measurement of the wigner distribution and the density matrix of a light mode using optical homodyne tomography: Application to squeezed states and the vacuum. *Phys. Rev. Lett.* **70**, 1244–1247 (1993).

[48] Larsen, M. V., Guo, X., Breum, C. R., Neergaard-Nielsen, J. S. & Andersen, U. L. Fiber-coupled EPR-state generation using a single temporally multiplexed squeezed light source. *npj Quantum Information* **5**, 46 (2019). URL http://www.nature.com/articles/s41534-019-0170-y.

[49] Lvovsky, A. I. Iterative maximum-likelihood reconstruction in quantum homodyne tomography. *Journal of Optics B: Quantum and Semiclassical Optics* **6**, S556–S559 (2004). URL https://doi.org/10.1088%2F1464-4266%2F6%2F6%2F014.

[50] Cimini, V., Barbieri, M., Treps, N., Walschaers, M. & Parigi, V. Neural networks for detecting multimode wigner negativity. *Phys. Rev. Lett.* **125**, 160504 (2020). URL https://link.aps.org/doi/10.1103/PhysRevLett.125.160504.

[51] Nehra, R. *et al.* State-independent quantum state tomography by photon-number-resolving measurements. *Optica* **6**, 1356–1360 (2019).

[52] Banaszek, K., D'Ariano, G. M., Paris, M. G. A. & Sacchi, M. F. Maximum-likelihood estimation of the density matrix. *Phys. Rev. A* **61**, 010304 (1999). URL https://link.aps.org/doi/10.1103/PhysRevA.61.010304.

[53] Lvovsky, A. I. *et al.* Production and applications of non-gaussian quantum states of light (2020). 2006.16985.

[54] Saleh, B. E. & Teich, M. C. *Fundamentals of Photonics (2nd ed.)* (John Wiley and Sons, Inc., New Jersey, USA, 2007).

[55] Black, E. D. An introduction to pound–drever–hall laser frequency stabilization. *American Journal of Physics* **69**, 79–87 (2001).

[56] Breum, C. R. *Long distance distribution of optical cat states*. Ph.D. thesis, Technical University of Denmark, Denmark (2017).

[57] Boyd, G. D. & Kleinman, D. A. Parametric interaction of focused gaussian light beams. *Journal of Applied Physics* **39**, 3597–3639 (1968).

[58] Masada, G. Evaluation of second order nonlinearity in periodically poled *ktiopo$_4$* and *ktioaso$_4$* crystals using boyd and kleinman theory. *Tamagawa University Quantum ICT Reasearch Institute Bulletin* **3**, 21–24 (2013).

[59] Eberle, T. *et al.* Quantum enhancement of the zero-area sagnac interferometer topology for gravitational wave detection. *Phys. Rev. Lett.* **104**, 251102 (2010). URL https://link.aps.org/doi/10.1103/PhysRevLett.104.251102.

[60] Mehmet, M. *et al.* Squeezed light at 1550 nm with a quantum noise reduction of 12.3 db. *Opt. Express* **19**, 25763–25772 (2011). URL http://www.opticsexpress.org/abstract.cfm?URI=oe-19-25-25763.

[61] Eberle, T., Händchen, V. & Schnabel, R. Stable control of 10 db two-mode squeezed vacuum states of light. *Opt. Express* **21**, 11546–11553 (2013). URL http://www.opticsexpress.org/abstract.cfm?URI=oe-21-9-11546.

[62] Emanueli, S. & Arie, A. Temperature-dependent dispersion equations for ktiopo4 and ktioaso4. *Appl. Opt.* **42**, 6661–6665 (2003). URL http://ao.osa.org/abstract.cfm?URI=ao-42-33-6661.

[63] Fradkin, K., Arie, A., Skliar, A. & Rosenman, G. Tunable midinfrared source by difference frequency generation in bulk periodically poled ktiopo4. *Applied Physics Letters* **74**, 914–916 (1999).

[64] Kato, K. & Takaoka, E. Sellmeier and thermo-optic dispersion formulas for ktp. *Appl. Opt.* **41**, 5040–5044 (2002). URL http://ao.osa.org/abstract.cfm?URI=ao-41-24-5040.

[65] Fan, T. Y. *et al.* Second harmonic generation and accurate index of refraction measurements in flux-grown ktiopo4. *Appl. Opt.* **26**, 2390–2394 (1987). URL http://ao.osa.org/abstract.cfm?URI=ao-26-12-2390.

[66] Bachor, H.-A. & Ralph, T. *A Guide to Experiments in Quantum Optics, 2nd, Revised and Enlarged Edition* (WILEY-VCH Verlag GmbH & Co. KGaA, 2004).

[67] Polzik, E. S., Carri, J. & Kimble, H. J. Atomic spectroscopy with squeezed light for sensitivity beyond the vacuum-state limit. *Applied Physics B* **55**, 279–290 (1992).

[68] Larsen, M. V., Guo, X., Breum, C. R., Neergaard-Nielsen, J. S. & Andersen, U. L. Deterministic generation of a two-dimensional cluster state. *Science* **366**, 369–372 (2019). URL `http://www.sciencemag.org/lookup/doi/10.1126/science.aay4354`.

[69] Larsen, M. V., Guo, X., Breum, C. R., Neergaard-Nielsen, J. S. & Andersen, U. L. Deterministic multi-mode gates on a scalable photonic quantum computing platform (2020). URL `http://arxiv.org/abs/2010.14422`. 2010.14422.

[70] Wang, Z., Miki, S. & Fujiwara, M. Superconducting nanowire single-photon detectors for quantum information and communications. *IEEE Journal of Selected Topics in Quantum Electronics* **15**, 1741–1747 (2009).

[71] Miki, S., Yamashita, T., Terai, H. & Wang, Z. High performance fiber-coupled nbtin superconducting nanowire single photon detectors with gifford-mcmahon cryocooler. *Opt. Express* **21**, 10208–10214 (2013). URL `http://www.opticsexpress.org/abstract.cfm?URI=oe-21-8-10208`.

[72] Yamashita, T., Miki, S., Terai, H. & Wang, Z. Low-filling-factor superconducting single photon detector with high system detection efficiency. *Opt. Express* **21**, 27177–27184 (2013). URL `http://www.opticsexpress.org/abstract.cfm?URI=oe-21-22-27177`.

[73] Gifford, W. E. & Longsworth, R. C. Surface heat pumping. In Timmerhaus, K. D. (ed.) *Advances in Cryogenic Engineering*, 171–179 (Springer US, Boston, MA, 1966).

[74] Bechhoefer, J. Feedback for physicists: A tutorial essay on control. *Rev. Mod. Phys.* **77**, 783–836 (2005). URL `https://link.aps.org/doi/10.1103/RevModPhys.77.783`.

[75] Neuhaus, L. *et al.* Pyrpl (python red pitaya lockbox) — an open-source software package for fpga-controlled quantum optics experiments. In *2017 Conference on Lasers and Electro-Optics Europe European Quantum Electronics Conference (CLEO/Europe-EQEC)*, 1–1 (2017).

[76] Briles, T. C., Yost, D. C., Cingöz, A., Ye, J. & Schibli, T. R. Simple piezoelectric-actuated mirror with 180 kHz servo bandwidth. *Optics Express* **18**, 9739 (2010). URL `https://www.osapublishing.org/oe/abstract.cfm?uri=oe-18-10-9739`. 1003.5962.

[77] Aoki, T., Takahashi, G. & Furusawa, A. Squeezing at 946nm with periodically poled ktiopo4. *Opt. Express* **14**, 6930–6935 (2006). URL `http://www.opticsexpress.org/abstract.cfm?URI=oe-14-15-6930`.

[78] Morin, O., Fabre, C. & Laurat, J. Experimentally accessing the optimal temporal mode of traveling quantum light states. *Phys. Rev. Lett.* **111**, 213602 (2013). URL `https://link.aps.org/doi/10.1103/PhysRevLett.111.213602`.

[79] Yoshikawa, J.-i., Makino, K., Kurata, S., van Loock, P. & Furusawa, A. Creation, storage, and on-demand release of optical quantum states with a negative wigner function. *Phys. Rev. X* **3**, 041028 (2013). URL `https://link.aps.org/doi/10.1103/PhysRevX.3.041028`.

[80] MacRae, A., Brannan, T., Achal, R. & Lvovsky, A. I. Tomography of a high-purity narrowband photon from a transient atomic collective excitation. *Phys. Rev. Lett.* **109**, 033601 (2012). URL `https://link.aps.org/doi/10.1103/PhysRevLett.109.033601`.

[81] Takase, K. *et al.* Complete temporal mode characterization of non-Gaussian states by a dual homodyne measurement. *Physical Review A* **99**, 033832 (2019). URL `https://journals-aps-org.proxy.findit.dtu.dk/pra/pdf/10.1103/PhysRevA.99.033832https://link.aps.org/doi/10.1103/PhysRevA.99.033832`.

[82] Abdi, H. & Williams, L. J. Principal component analysis. *WIREs Computational Statistics* **2**, 433–459 (2010). URL `https://onlinelibrary.wiley.com/doi/abs/10.1002/wics.101`. `https://onlinelibrary.wiley.com/doi/pdf/10.1002/wics.101`.

[83] Larsen, M. V. *Quantum Information Protocols with Gaussian States of Light.* Ph.D. thesis, Technical University of Denmark, Denmark (2016).

[84] .

[85] Zhuang, Q., Preskill, J. & Jiang, L. Distributed quantum sensing enhanced by continuous-variable error correction. *New Journal of Physics* **22**, 022001 (2020). URL `https://doi.org/10.1088%2F1367-2630%2Fab7257`.

[86] Xia, Y. *et al.* Demonstration of a Reconfigurable Entangled Radio-Frequency Photonic Sensor Network. *Physical Review Letters* **124**, 150502 (2020). URL `http://arxiv.org/abs/1910.08825https://link.aps.org/doi/10.1103/PhysRevLett.124.150502`. 1910.08825.

[87] Lawrie, B. J., Lett, P. D., Marino, A. M. & Pooser, R. C. Quantum sensing with squeezed light. *ACS Photonics* **6**, 1307–1318 (2019).

[88] Qi, B., Lougovski, P., Pooser, R., Grice, W. & Bobrek, M. Generating the local oscillator "locally" in continuous-variable quantum key distribution based on coherent detection. *Phys. Rev. X* **5**, 041009 (2015). URL `https://link.aps.org/doi/10.1103/PhysRevX.5.041009`.

[89] Brask, J. B., Rigas, I., Polzik, E. S., Andersen, U. L. & Sørensen, A. S. Hybrid Long-Distance Entanglement Distribution Protocol. *Physical Review Letters* **105**, 160501 (2010). URL `https://link.aps.org/doi/10.1103/PhysRevLett.105.160501`. `1004.0083`.

[90] Neuhaus, L. Red pitaya dac performance (2016). URL `https://ln1985blog.wordpress.com/2016/02/07/red-pitaya-dac-performance/`.